

Spring 2024

Spectroscopy of Atmospheres

Randika Dodangodage
Old Dominion University, lakshmangold@live.com

Follow this and additional works at: https://digitalcommons.odu.edu/physics_etds



Part of the [Atmospheric Sciences Commons](#), [Chemistry Commons](#), and the [Physics Commons](#)

Recommended Citation

Dodangodage, Randika. "Spectroscopy of Atmospheres" (2024). Doctor of Philosophy (PhD), Dissertation, Physics, Old Dominion University, DOI: 10.25777/7f67-kf04
https://digitalcommons.odu.edu/physics_etds/208

This Dissertation is brought to you for free and open access by the Physics at ODU Digital Commons. It has been accepted for inclusion in Physics Theses & Dissertations by an authorized administrator of ODU Digital Commons. For more information, please contact digitalcommons@odu.edu.

SPECTROSCOPY OF ATMOSPHERES

by

Randika Dodangodage

B.S. July 2015, University of Sri Jayewardenepura, Sri Lanka

M.S. May 2020, Old Dominion University

A Dissertation Submitted to the Faculty of
Old Dominion University in Partial Fulfillment of the
Requirements for the Degree of

DOCTOR OF PHILOSOPHY

PHYSICS

OLD DOMINION UNIVERSITY

May 2024

Approved by:

Peter Bernath (Director)

Craig Bayse (Member)

Alex Gurevich (Member)

Amaryan Moskov (Member)

Colm Whelan (Member)

ABSTRACT

SPECTROSCOPY OF ATMOSPHERES

Randika Dodangodage
Old Dominion University, 2024
Director: Dr. Peter Bernath

Spectroscopic methods are used to study planetary and stellar atmospheres. The information obtained from spectroscopic studies provides insight into atmospheric compositions and dynamics, which can be used to model and characterize atmospheres and climates. Laboratory-recorded absorption cross-sections are needed to interpret the recorded spectra of planets and stars. High-resolution ethane, neopentane, propene, and *n*-butane spectra have been recorded, and absorption cross-sections have been provided for different temperatures and total pressures with different broadening gases, including hydrogen, helium, and nitrogen. The Atmospheric Chemistry Experiment (ACE) satellite orbits Earth and records spectra through solar occultation limb observations. HOCl is a chlorine reservoir molecule found in the Earth's stratosphere and is also responsible for polar ozone destruction. HOCl retrievals have been developed using the spectra recorded by the ACE. Analysis of ACE HOCl VMR data globally for the entire mission (2004-2020) shows a decreasing trend attributed to the Montreal Protocol's success. In ACE version 5.0 data, HFC-32 is a new molecule added. Global altitude-latitude VMR profiles for 2004 to 2020 were studied, and HFC-32 abundances are increasing exponentially. LaO and YO are characteristic features in the spectra of cool S-type stars. The $B^2\Sigma^+-X^2\Sigma^+$ and $A^2\Pi-X^2\Sigma^+$ transitions of LaO and the $B^2\Sigma^+-X^2\Sigma^+$ transition of YO were rotationally analyzed to provide spectroscopic constants and, more importantly, a line list suitable for simulating stellar spectra.

Copyright, 2024, by Randika Dodangodage, All Rights Reserved.

ACKNOWLEDGMENTS

I would like to express my sincere gratitude to several individuals who have contributed to the completion of my PhD thesis. First and foremost, I am deeply thankful to my advisor, Dr. Peter Bernath, for his unwavering support, guidance, and encouragement throughout this journey. His expertise, patience, and mentorship have been invaluable, and I am grateful for the opportunity to learn from him.

I also extend my special thanks to my colleagues and collaborators for their assistance and stimulating discussions, which have contributed significantly to my intellectual growth and development.

My family and friends deserve my heartfelt appreciation for their unwavering love, encouragement, and understanding throughout this endeavor. Their support has been my source of strength and motivation.

Finally, I thank all individuals who have contributed directly or indirectly to this thesis.

TABLE OF CONTENTS

	Page
LIST OF TABLES.....	vi
LIST OF FIGURES	viii
Chapter	
1. INTRODUCTION	1
1.1 MOLECULAR SPECTROSCOPY	1
1.2 REMOTE SENSING	2
1.3 EARTH'S ATMOSPHERE	3
1.4 SPECTROSCOPY OF PLANETARY ATMOSPHERES AND STARS	4
2. ABSORPTION CROSS SECTIONS OF HYDROCARBONS	6
2.1 INTERACTION OF RADIATION WITH MATTER	7
2.2 MEASUREMENT AND ANALYSIS OF HYDROCARBONS	10
3. MOLECULES IN EARTH'S ATMOSPHERE	31
3.1 ATMOSPHERIC CHEMISTRY EXPERIMENT (ACE).....	31
3.2 MONTREAL PROTOCOL AND STRATOSPHERIC OZONE DEPLETION	33
3.3 HOCl	33
3.4 HFC-32	40
4. SPECTROSCOPY OF DIATOMIC MOLECULES	46
4.1 SPECTROSCOPIC CONCEPTS	46
4.2 INTRODUCTION TO PGOPHER.....	51
4.3 LaO TRANSITIONS	52
4.4 YO TRANSITIONS	74
5. CONCLUSION AND FUTURE WORKS	84
REFERENCES	87
APPENDICES	
A. RKR AND LEVEL INPUT FILES FOR LaO TRANSITIONS	99
B. RKR AND LEVEL INPUT FILES FOR YO TRANSITIONS	207
VITA	218

LIST OF TABLES

Table	Page
1. Experimental conditions for each ethane spectrum.....	12
2. Experimental conditions for each neopentane spectrum	16
3. Experimental conditions for each propene spectrum in the CH stretching region.....	21
4. Experimental conditions for each propene spectrum in the 450-1250 cm ⁻¹ region.....	22
5. Comparison of propene integrated areas in the region 800-1100 cm ⁻¹	25
6. NOAA flask stations used.....	43
7. Spectroscopic parameters for X ² Σ ⁺ state of LaO.....	60
8. Spectroscopic parameters for B ² Σ ⁺ state of LaO.....	61
9. Sample of observed and calculated line list of the LaO B ² Σ ⁺ -X ² Σ ⁺ transition	62
10. Equilibrium constants of LaO for X ² Σ ⁺ and B ² Σ ⁺ states.....	63
11. Band strengths of B ² Σ ⁺ -X ² Σ ⁺ transition of LaO.....	64
12. Radiative lifetimes of LaO B ² Σ ⁺ state.....	65
13. Sample line list of the LaO B ² Σ ⁺ -X ² Σ ⁺ transition	66
14. Spectroscopic constants for the A ² Π state.....	69
15. Sample of observed and calculated line list of the LaO A ² Π-X ² Σ ⁺ transition.....	70
16. Equilibrium constants of LaO for the A ² Π state.....	71
17. Band strengths of A ² Π-X ² Σ ⁺ transition of LaO.....	72
18. Radiative lifetimes of LaO A ² Π state.....	72
19. Sample line list of the LaO A ² Π-X ² Σ ⁺ transition.....	73
20. Sample of observed and calculated line list of the B ² Σ ⁺ -X ² Σ ⁺ transition of YO	77
21. Spectroscopic constants of YO B ² Σ ⁺ and X ² Σ ⁺ states.....	78

Table	Page
22. Equilibrium constants for the $X^2\Sigma^+$ and $B^2\Sigma^+$ states of YO.....	80
23. Band strengths of $B^2\Sigma^+-X^2\Sigma^+$ transition.....	80
24. Radiative lifetimes of YO $B^2\Sigma^+$ state	81
25. Sample line list of the YO $B^2\Sigma^+-X^2\Sigma^+$ transition	82

LIST OF FIGURES

Figure	Page
1. Temperature profile of Earth's atmosphere at mid-latitudes.....	3
2. Absorption cross sections of ethane broadened by hydrogen at 291.75 K.....	13
3. Absorption cross sections of ethane broadened by hydrogen with different pressures at 292 K.....	14
4. Absorption cross sections of ethane broadened by hydrogen for 10 Torr of total pressure at different temperatures.....	15
5. Absorption cross section of neopentane broadened by nitrogen at 202.15 K.....	17
6. Overview of $\nu_{14}(t_2)$ band of pure neopentane at 202.15 K.....	18
7. $\nu_{13}(t_2)$ band of neopentane broadened by nitrogen at different temperatures for 100 Torr of total pressure.....	19
8. The effect of nitrogen broadening on rotational features of the neopentane $\nu_{14}(t_2)$ band at 202.15 K.....	20
9. Absorption cross sections of propene in the CH stretching region.....	23
10. Absorption cross sections of propene in the 450-1250 cm^{-1} stretching region.....	24
11. Absorption cross sections of propene broadened by helium at different total pressures at 295 K.....	26
12. Absorption cross sections of propene broadened by nitrogen at different total pressures at 202 K.....	27
13. Absorption cross sections of propene broadened by helium at different temperatures for 30 Torr of total pressure.....	28
14. Absorption cross sections of <i>n</i> -butane in the CH stretching region at two different temperatures.....	29
15. <i>n</i> -butane cross sections at 230.5 K showing the CH_2 symmetric stretch (ν_2) centered around 2886 cm^{-1}	30
16. Limb viewing geometry of ACE satellite.....	32
17. HOCl altitude-latitude VMR plot for the 2004-2020 mission average.....	35

Figure	Page
18. Seasonal distribution of HOCl VMR	36
19. Time series of HOCl for the region 60°S to 60°N, 30.5 km to 39.5 km.....	37
20. The mission average HOCl VMR distributions for sunrise and sunset.....	38
21. The mission average quarterly HOCl VMR distributions for sunrise and sunset.....	39
22. The average HFC-32 VMRs from Feb. 2004 to July 2020.....	41
23. The average HFC-32 VMRs for the regions 30-60°N and 30-60°S in the months of June, July and August 2019.....	42
24. HFC-32 VMR time series.....	44
25. The low-lying electronic states of LaO molecule.....	51
26. Overview emission spectrum of LaO showing $B^2\Sigma^+-X^2\Sigma^+$ and $A^2\Pi-X^2\Sigma^+$ transitions....	53
27. Ab initio transition dipole moment curves for the $B^2\Sigma^+-X^2\Sigma^+$ and $A^2\Pi-X^2\Sigma^+$ transi- tions of LaO.....	55
28. Hyperfine splitting of the LaO $B^2\Sigma^+$ and $X^2\Sigma^+$ states.....	57
29. The spectrum of LaO and simulation of the $B^2\Sigma^+-X^2\Sigma^+$ 1-0 band	67
30. The 0-0 band of the $A^2\Pi_{3/2}-X^2\Sigma^+$ transition of LaO.....	74
31. The simulated bands of $B^2\Sigma^+-X^2\Sigma^+$ transition of YO.....	79

CHAPTER 1

INTRODUCTION

1.1 MOLECULAR SPECTROSCOPY

The interaction between matter and electromagnetic radiation, wherein atoms and molecules absorb or emit photons, forms the basis of spectroscopy [1, 2]. These interactions lead to transitions between different energy states, and scientists study the details of these transitions to understand the behavior of atoms and molecules better.

Distinctive spectroscopic features inherent to atoms and molecules render them invaluable in many disciplines. In astronomy, spectroscopy is a powerful tool for identifying molecules and determining their abundances within planetary and stellar atmospheres. By analyzing stellar spectra, astronomers obtain insights into the composition and dynamics of stars, thereby enhancing our understanding of the universe's elemental origins. Planetary and stellar atmospheres exhibit characteristic atomic and molecular absorption and emission lines, providing vital clues about their composition and physical properties. Retrieving such information from observed spectra necessitates precise line parameters, including line positions and strengths, as well as absorption cross-sections and other spectroscopic parameters for all contributing species.

The accuracy of these parameters directly influences the reliability of derived molecular abundances, compositions, and the potential discovery of novel atmospheric constituents. Therefore, advancements in spectroscopic techniques and the refinement of spectroscopic data play pivotal roles in advancing our knowledge of the planetary and stellar atmospheres.

The electromagnetic spectrum is classified into several regions depending on frequency (ν), wavelength (λ), or wavenumber ($\bar{\nu}$). Frequency and wavelength are related by the equation $\lambda \nu = c$, where c is the speed of light. Wavenumber is defined as the reciprocal of the vacuum wavelength and generally given in the units of cm^{-1} . Conventionally the region $0.1\text{-}1 \text{ cm}^{-1}$ belongs to microwave region, $500\text{-}12500 \text{ cm}^{-1}$ range belongs to infrared region, and $12500\text{-}25000 \text{ cm}^{-1}$ is known as visible region. Plane waves can represent an electromagnetic wave

$$\mathbf{E}(\mathbf{r}, t) = \mathbf{E}_0 \cos(\mathbf{k} \cdot \mathbf{r} - \omega t). \quad (1)$$

\mathbf{E} is electric field, \mathbf{k} is the direction of propagation, $\omega = 2\pi\nu$ is the angular frequency and $|\mathbf{E}_0|$ is the amplitude of the electric field. Electromagnetic radiation carries a specific energy E

$$E = h\nu = \frac{hc}{\lambda}, \quad (2)$$

where h is the Planck constant ($h = 6.62607015 \times 10^{-34}$ Js). A system can change its energy by absorption or emission of photons. If the lower energy is E_0 and the upper energy is E_1 , the increase in energy can be written as

$$E_1 - E_0 = h\nu_{10}. \quad (3)$$

Where ν_{10} is the transition frequency between the upper and lower states. The state (or energy) of a system can be changed in three ways: absorption of a photon increases the energy from E_0 to E_1 , spontaneous emission decreases the energy from E_1 to E_0 by emitting a photon, and stimulated emission decreases energy from E_1 to E_0 by absorbing one photon and emitting two photons. The net energy change remains the same $h\nu_{10}$ in all three situations.

In the spectrum, ν_{10} appears as a line, and the intensity of the lines is a measure of how many photons were absorbed or emitted in that frequency. Pressure and temperature give width or shape to the line, referred to as line shape. The study of these line positions, intensities, and line shapes falls under the category of spectroscopy.

1.2 REMOTE SENSING

Scientists rely on various measurements to quantitatively analyze atmospheres' molecular characteristics and dynamics. These measurements include ground-based measurements taken from the Earth's surface, balloon-borne in situ measurements taken from a balloon in the atmosphere, airborne measurements taken from an aircraft, and satellite remote sensing methods used to gather information from space. Using these different methods, scientists can better understand the Earth's atmosphere and how it changes over time. In atmospheric science, in situ measurements are a commonly employed method for data collection. However, such measurements have a limited scope, as balloons and airplanes can only reach a certain altitude. Therefore, to study the Earth's atmosphere beyond this altitude, the use of satellites that view the Earth from orbit is essential. These spacecraft capture data from much higher up, providing crucial insights into the Earth's atmosphere that would otherwise be difficult to obtain. In essence, satellites play a pivotal role in expanding the scope of atmospheric research and are an indispensable tool in the field.

In this thesis, viewing the atmospheres of Earth, planets, and stars through spectroscopic methods is referred to as remote sensing. Different remote sensing techniques, including ground-based, airborne, and satellite-based measurements, are utilized to obtain spectra of these atmospheres. By interpreting these spectra, one can determine essential information such as temperature, pressure, precipitation, wind velocities, and concentrations of molecules like water vapor, CO₂, ozone, and more.

There are two main types of remote sensing systems: active and passive. Active systems emit

radiation and measure what is reflected back, while passive systems detect the radiation naturally emitted by objects in the environment, such as the sun's ultraviolet, visible, and near-infrared radiation. One example of a passive remote-sensing satellite is the Atmospheric Chemistry Experiment (ACE), orbiting Earth since 2004. The data gathered by ACE helps scientists better understand the composition, behavior, and evolution of Earth's atmosphere over time [3].

1.3 EARTH'S ATMOSPHERE

The Earth's atmosphere is a fascinating subject studied for many years. It is a complex and dynamic system divided into four distinct layers based on temperature [4]. Figure 1 shows the Earth's temperature variation with altitude. Each layer has unique characteristics essential to understanding how the atmosphere works and influences the planet's climate.

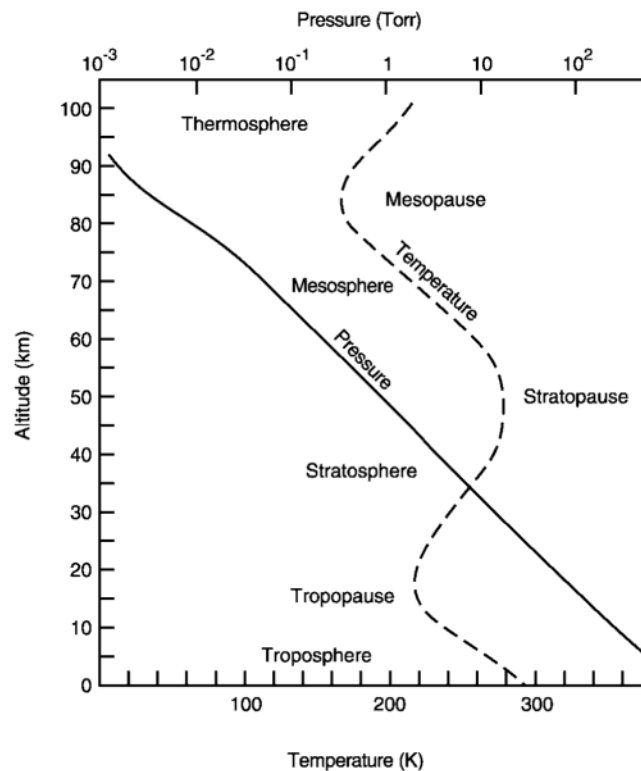


Figure 1. Temperature profile of Earth's atmosphere at mid-latitudes. Pressure variation is also shown. The figure is from Finlayson-Pitts and Pitts Jr [4].

The first layer is the troposphere, closest to the Earth's surface, extending up to about 10 km. Most weather phenomena occur here, and temperature decreases as altitude increases. The second layer, the stratosphere, extends from the top of the troposphere to about 50 km above the surface. Here, temperature increases as altitude increases due to ozone (O_3) gas. Ozone absorbs ultraviolet radiation ($\lambda < 290$ nm) from the sun, causing the temperature increase. The third layer, the mesosphere, extends from 50 to 85 km above the Earth's surface. Temperature decreases again with altitude. This layer is where meteors burn up when they enter the Earth's atmosphere. The final layer is the thermosphere, extending from 85 km. Here, temperature increases again due to the absorption of high-energy solar radiation by O_2 and N_2 . Understanding the characteristics of each layer of the Earth's atmosphere is crucial to comprehending the planet's climate system. It helps us track weather patterns, predict climate change, and develop strategies to mitigate the effects of atmospheric pollution.

The atmosphere is primarily composed of nitrogen (N_2) and oxygen (O_2) gases, which make up 78% and 21% of the atmosphere, respectively. However, a wide range of other gases are also present in trace amounts, including water vapor (H_2O), carbon dioxide (CO_2), methane (CH_4), and ozone (O_3), among others. These atmospheric gases play a critical role in the dynamics and chemistry of the atmosphere. For example, water vapor is essential in cloud formation and precipitation, while carbon dioxide and methane are potent greenhouse gases that trap heat in the atmosphere and contribute to global warming. Ozone, while beneficial in the upper atmosphere, where it shields us from harmful UV radiation, is a pollutant when present in the lower atmosphere.

Studying the Earth's atmosphere is vital to predicting weather patterns and modeling climate. Scientists use atmospheric data to understand how changes in the atmospheric composition will impact the Earth's temperature over time. For instance, the increase in greenhouse gases due to human activities has resulted in a warming trend that is projected to continue. Overall, the Earth's atmosphere is a complex system of gases that plays a vital role in regulating the planet's climate and supporting life. Understanding the chemistry and dynamics of the atmosphere is essential for developing effective strategies to mitigate the effects of climate change and ensure a sustainable planet.

1.4 SPECTROSCOPY OF PLANETARY ATMOSPHERES AND STARS

The universe is full of molecules that can be found in various environments. From diffuse clouds and dark clouds to planetary atmospheres and galaxies, molecules exist in numerous environments. Planets within our solar system are similar to Earth in terms of dynamic and chemical processes. For example, Venus, Earth, and Mars have rocky surfaces with thin and dense atmo-

spheres, while Jupiter, Saturn, Uranus, and Neptune have deep atmospheres composed mainly of hydrogen and helium [5]. Saturn's largest moon, Titan, has a thick atmosphere comprised mostly of nitrogen, where complex chemical reactions occur, forming molecules containing carbon, hydrogen, nitrogen, and oxygen. The molecules eventually settle on the surface, forming dunes, lakes, and seas. Among celestial bodies, it is the only planet besides Earth known to harbor lakes and seas on its surface, although composed of liquid methane and ethane rather than water [6]. Venus, the closest planet to Earth, has a similar size and mean density but is hotter due to the runaway greenhouse effect. Because Venus lacks a magnetic field, its atmosphere is constantly subjected to erosion by solar winds [5]. It has retained a large abundance of CO₂ (96.5%) and a minimal amount of nitrogen (3.5%) [7].

Studying stellar atmospheres and molecular clouds is crucial for understanding the universe's formation. Supernova explosions involve nuclear reactions that release a rapid burst of neutrons known as the *r*-process, which are absorbed by nuclei, forming elements heavier than Fe. Additionally, heavy elements are produced within stellar cores through nuclear reactions involving slow neutrons, known as the *s*-process, which are released during fusion reactions. Consequently, both supernova explosions and stellar winds enrich the interstellar medium with elements referred to as metals.

Spectroscopic techniques are used to identify molecular signatures in planetary and stellar atmospheres. Orbiting satellites and ground-based telescopes are used to obtain the spectra of the atmospheres discussed above. The recent launch of the James Webb Space Telescope (JWST) will use spectroscopy to identify new exoplanets and characterize the atmospheres of already identified exoplanets. Seager [8] has utilized spectroscopic techniques to identify molecular species in exoplanetary atmospheres, offering clues about their potential habitability. Recent studies have found hydrocarbons in planetary atmospheres like Jupiter [9–12], Saturn [13–15], Neptune [13, 16], Titan [10, 17] and also in molecular clouds like TMC-1 [18–20]. Electronic transitions of LaO, YO, ZrO, and ScO have been found in cool S-type stars [21].

Understanding the chemical compositions of different environments in the universe is essential for understanding the universe's formation and potential life on other planets. Spectroscopy and other scientific techniques help us identify and study different molecular signatures, leading to groundbreaking discoveries.

CHAPTER 2

ABSORPTION CROSS SECTIONS OF HYDROCARBONS

Absorption cross sections, a key parameter in spectroscopy, offer valuable insights into planets' composition and atmospheric conditions. The spectra of planets, obtained through ground-based, airborne, or satellite-based measurements, serve as cosmic fingerprints. These spectral fingerprints, however, are often blended by the absorption and emission features imprinted by the planetary or stellar atmosphere. Different molecules possess unique absorption cross-sections, causing them to absorb light at specific wavelengths. Laboratory-recorded spectra at or near atmospheric conditions are needed to identify these unique features from a complex spectrum.

Hydrocarbons are found in Earth's atmosphere as well as other planetary atmospheres. Methane features are observed in the spectra of outer planets and their moons [22]. Ethane is the second most abundant hydrocarbon, after methane, in many planetary atmospheres like Jupiter [23], Saturn [24], Neptune [25], and Uranus [26]. Saturn's moon Titan has an organic-rich atmosphere and is considered to be like the pre-biotic Earth [27, 28]. Several hydrocarbons like C_2H_2 , C_2H_4 , C_2H_6 , CH_3C_2H , C_3H_6 , C_3H_8 , and C_4H_2 were detected in the stratosphere of Titan [6] using infrared spectra taken from the Voyager spacecraft. Complex hydrocarbon reservoirs in both gaseous and condensed states are more likely present in cold planetary atmospheres [29]. Emissions from fossil fuel production are typically responsible for hydrocarbons in Earth's atmosphere [30], and hydrocarbons originate from the photolysis of methane in the atmospheres of Giant Planets [31] and Titan [6].

There is a growing interest in the atmospheric community to explore hydrocarbons in planetary atmospheres and molecular clouds. This chapter relies on published absorption cross-sections of ethane [32], neopentane [29], propene [33, 34], and *n*-butane [35]. Ethane, propene, and neopentane spectra were measured at the Canadian Light Source, while *n*-butane was measured at Old Dominion University. Jianbao Zhao and Brant Billinghamurst from the Canadian Light Source Far-Infrared Beamline recorded ethane, neopentane, and propene spectra. The original draft for neopentane [29] and propene [34] was written by Peter Bernath, while the original drafts for ethane [32] and propene [33] were composed by myself. R. Dodangodage conducted the formal analyses of the molecules. The work by Sorensen et al. [35] involves four hydrocarbons, and I contributed to the measurement, analysis, and writing related to *n*-butane.

2.1 INTERACTION OF RADIATION WITH MATTER

This section provides an overview of the fundamental principles that define the spectral properties of atoms or molecules. It explains crucial concepts such as Einstein coefficients, absorption cross-sections, and line shapes, which are used to determine these properties. The information presented is based on Bernath [1].

2.1.1 Einstein Coefficients

Imagine a cavity within a material where the temperature remains constant at T . The radiation emitted from the walls of the cavity is balanced with the radiation absorbed by the walls, resulting in equilibrium. The radiation density (ρ) inside the cavity over all frequencies can be defined as

$$\rho = \int_0^{\infty} \rho_{\nu} d\nu. \quad (4)$$

The frequency distribution of this radiation is represented by ρ_{ν} which is known as the Planck function,

$$\rho_{\nu}(T) = \frac{8\pi h\nu^3}{c^3} \frac{1}{e^{\frac{h\nu}{kT}} - 1}, \quad (5)$$

where T is temperature and $K = 1.380649 \times 10^{-23} \text{ JK}^{-1}$ is the Boltzmann constant.

Consider a non-degenerate two-level system with energies E_0 and E_1 at a constant temperature T . Considering the system is in thermal equilibrium the population N_0 (number of systems with energy E_0) and N_1 (number of systems with energy E_1) are related by the Boltzmann expression

$$\frac{N_1}{N_0} = e^{-\frac{h\nu_{10}}{kT}}. \quad (6)$$

The rate which drives a state from a lower energy level to a higher energy level as a result of absorption can be written as

$$\frac{dN_1}{dt} = B_{1\leftarrow 0} \rho_{\nu}(\nu_{10}) N_0, \quad (7)$$

where $B_{1\leftarrow 0}$ is the Einstein B coefficient. Similarly, in the case of stimulated emission, the rate is given by

$$\frac{dN_1}{dt} = -B_{1\rightarrow 0} \rho_{\nu}(\nu_{10}) N_1, \quad (8)$$

and the rate of spontaneous emission is given by

$$\frac{dN_1}{dt} = -A_{1\rightarrow 0} N_1. \quad (9)$$

The rate constant, $A_{1\rightarrow 0}$, is known as the Einstein A coefficient. Since the system is in thermal equilibrium, the absorption rate must be equal to the emission rate. Hence, we can write

$$B_{1\leftarrow 0} \rho_{\nu}(\nu_{10}) N_0 = A_{1\rightarrow 0} N_1 + B_{1\rightarrow 0} \rho_{\nu}(\nu_{10}) N_1 \quad (10)$$

$$\frac{N_1}{N_0} = \frac{B_{1\leftarrow 0}\rho_{\nu}(\nu_{10})}{A_{1\rightarrow 0} + B_{1\rightarrow 0}\rho_{\nu}(\nu_{10})} = e^{-\frac{h\nu_{10}}{kT}}. \quad (11)$$

Solving for $\rho_{\nu}(\nu_{10})$,

$$\rho_{\nu}(\nu_{10}) = \frac{A_{1\rightarrow 0}}{B_{1\leftarrow 0}e^{\frac{h\nu_{10}}{kT}} - B_{1\rightarrow 0}}. \quad (12)$$

$\rho_{\nu}(\nu_{10})$ is also given by Planck's function (Equation (5)). For both of these to be valid, it is necessary that,

$$B_{1\leftarrow 0} = B_{1\rightarrow 0}, \quad (13)$$

and

$$A_{1\rightarrow 0} = \frac{8\pi h\nu^3}{c^3} B_{1\leftarrow 0}. \quad (14)$$

The interaction of electromagnetic radiation with matter can also be represented using the time-independent Schrödinger equation

$$\hat{H}\Psi_n = E_n\Psi_n. \quad (15)$$

In this representation, the two-level system is described using two wave functions, ψ_0 being the lower state and ψ_1 being the upper state. A system (molecule) consists of a nucleus and a charge distribution, which results in a dipole moment μ

$$\vec{\mu} = \sum q_i \vec{r}_i. \quad (16)$$

This is taken into account by the addition of $\hat{H}'(t) = -\vec{\mu} \cdot \vec{E}$ as a perturbation to the Schrödinger equation. General solutions to the Schrödinger equation without perturbation are $\Psi_0(t) = \psi_0 e^{-i\omega_0 t}$, and $\Psi_1(t) = \psi_1 e^{-i\omega_1 t}$. The complete solution leads to the term $\mu_{10} = \langle \psi_1 | \mu | \psi_0 \rangle$ known as transition dipole moment.

The Einstein A and B coefficients can be written to include transition dipole moments as follows [1]:

$$B_{1\leftarrow 0} = \frac{1}{6\epsilon_0 \hbar^2} \mu_{10}^2, \quad (17)$$

$$A_{1\rightarrow 0} = \frac{16\pi^3 \nu^3}{3\epsilon_0 \hbar c^3} \mu_{10}^2. \quad (18)$$

2.1.2 Absorption Cross Section

Consider a two-level system with a molecular density (molecules/m³) N_0 in the ground state and N_1 in the upper state. When radiation with intensity I_0 is entered into the system, it will be absorbed or can induce stimulated emission, and the emitted radiation will have an intensity of I .

The effective area of a molecule presented to the incident radiation is interpreted as the absorption cross section (σ) with units of $\text{m}^2/\text{molecule}$. The change in intensity can be written as

$$dI = -\sigma I(N_0 - N_1)dx. \quad (19)$$

If the radiation goes through a path length of l , we can integrate along the absorption path,

$$\begin{aligned} \int_{I_0}^I \frac{dI}{I} &= -\sigma(N_0 - N_1) \int_0^l dx \\ \ln\left(\frac{I}{I_0}\right) &= -\sigma(N_0 - N_1)l \\ \frac{I}{I_0} &= e^{-\sigma(N_0 - N_1)l}. \end{aligned} \quad (20)$$

Equation (20) is known as the Beer-Lambert law. Absorption cross-section and concentration are combined to define an absorption coefficient $\alpha = \sigma(N_0 - N_1)$ or concentration and path length are combined to define column density $x = (N_0 - N_1)l$.

2.1.3 Line Shapes

The absorption features are seen as lines in a spectrum. These lines have definite widths and characteristic shapes and are described with a line shape function, typically a Lorentzian or a Gaussian function [1]. The population in the ground state will move to the upper state by absorbing energy, and with time, they will lose that energy and return to the ground state. This is called spontaneous emission, and the system is said to have an intrinsic lifetime τ_{sp} at that upper state energy E_1 . This spontaneous emission gives a Lorentzian function to the line shape, and full width at half maximum (FWHM) is given by [1],

$$\Delta\nu_{1/2} = \frac{1}{2\pi\tau_{sp}}. \quad (21)$$

This is known as natural lifetime broadening.

A simplified model within the semi-classical picture estimates the pressure-broadening effect. As the pressure (p) changes in the system, the number of collisions changes. For example, if the pressure increases, the time between collisions decreases. This also changes the effective absorption cross-section of the atom or molecule, which affects the line shape. The FWHM due to pressure broadening is given as [1],

$$\Delta\nu_{1/2} = bp, \quad (22)$$

where b is the pressure broadening coefficient.

Different velocities of absorbing particles create a Doppler shift in the spectrum, resulting in broader lines. The velocity distribution of the system is affected by particle mass (m) and temperature (T). The FWHM due to Doppler broadening (temperature broadening) is given by [1],

$$\Delta\nu_{1/2} = 2\nu_0 \sqrt{\frac{2kT \ln(2)}{mc^2}}, \quad (23)$$

where k is the Boltzmann constant and ν_0 is the resonance frequency of the particle moving.

2.2 MEASUREMENT AND ANALYSIS OF HYDROCARBONS

The experimental procedure is similar in ethane [32], neopentane [29], and propene [33, 34] measurements. Infrared absorption spectra of these hydrocarbons were measured at the Canadian Light Source (CLS) far infrared beamline. The gas was held in a White-type multiple reflection cell, which gives a path length of 8.63 m (± 0.02 m). A small amount of hydrocarbon was added to the gas cell, and then the broadening gas was added until the desired total pressure was achieved. The gas cell was held at different temperatures and pressures to record the spectra. A Bruker IFS 125 HR Fourier transform spectrometer with a CaF₂ beam splitter and InSb detector were used to record the spectra of ethane, neopentane, and propene in the CH stretching region. A KBr beamsplitter and Ge:Cu detector in a QMC Instruments cryostat was used to record propene spectra for the band centered around 575 cm⁻¹. The spectra of *n*-butane were recorded with a Bruker IFS 120/125HR Fourier transform spectrometer at Old Dominion University. A KBr beam splitter and InSb detector were used, and the gas cell was a single pass 20 cm cell fitted with wedged CaF₂ windows.

The transmission spectra of ethane, neopentane, and *n*-butane were converted to cross sections, σ (cm²/molecule) using [36]:

$$\sigma(\nu, T) = -\frac{10^4 kT}{Pl} \ln \tau(\nu, T), \quad (24)$$

where $\tau(\nu, T)$ is the transmittance at wavenumber ν (cm⁻¹) and temperature T (K), P is the pressure (Pa) of the absorbing gas, l is the path length (m) and k (1.380649×10^{-23} JK⁻¹) is the Boltzmann constant.

2.2.1 Ethane

99.999% pure ethane with less than 6 ppm total hydrocarbon impurity was used in the gas cell. The samples were held at four different temperatures (203, 233, 263, 295 K) with broadening gas pressures of 10 Torr, 30 Torr, and 100 Torr. Hydrogen and helium, which are the main contributors

to the atmospheres of giant planets (For example, Saturn has a H₂ abundance of 93%, and He abundance of 7% [37]), were used as the broadening gases. A bandpass filter in the region 2650-3200 cm⁻¹ was used, and the pressures were selected to give suitable absorption in this region. The spectral resolution was chosen according to the total pressure: 0.005 cm⁻¹ (10 Torr), 0.01 cm⁻¹ (30 Torr), 0.04 cm⁻¹ (100 Torr), and 0.005 cm⁻¹ (pure sample). The background spectra were recorded at a spectral resolution of 0.04 cm⁻¹. 10 Torr and 1000 Torr Baratron pressure gauges were used to measure the pressures. The experimental conditions, temperature, ethane pressure, and total pressure for each spectrum are given in Table 1.

Table 1. Experimental conditions for each ethane spectrum. Table is from Dodangodage et al. [32]

Helium					
Temp (K)	Ethane (mTorr)	Total (Torr)	Temp (K)	Ethane (mTorr)	Total (Torr)
201.85	2.62	10.4	232.95	3.03	10.2
201.75	3.09	30.1	232.95	2.46	30.5
201.85	3.47	100.3	232.95	4.76	99.8
262.35	4.30	9.9	292.05	5.71	10.4
262.25	2.47	30.6	292.15	3.14	30.4
262.35	6.48	100.5	291.95	8.66	100.8
Hydrogen					
Temp (K)	Ethane (mTorr)	Total (Torr)	Temp (K)	Ethane (mTorr)	Total (Torr)
202.05	2.53	11	232.95	3.45	10.45
201.95	2.80	30.7	232.95	2.37	29.8
201.85	2.87	100	232.95	5.16	99.5
262.45	4.30	10.7	291.85	4.51	10.29
262.45	2.72	30.8	291.45	4.09	30.1
262.45	6.19	100.5	291.75	7.62	100.3
Pure Samples					
Temp (K)	Ethane (mTorr)	Total (Torr)	Temp (K)	Ethane (mTorr)	Total (Torr)
201.85	2.50	2.50	232.75	3.10	3.10
262.35	3.94	3.94	291.85	4.68	4.68

Ethane pressures were measured using a 10 Torr Baratron, not ideal for small pressures, resulting in some inaccuracies in pressure readings. Therefore, a calibration factor (C) was applied to Equation (24) to obtain more accurate cross-sections. The calibration factor is the ratio between the averaged integrated area of the Pacific Northwest National Laboratory (PNNL) spectra and the

integrated area from the recorded spectra. PNNL database has ethane spectra recorded at temperatures of 278 K, 298 K, and 323 K with 1 atm of nitrogen broadening gas. Hewett et al. [38] integrated area of the same spectral region can be used for calibration. The integrated areas for ethane in the region $2790 - 3092 \text{ cm}^{-1}$ are 28.365 , 28.048 , and $27.887 \times 10^{-18} \text{ cm}^2/\text{molecule}$ for 278, 298, and 323 K respectively and the average area is $28.1 \times 10^{-18} \text{ cm}^2/\text{molecule}$. Ethane pressures were corrected using this calibration factor and are shown in Table 1. The wavenumbers were calibrated by a factor of 0.99999486 by comparing the cross sections with pure spectra reported by Harrison et al. [39].

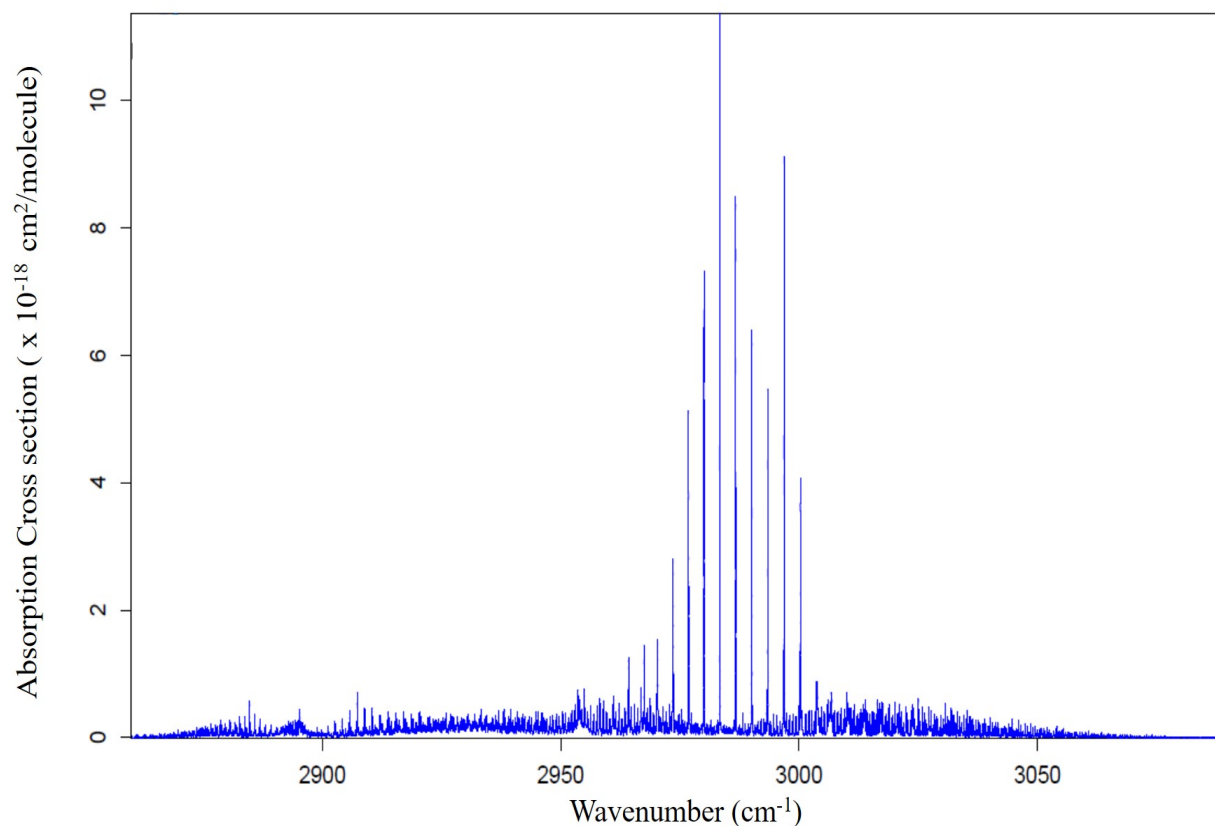


Figure 2. Absorption cross sections of ethane (about 9 mTorr of ethane in 100.3 Torr total pressure of H_2 and ethane at 291.75 K). This figure is taken from Dodangodage et al. [32].

Figure 2 shows the absorption cross sections of ethane broadened by hydrogen at 291.75 K

and total pressure of 100.3 Torr in the CH stretching region. This work reports 28 ethane spectra broadened by helium and hydrogen at four different temperatures at three total pressures and pure ethane spectra. These spectra are published as supplementary data files to Dodangodage et al. [32] and can be obtained from the MoLLIST (Molecular Line Lists, Intensities and SpecTra) website (<https://bernath.uwaterloo.ca/molecularlists.php>).

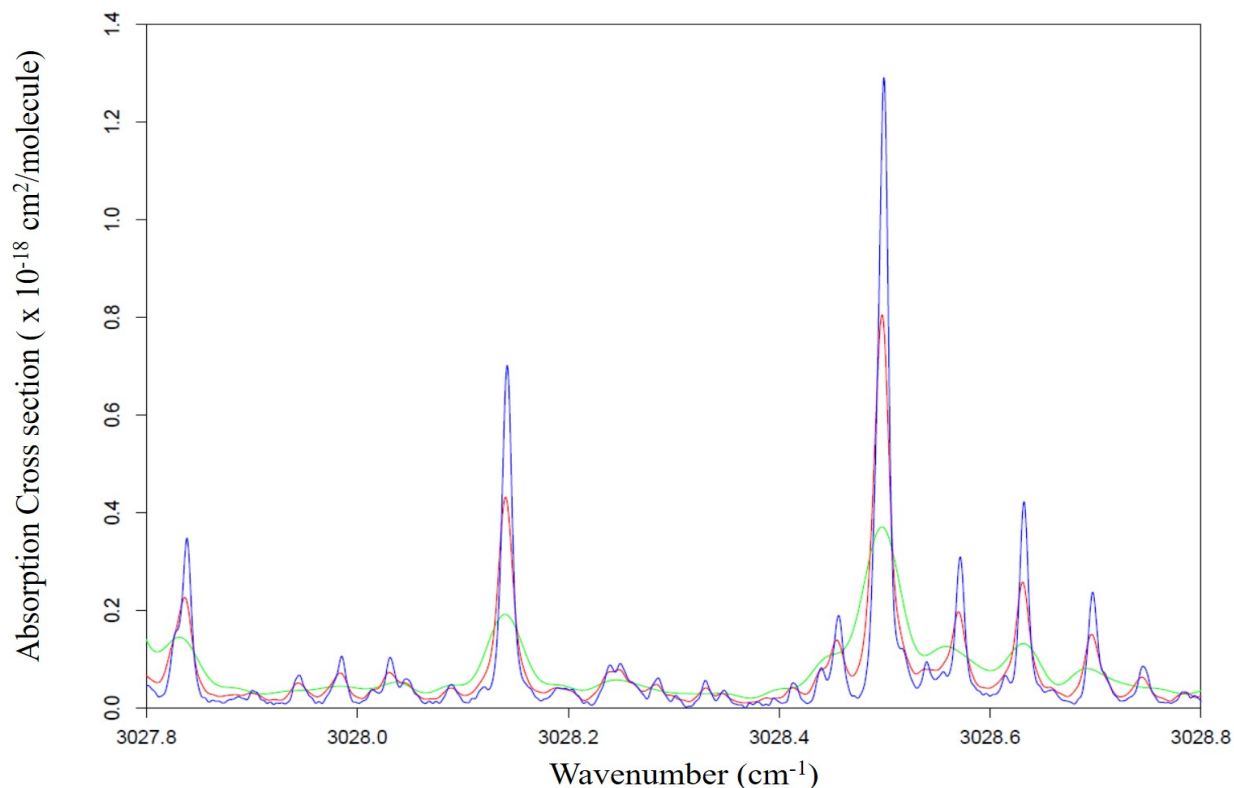


Figure 3. Absorption cross sections of ethane broadened by hydrogen with different pressures at 292 K. (Blue = 10.29 Torr, Red = 30.1 Torr, Green = 100.3 Torr). This figure is taken from Dodangodage et al. [32].

The effect of pressure on ethane cross sections is illustrated in Figure 3. The blue curve depicts the cross sections at 10.29 Torr, and the green curve gives cross sections at 100.3 Torr. As the pressure increases, the lines get smaller and wider. The pressure broadening is linear with pressure (Equation (22)). A similar effect can be seen on cross-sections broadened by helium as well.

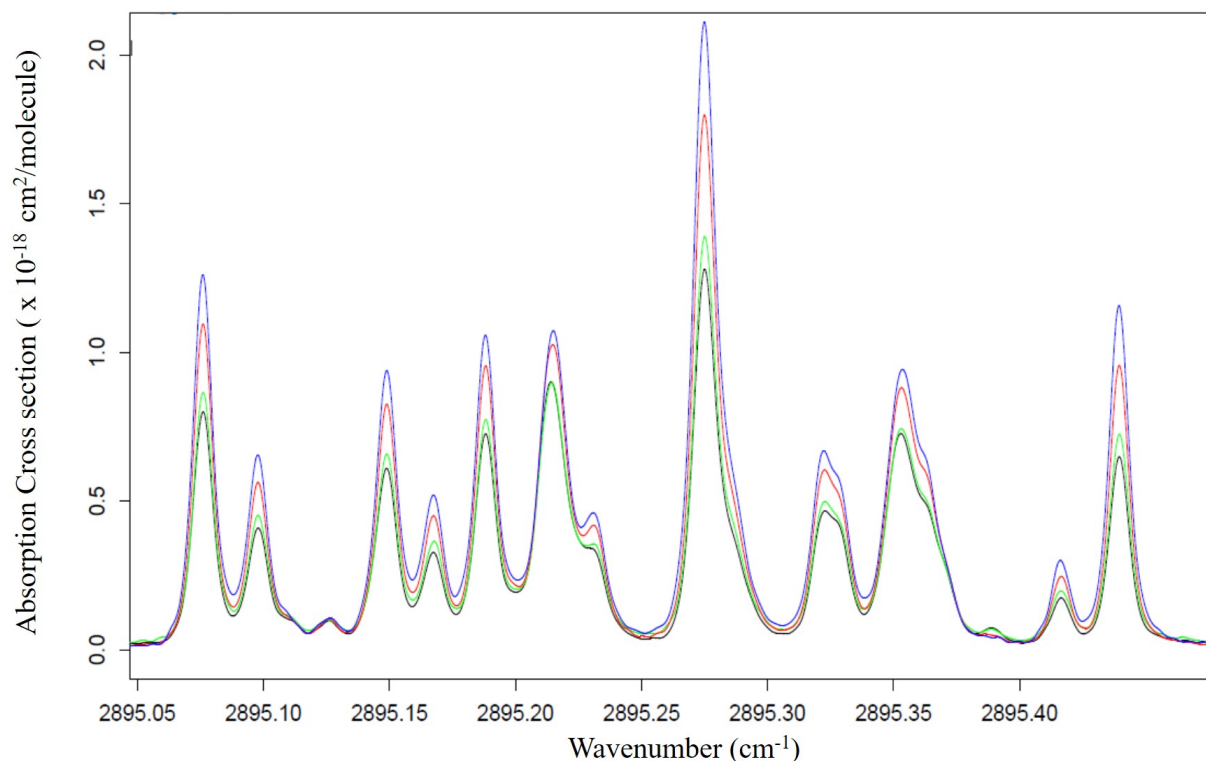


Figure 4. Absorption cross sections of ethane broadened by hydrogen for 10 Torr of total pressure at different temperatures. (Blue = 202.05 K, Red = 232.95 K, Green = 262.45 K, Black = 291.85 K). This figure is taken from Dodangodage et al. [32].

The effect of temperature on ethane cross sections is shown in Figure 4. Temperature affects mainly the population, and for these low J and K transitions, the intensity and population increase as temperature drops.

2.2.2 Neopentane

Neopentane spectra were recorded at four temperatures (202, 232, 265, 297 K) and three different total pressures (10, 30, 100 Torr). Nitrogen was chosen as the broadening gas as these data are aimed at infrared remote sensing in Titan's atmosphere, composed of 95% N_2 and 5% methane [6]. The spectral resolution was varied according to the total pressure: 0.003 cm^{-1} (pure sample), 0.003 cm^{-1} (10 Torr), 0.01 cm^{-1} (30 Torr), and 0.04 cm^{-1} (100 Torr) [29]. The background spectra were recorded at 0.05 cm^{-1} resolution, and Fourier interpolated to match higher resolution

spectra [29]. A 2500-3400 cm^{-1} bandpass filter was used to record the neopentane spectra in the CH stretching region, and the pressures were selected to give a strong absorption for the feature at 2960 cm^{-1} . The experimental conditions for each spectrum are shown in Table 2.

Table 2. Experimental conditions for each neopentane spectrum. The table is from Bernath et al. [29]

Temp (K)	Neopentane (mTorr)	Total (Torr)	Temp (K)	Neopentane (mTorr)	Total (Torr)
202.15	30.0	0.0300	265.05	44.7	0.0447
202.15	30.3	10.1	265.05	44.9	10
202.15	28.6	30.1	265.05	42.1	30
202.15	32.1	100	265.05	51.6	100.1
232.15	39.8	0.0398	297.25	46.2	0.0462
232.15	39.8	10	297.25	46.2	10.05
232.15	41.4	30.2	297.25	68.6	30.2
232.15	43.6	100.1	297.25	70.4	100.4

Another neopentane spectrum covering a wider spectral range (22.5 °C, 10.1 Torr of neopentane, and 19.99 cm path length) was recorded at Old Dominion University (ODU) for comparison. This spectrum was recorded with a spectral resolution of 0.01 cm^{-1} , and pressure was measured with an accuracy of about 1%. A factor of 0.99999893(54) was applied to the wavenumbers of CLS spectra. Comparison with the ODU spectrum showed that CLS pressure measurements were a factor of 3 low. These cross sections were re-calibrated by Bernath et al. [40].

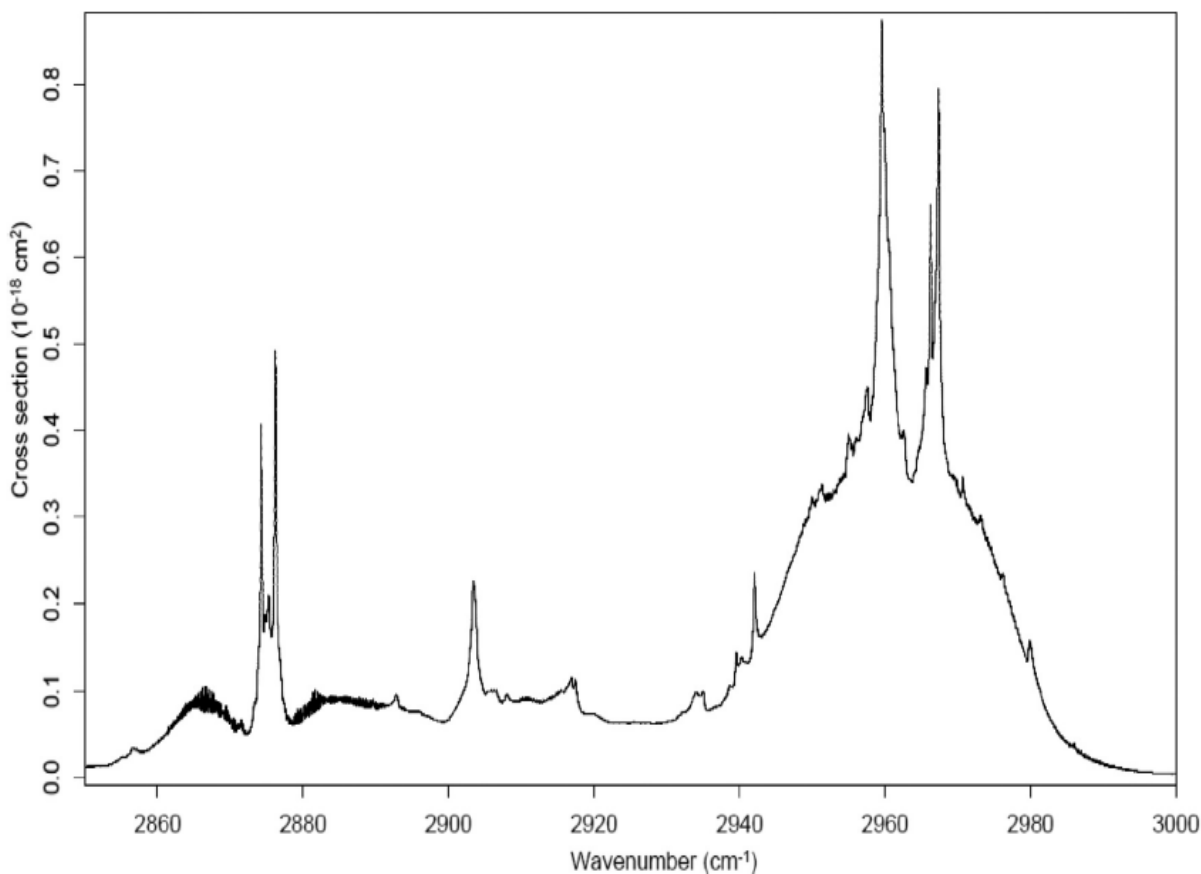


Figure 5. Absorption cross section of neopentane broadened by nitrogen at 202.15 K (32.1 mTorr of neopentane in 100 Torr of total pressure). This figure is taken from Bernath et al. [29].

Neopentane absorption cross sections in the CH stretching region with nitrogen as a broadening gas at 202.15 K and 100 Torr of total pressure are shown in Figure 5. All 16 cross-section files described in Table 2 are provided as supplementary files to Bernath et al. [29] and also can be found on the MoLLIST (Molecular Line Lists, Intensities and SpecTra) website.

Neopentane has 45 normal modes and 19 fundamental frequencies of vibration, of which only the t_2 modes are infrared active [29, 41, 42]. In the CH stretching region, there are five fundamental vibrational frequencies: $\nu_1(a_1) = 2909 \text{ cm}^{-1}$, $\nu_4(e) = 2955 \text{ cm}^{-1}$, $\nu_g(t_1) = 2942 \text{ cm}^{-1}$, $\nu_{13}(t_2) = 2959.6 \text{ cm}^{-1}$, $\nu_{14}(t_2) = 2876.2 \text{ cm}^{-1}$ [29]. An overview of the $\nu_{14}(t_2) = 2876.2 \text{ cm}^{-1}$ band of pure neopentane at 202.15 K is shown in Figure 6. The typical P-Q-R rotational structure of a molecule's allowed t_2 mode with T_d symmetry can also be seen in the $\nu_{14}(t_2)$ band. However, the Q-branch is doubled and has a weaker feature in the center.

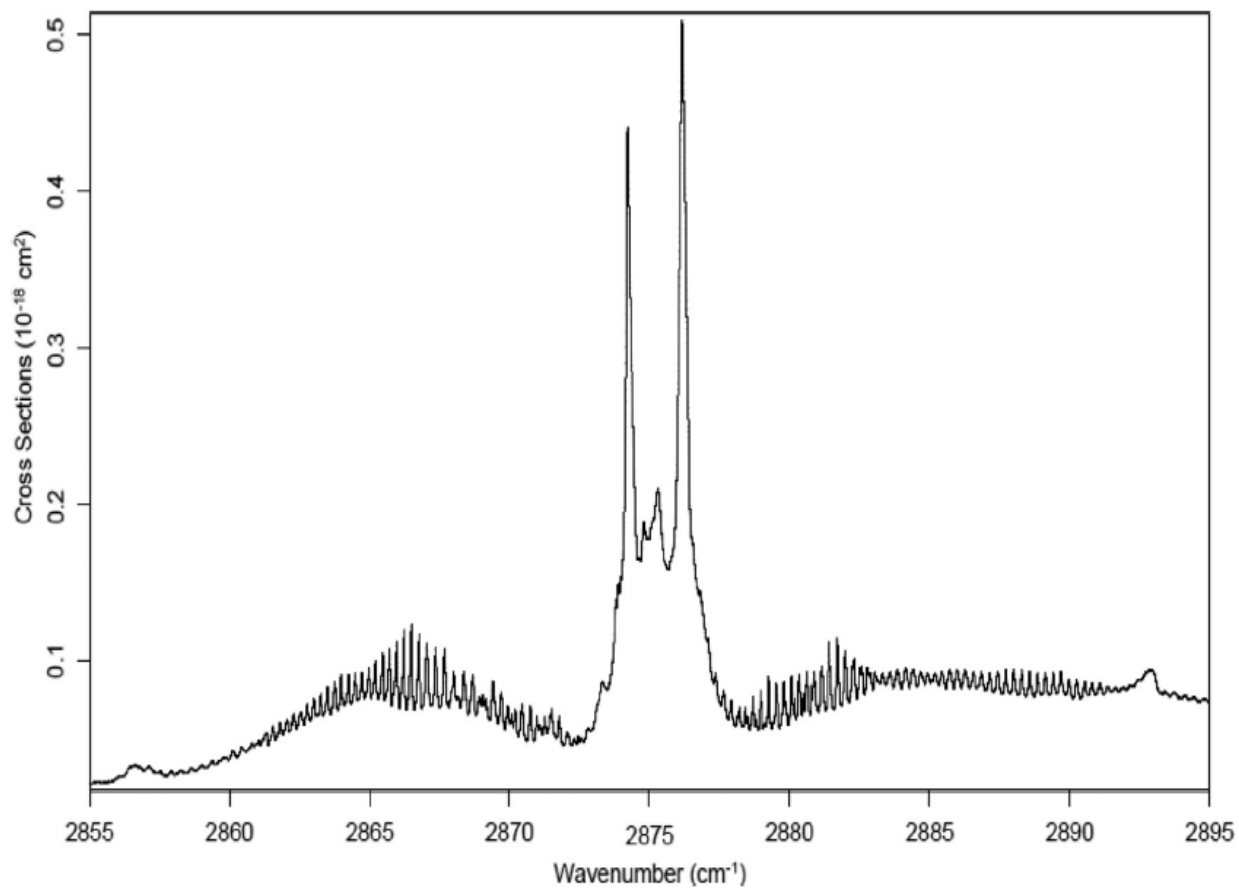


Figure 6. Overview of $\nu_{14}(t_2)$ band of pure neopentane at 202.15 K. This figure is taken from Bernath et al. [29].

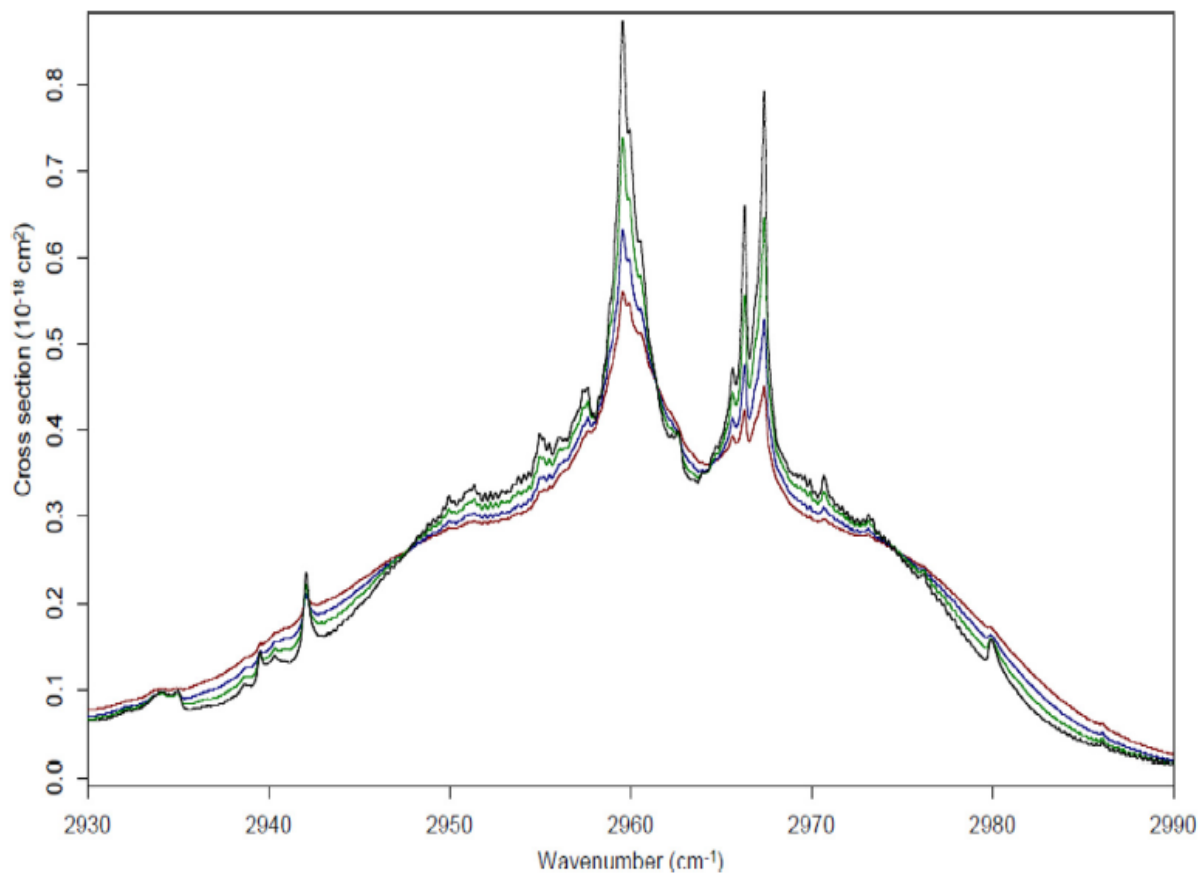


Figure 7. $\nu_{13}(t_2)$ band of neopentane broadened by nitrogen at different temperatures for 100 Torr of total pressure. (Red = 297 K, Blue = 265 K, Green = 232 K, Black = 202 K). This figure is taken from Bernath et al. [29].

Figure 7 illustrates the strong $\nu_{13}(t_2)$ band and also demonstrates the effect of temperature on neopentane cross sections. As temperature increases the population is drained from higher energy levels into lower ones resulting in sharpened and intensified spectral lines. However, Figure 7 shows that almost all the features increase in intensity as the temperature decreases; therefore, these are not due to vibrational hot bands.

The sharpest features seen in Figure 8 are rotational lines associated with the $\nu_{14}(t_2)$ band, and as depicted, the effect of pressure on the cross sections is small.

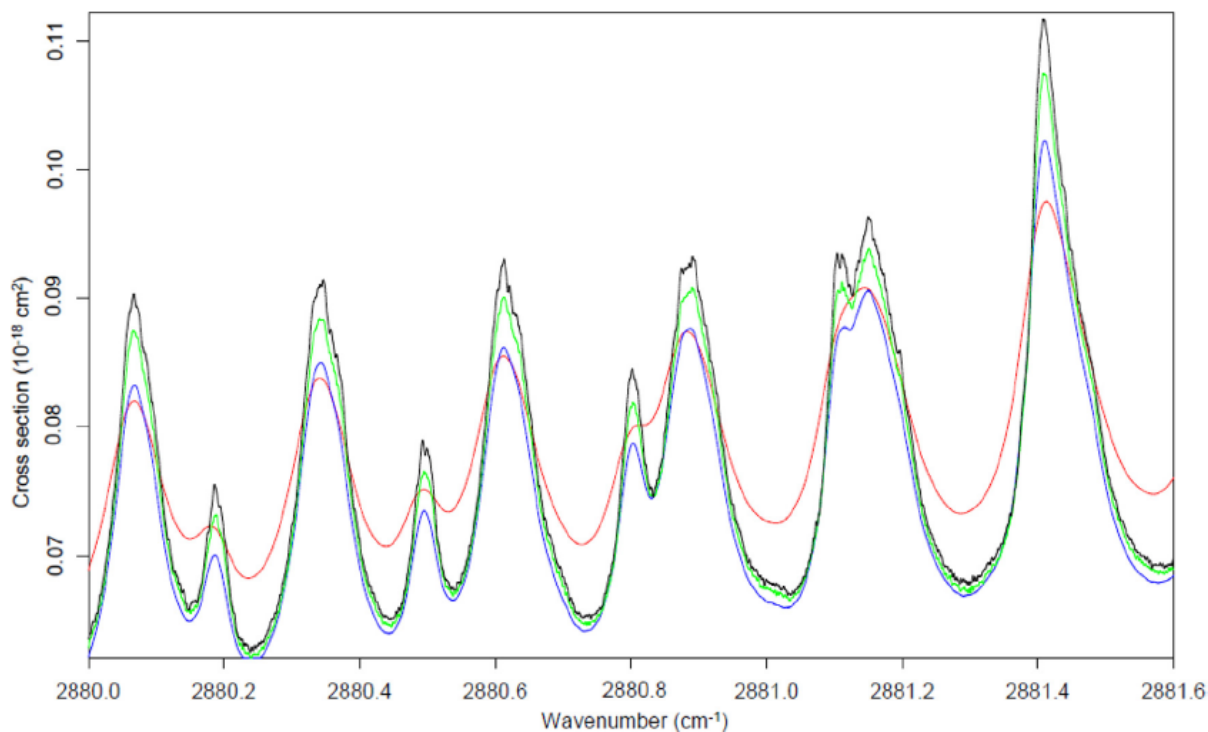


Figure 8. The effect of nitrogen broadening on rotational features of the neopentane $\nu_{14}(t_2)$ band at 202.15 K. Black curve is for pure neopentane. (Green = 10 Torr, Blue = 30 Torr, Red = 100 Torr). This figure is taken from Bernath et al. [29].

2.2.3 Propene

Propene spectra broadened by hydrogen, helium, and nitrogen in the CH stretching region were recorded along with those broadened by nitrogen to cover the band centered around 575 cm^{-1} . Similar to others, propene spectra were recorded at four different temperatures and three different total pressures, including pure propene spectra. Spectral resolutions of 0.003 cm^{-1} (Pure sample, 10 Torr), 0.01 cm^{-1} (30 Torr), 0.04 cm^{-1} (100 Torr) were selected. The experimental conditions of propene spectra in the CH stretching region are given in Table 3 and in the $450\text{-}1250\text{ cm}^{-1}$ region are given in Table 4. No wavenumber calibration was required for the spectra recorded in the CH stretching region with helium and nitrogen broadening gases as it matched the HITRAN [43] N_2O line positions within about 0.0003 cm^{-1} . The spectra broadened by hydrogen in the CH stretching region were calibrated by a factor of 0.999999380 after comparing the two pure spectra at room temperature. No calibration was required for the spectra broadened by nitrogen.

Table 3. Experimental conditions for each propene spectrum in the CH stretching region. This table is from Dodangodage et al. [33] and Bernath et al. [34]

Hydrogen					
Temp (K)	propene (mTorr)	Total (Torr)	Temp (K)	propene (mTorr)	Total (Torr)
202.15	258.7	10.3	232.15	352.1	10.0
202.05	249.4	30.4	232.15	314.1	30.3
202.05	247.6	100.3	232.15	341.4	100.4
265.05	409.6	10.0	297.15	484.3	10.09
265.05	448.5	30.8	297.25	594.5	30.0
265.05	481.0	100.2	297.35	506.8	100.0
Helium					
Temp (K)	propene (mTorr)	Total (Torr)	Temp (K)	propene (mTorr)	Total (Torr)
201.95	257.5	10.6	232.15	315.4	10.47
201.95	248.3	30.2	232.15	334.4	30.2
201.95	248.3	100.3	232.05	347.4	100.3
265.05	408.2	10.1	296.85	487.5	10.32
265.05	446.4	30.1	296.85	503.1	30.5
265.05	479.3	100.2	296.85	504.4	100.2
Nitrogen					
Temp (K)	propene (mTorr)	Total (Torr)	Temp (K)	propene (mTorr)	Total (Torr)
201.95	256.8	10.2	232.15	348.8	10.2
201.95	250.8	30.1	232.15	345.7	30
202.25	247.9	100.2	232.25	340.3	100.2
265.05	405.9	10.2	296.75	483.5	9.9
265.05	445.6	30.3	296.85	502.9	30.2
265.15	479.2	100.6	296.85	506	100.2
Pure Sample					
Temp (K)	propene (mTorr)	Total (mTorr)	Temp (K)	propene (mTorr)	Total (mTorr)
296.75	482.9	482.9	297.85	488.0	488.0
265.15	411.8	411.8	232.15	353.5	353.5
202.15	260.0	260.0			

Table 4. Experimental conditions for each propene spectrum in the 450-1250 cm^{-1} region. This table is from Bernath et al. [34]

Nitrogen					
Temp (K)	propene (mTorr)	Total (Torr)	Temp (K)	propene (mTorr)	Total (Torr)
201.75	52.5	9.939	232.05	75.3	10.3
201.75	81.9	30.2	232.05	100.6	30.7
201.75	105.2	100.4	232.05	139	100.1
265.25	96.8	10.2	294.35	103.7	10.0
265.25	119.2	30.1	294.35	128.5	31.2
265.25	148.6	100.0	294.35	153.9	100.2

Propene is a molecule with C_s symmetry and has 21 fundamental frequencies [44, 45], and six of them are in the CH stretching region ($\nu_1 = 3091.62 \text{ cm}^{-1}$, $\nu_2 = 3015 \text{ cm}^{-1}$, $\nu_3 = 2991.03 \text{ cm}^{-1}$, $\nu_4 = 2973 \text{ cm}^{-1}$, $\nu_5 = 2931.46 \text{ cm}^{-1}$, and $\nu_{15} = 2954.3 \text{ cm}^{-1}$ [45]). Figure 9 illustrates the propene absorption cross sections broadened by helium at room temperature. The absorption cross-sections broadened by nitrogen at 202 K are shown in Figure 10. Although the cross-sections broadened by nitrogen focus on the band 575 cm^{-1} , recorded spectra cover the entire 450-1250 cm^{-1} range. The spectra recorded in the 450-1250 cm^{-1} region have considerable channeling (sinusoidal fringing) and were reduced using interactive software at the Canadian Light source. This channeling behaves like "noise" and reduces the signal-to-noise ratio by a factor of about 5. The cross-sections of pure samples in this region contained strong channeling and were not reported. Absorption cross sections broadened by helium and nitrogen in the CH stretching region are included in 25 files and are published as supplementary files to Dodangodage et al. [33]. Cross sections broadened by nitrogen in the 450-1250 cm^{-1} region and broadened by hydrogen along with pure propene spectra in the CH stretching region are included in 28 files published as supplementary files to Bernath et al. [34]. All the cross sections are also available on the MoLLIST (Molecular Line Lists. Intensities and SpecTra) website.

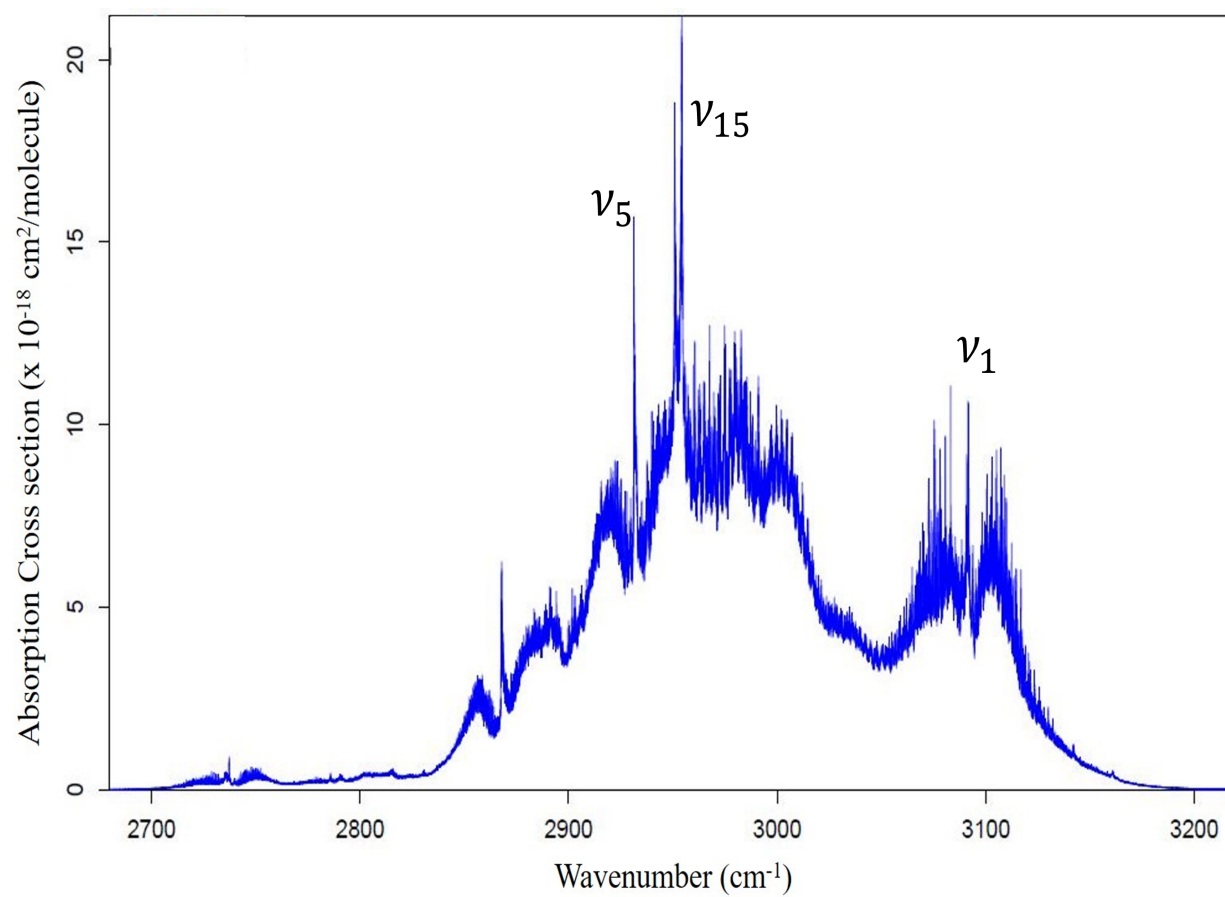


Figure 9. Absorption cross sections of propene in the CH stretching region. The spectrum is recorded at 296.85 K with a propene pressure of 503.1 mTorr and 30.5 Torr of total pressure with helium. This figure is taken from Dodangodage et al. [33].

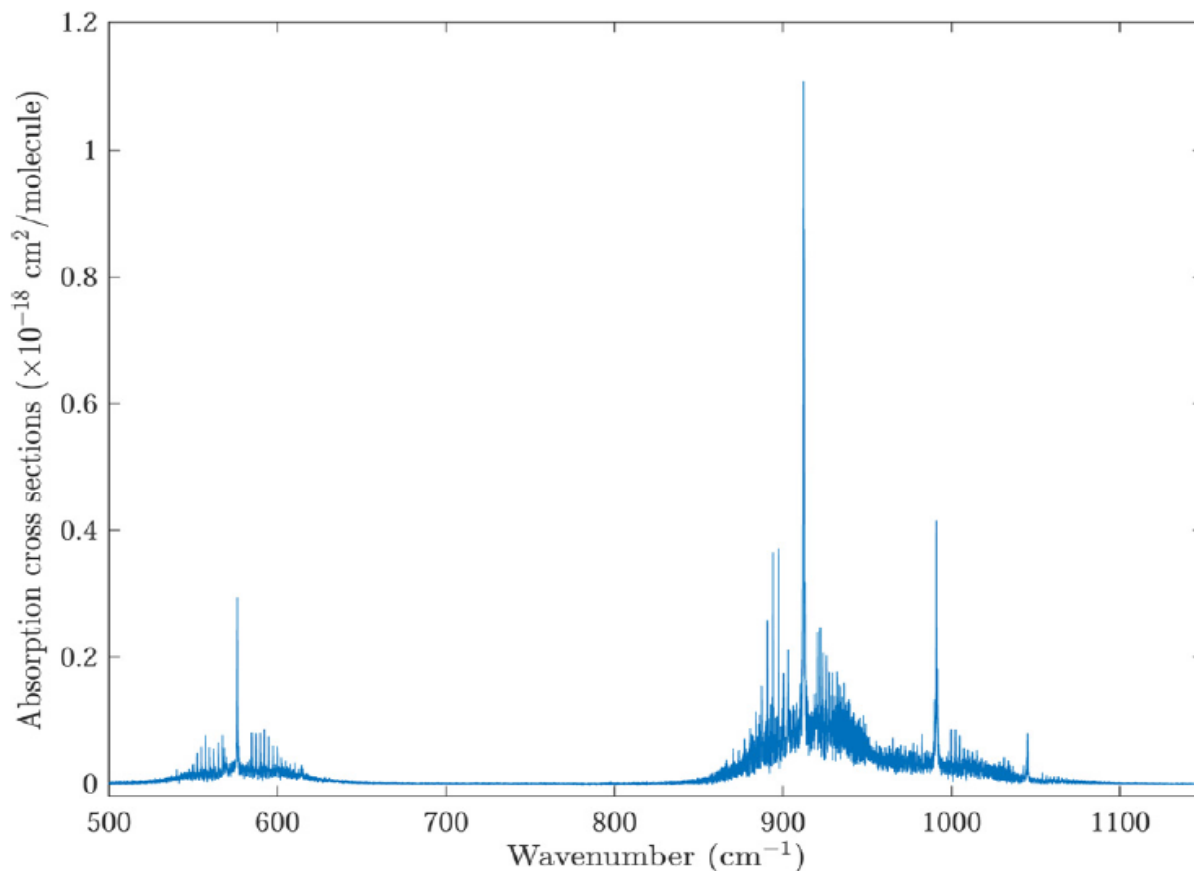


Figure 10. Absorption cross sections of propene in the 450-1250 cm^{-1} stretching region. The spectrum was recorded with a propene pressure of 105.2 mTorr and a total pressure of 100.4 Torr of nitrogen at 201.75 K. This figure is taken from Bernath et al. [34].

The integrated areas of strong fundamental bands are used for calibration as they are approximately constant and independent of temperatures [46]. The 2675-3210 cm^{-1} region was selected to calculate the integrated areas and compare with our spectra focused on the CH stretching region. The Pacific Northwest National Laboratory (PNNL) database has composite spectra of propene at 278, 298, and 323 K temperatures. These spectra were recorded by adding propene in a nitrogen mixture to make a total pressure of 760 Torr in a cell with a path length of 19.94 cm. The spectral resolution of PNNL spectra is 0.112 cm^{-1} . The integrated areas range from 16.80×10^{-18} to 16.82×10^{-18} $\text{cm}^2/\text{molecule}$ with an average value of 16.82×10^{-18} $\text{cm}^2/\text{molecule}$. Es-sebbar et al. [47] recorded spectra with 10% of propene in a nitrogen mixture in a gas cell of a path length of 10 cm at various temperatures above 296 K. These spectra have spectral resolutions of 0.09 cm^{-1}

and 0.18 cm^{-1} for the regions $400\text{-}3200 \text{ cm}^{-1}$ and $3200\text{-}6000 \text{ cm}^{-1}$ respectively. The integrated area of the cross sections at 296 K is $16.49 \times 10^{-18} \text{ cm/molecule}$. The integrated areas of our cross sections broadened by helium and nitrogen in the same spectral region range from 16.76×10^{-18} to $16.98 \times 10^{-18} \text{ cm/molecule}$ with an average of $16.89 \times 10^{-18} \text{ cm/molecule}$ [33]. The cross sections broadened by hydrogen and pure have integrated areas ranging from 16.49×10^{-18} to $16.94 \times 10^{-18} \text{ cm/molecule}$ with an average of $16.76 \times 10^{-18} \text{ cm/molecule}$. The integrated areas of the PNNL and Es-sebbar et al. [47] differ by 0.42% and 2.38% from Dodangodage et al. [33]. PNNL integrated areas differ by 0.36% from Bernath et al. [34].

Table 5. Comparison of propene integrated areas in the region $800\text{-}1100 \text{ cm}^{-1}$. This table is from Bernath et al. [34]

Source	Integrated area ($\times 10^{-18} \text{ cm/molecule}$)
JPL ^a at 298 K	8.79 ± 0.47
Es-sebbar et al. ^b at 296 K	9.14
PNNL ^c at 278, 298, 323 K	9.41 ± 0.01
This work ^d at 294.35 K	9.13 ± 0.09^e
JPL ^a at 270 K	8.93 ± 0.47
This work ^d at 265.25 K	8.89
JPL ^a at 230 K	9.21 ± 0.49
This work ^d at 232.05 K	9.30
This work ^d at 201.75 K	9.38 ± 0.21^f

^a Ref. [45]

^b Ref. [47]

^c Ref. [48]

^d Ref. [34]

^e Average integrated area of two total pressures.

^f Average integrated area of three total pressures.

The spectra focused on the 575 cm^{-1} band extends to 1250 cm^{-1} , and $800\text{-}1100 \text{ cm}^{-1}$ region was integrated to compare with Jet Propulsion Laboratory (JPL) spectra reported by Sung et al.

[45], Es-sebbar et al. [47] and PNNL [48], and are shown in Table 5. Our cross sections at room temperature agree well with the Es-sebbar et al. [47]. Our data and JPL vary with temperature, but PNNL shows no temperature dependence. Based on the range of values shown in Table 5, our work has an accuracy of about 5%.

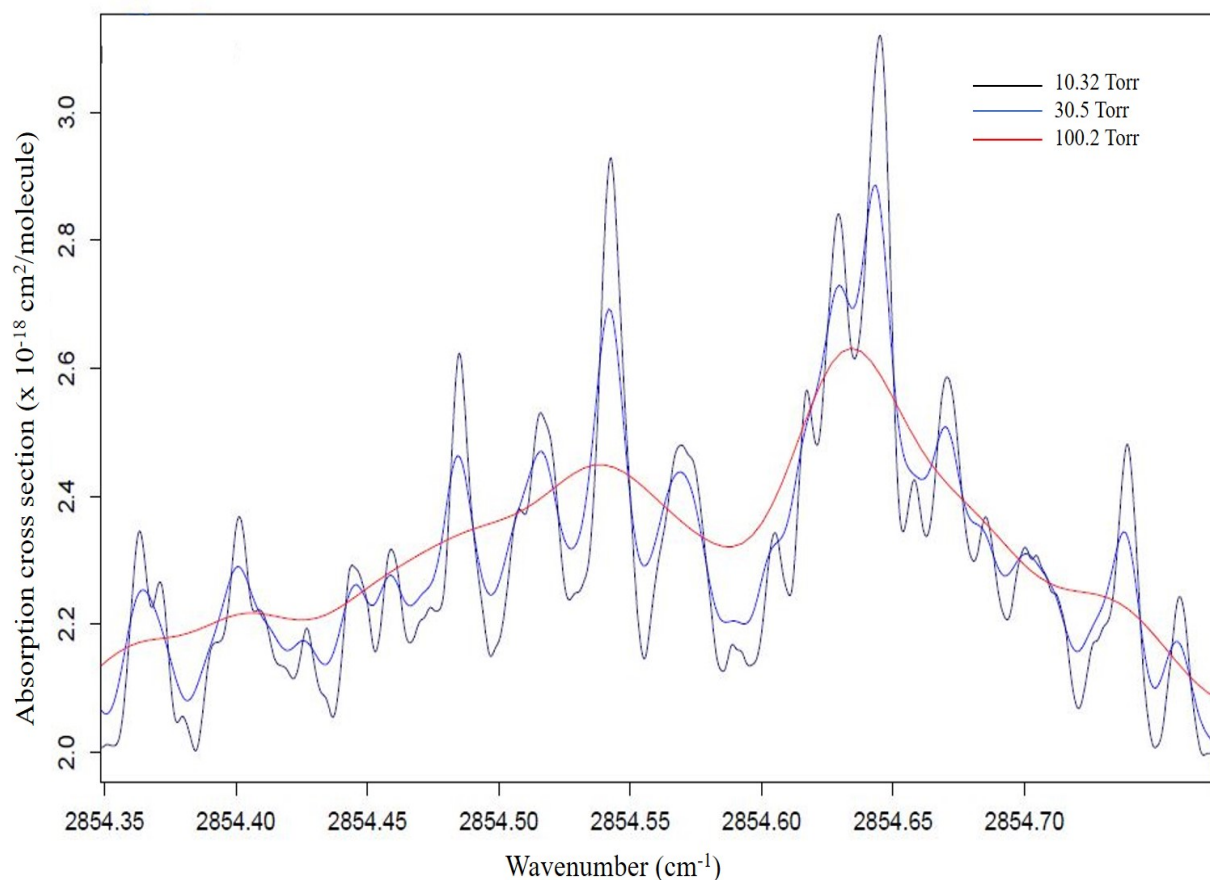


Figure 11. Absorption cross sections of propene broadened by helium at different total pressures at 295 K. (Black = 10.32 Torr, Blue = 30.5 Torr, Red = 100.2 Torr). This figure is taken from Dodangodage et al. [33].

The effect of pressure on propene cross-sections is shown in Figure 11. As the pressure increases, the peaks get smaller, and lines get broadened. The effect of nitrogen and hydrogen is similar. Figure 12 shows the pressure broadening effect on propene lines by nitrogen near 600

cm^{-1} . The vibration-rotation lines are nearly fully resolved in the propene spectrum at 10 Torr (black curve on Figure 12) and only slightly broadened. At 100 Torr (red curve on Figure 12), the rotational structure is completely washed out by pressure broadening. The effect of temperature is shown in Figure 13. The temperature mainly affects the population, and for the low J and K transitions, the intensity increases, and the population increases as the temperature drops.

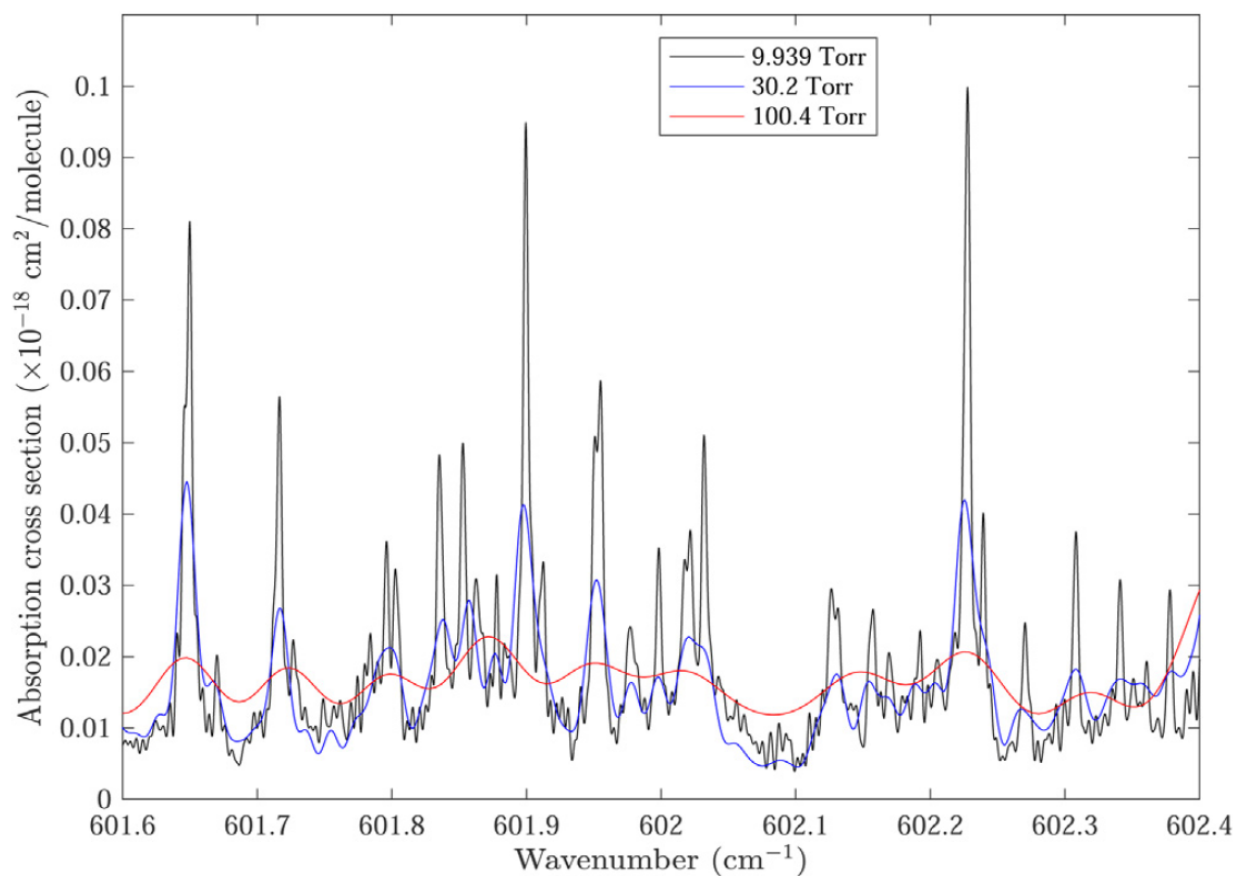


Figure 12. Absorption cross sections of propene broadened by nitrogen at different total pressures at 202 K. (Black = 9.939 Torr, Blue = 30.2 Torr, Red = 100.4 Torr). This figure is taken from Bernath et al. [34].

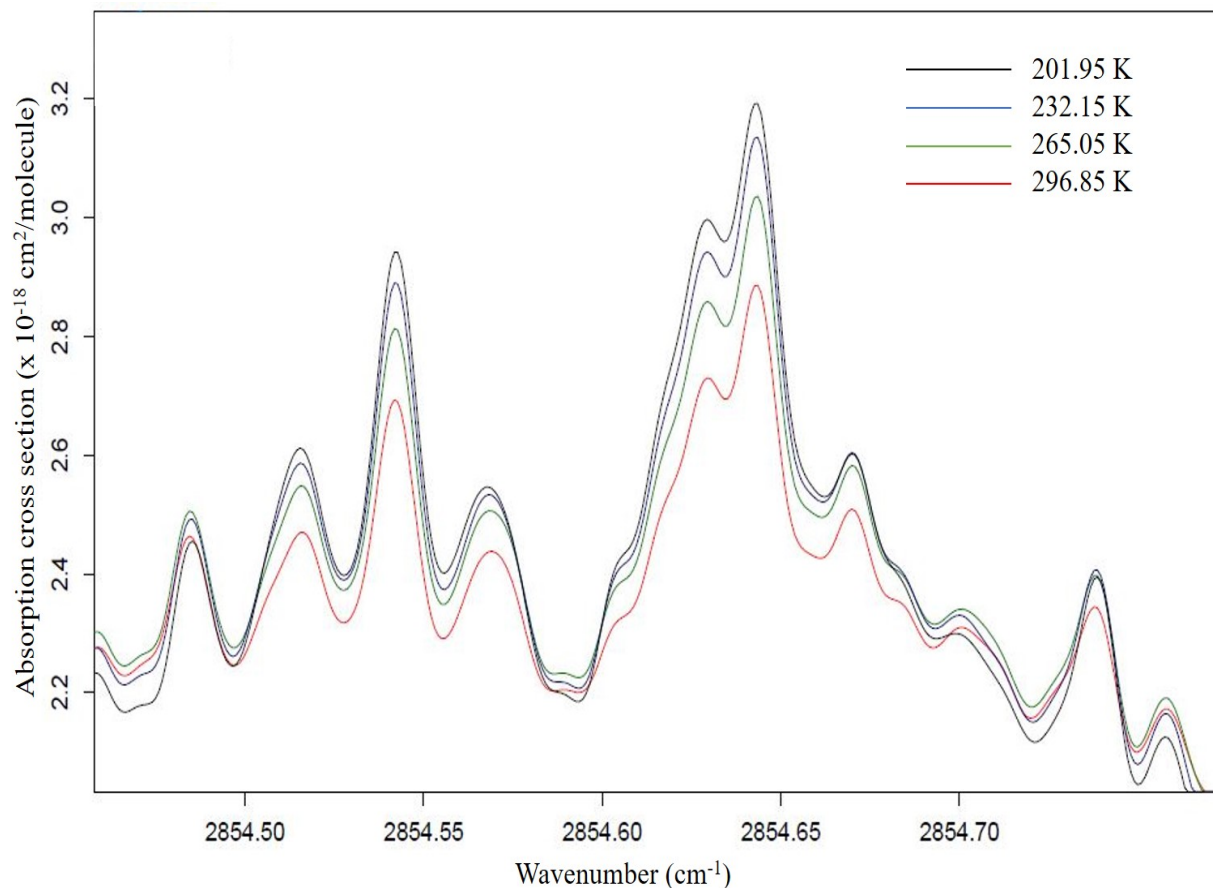


Figure 13. Absorption cross sections of propene broadened by helium at different temperatures for 30 Torr of total pressure. (Black = 202 K, Blue = 232 K, Green = 265 K, Red = 297 K). This figure is taken from Dodangodage et al. [33].

2.2.4 *n*-Butane

The spectra for *n*-butane were recorded at Old Dominion University with a Bruker IFS 120/125 HR Fourier transform spectrometer at a resolution of 0.04 cm^{-1} . An internal glowbar source, KBr beamsplitter, and liquid N_2 cooled InSb detector were used, and the *n*-butane sample was kept in a single pass 20 cm cell fitted with wedged CaF_2 windows. The cell was cooled with a liquid ethanol circulator to obtain low temperatures. Two *n*-butane spectra were recorded at two different temperatures, 294.2 K and 230.5 K, between 2800 and 3050 cm^{-1} . 512 scans were recorded at each temperature for the sample and background scans and were averaged. Figure 14 shows the absorption cross sections for the two temperatures in the CH stretching region.

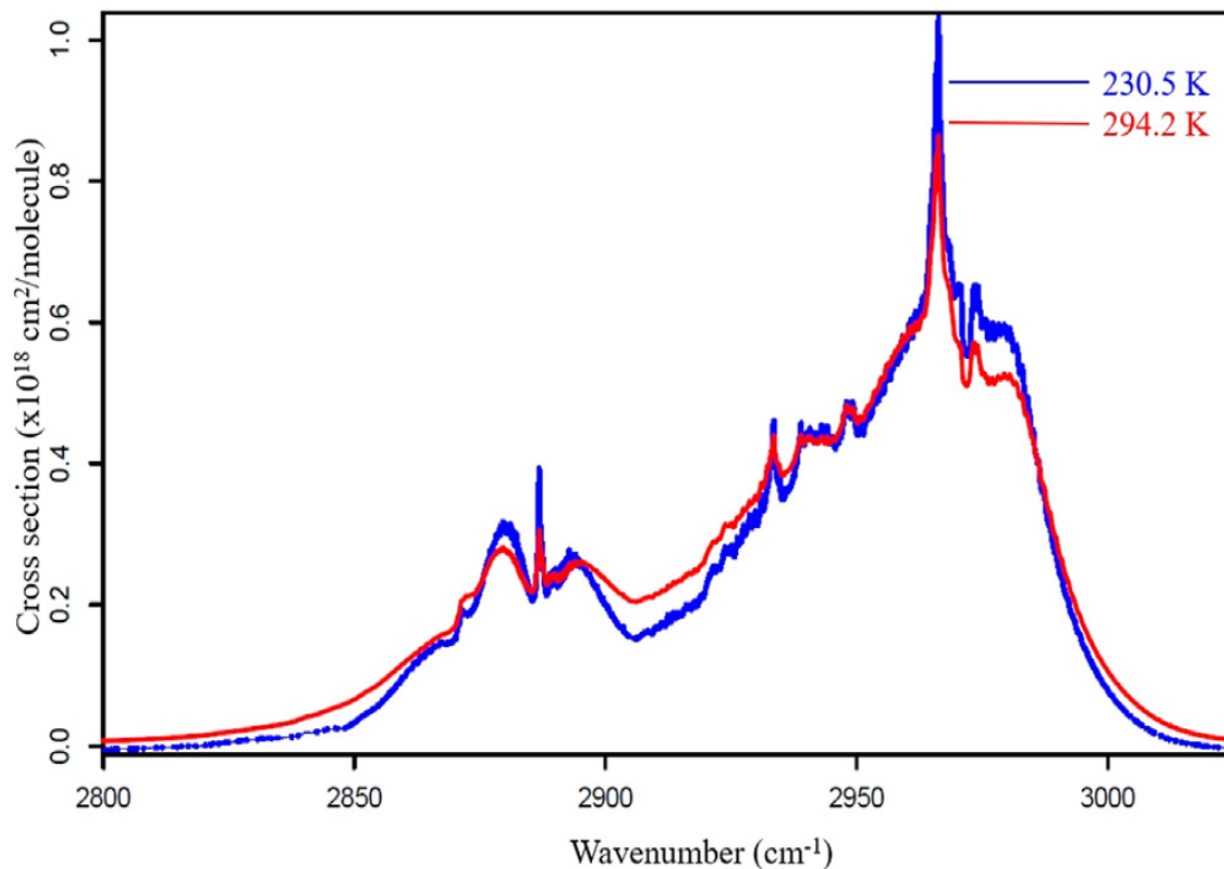


Figure 14. Absorption cross sections of *n*-butane in the CH stretching region at two different temperatures (Blue = 230.5 K, Red = 294.2 K). This figure is taken from Sorensen et al. [35].

n-butane has two main conformations: *s*-trans and *gauche*, which have C_{2h} and C_2 symmetry with 11 and 21 allowed Raman modes and 10 and 21 infrared active modes, respectively. In the CH stretching region, there are 10 vibrational modes; C_{2h} symmetry includes $\nu_1 - \nu_3$ (a_g), $\nu_{12} - \nu_{13}$ (a_u), $\nu_{20} - \nu_{21}$ (b_g), and $\nu_{27} - \nu_{29}$ (b_u), while C_2 symmetry has $\nu_1 - \nu_3$, ν_{12} , and ν_{13} (a) and ν_{20} , ν_{21} , $\nu_{27} - \nu_{29}$ (b) modes [49]. The wavenumber of the spectra recorded at 294.2 K and 230.5 K were calibrated by factors of 0.999995689(16) and 0.999995727(14), respectively, using CO_2 lines between 2323 to 2348 cm^{-1} from the HITRAN database [50]. *n*-butane spectra were calibrated to match the low-resolution spectra obtained by PNNL at 296 K, using the integrated area between 2776.298 - 3042.959 cm^{-1} . Figure 15 shows the CH_2 symmetric stretch (ν_2) centered around 2886 cm^{-1} recorded at a temperature of 230.5 K. P, Q, and R rotational structure is clearly visible in Figure 15.

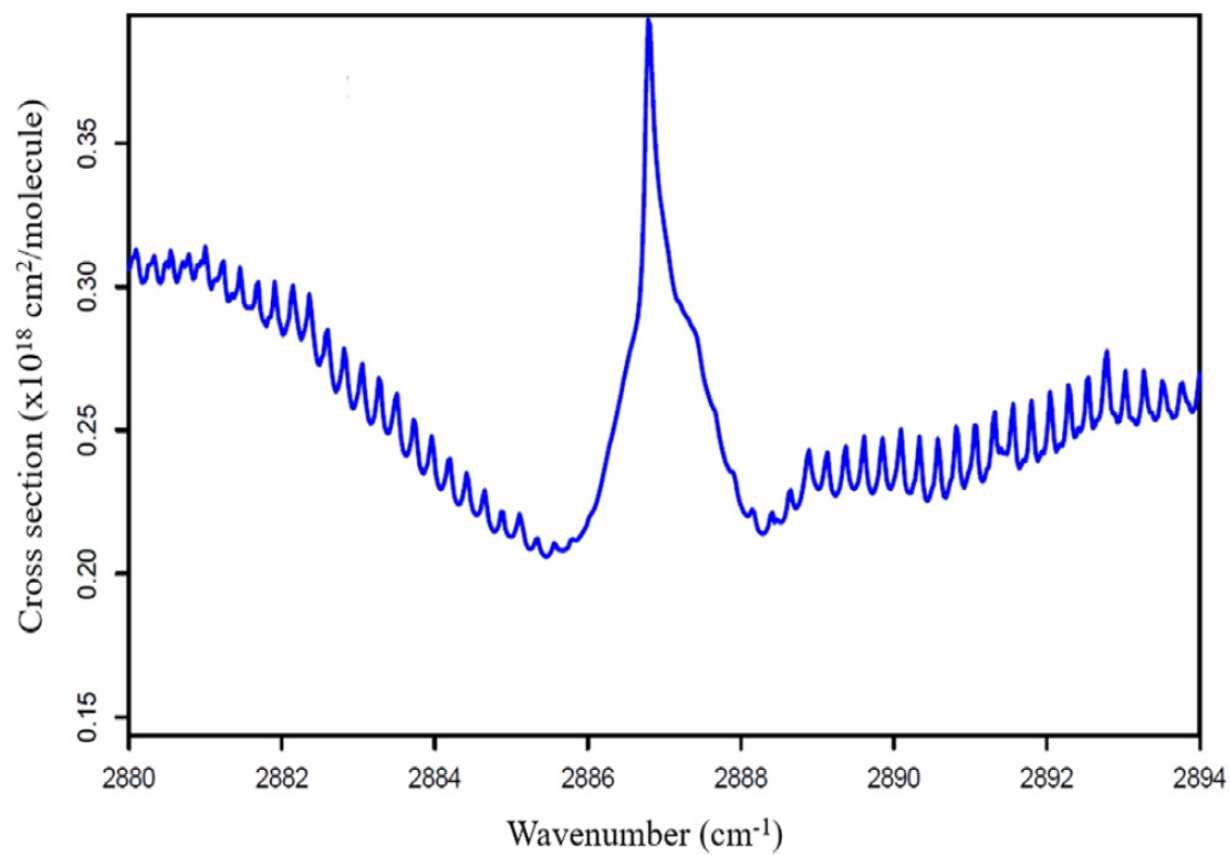


Figure 15. *n*-butane cross sections at 230.5 K showing the CH₂ symmetric stretch (ν_2) centered around 2886 cm⁻¹. This figure is taken from Sorensen et al. [35].

CHAPTER 3

MOLECULES IN EARTH'S ATMOSPHERE

The components comprising Earth's atmosphere play a pivotal role in atmospheric chemistry. It is essential to understand the chemistry and dynamics of the atmosphere to predict the weather and climate. Among the vast number of molecules present in Earth's atmosphere, substances like ozone hold particular significance due to their crucial role in sustaining the planet's habitability. However, natural phenomena, such as volcanic eruptions, alongside anthropogenic activities and biomass burning, introduce numerous molecules into the atmosphere, significantly impacting its dynamics and composition. The precise measurement and ongoing monitoring of these atmospheric constituents and their evolving trends are significant in proactively addressing and mitigating potential challenges associated with future weather and climate scenarios.

In this chapter, two molecules, HOCl [51] and HFC-32 [52], are examined using data from the Atmospheric Chemistry Experiment (ACE). R. Dodangodage conducted formal analysis and visualization for both publications. The initial draft for Bernath et al. [51] was authored by Dr. Bernath, and for Dodangodage et al. [52], it was composed by R. Dodangodage. Chris Boone from the Department of Chemistry, University of Waterloo, performed the data retrievals from the ACE satellite. J. Crouse from the Department of Chemistry, University of Waterloo, and J. J. Harrison from the Department of Physics and Astronomy, University of Leicester, managed the data curation. All authors contributed to the writing, reviewing, and editing of the manuscripts.

3.1 ATMOSPHERIC CHEMISTRY EXPERIMENT (ACE)

Launched by NASA on August 12, 2003, the Atmospheric Chemistry Experiment (ACE), also known as SCISAT, is a long-standing Canadian satellite mission [3]. The mission's primary objective is to investigate atmospheric chemistry and dynamics related to stratospheric ozone depletion. With a track record spanning two decades and ongoing operations, ACE has played a crucial role in studying changes in atmospheric composition [53]. ACE currently provides data for 44 molecules and 23 isotopologues [54].

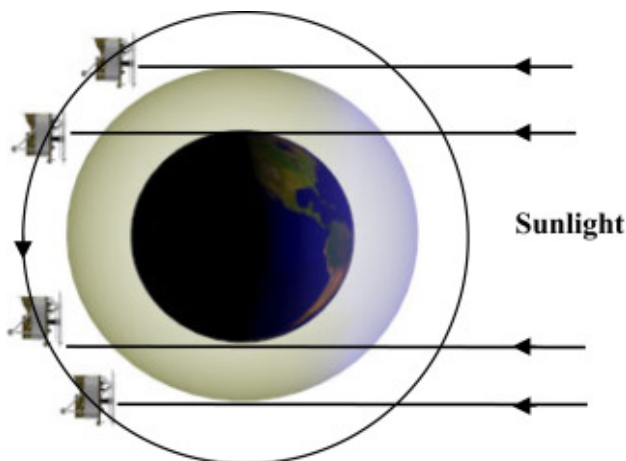


Figure 16. Limb viewing geometry of ACE satellite. The figure is from Bernath [3].

The satellite orbits at an altitude of 650 km, with an inclination of 73.9° to the equator. The latitude of the satellite repeats annually, owing to the selected inclination angle. With an orbital period of 97.6 minutes, the satellite captures 30 daily occultations during sunrise and sunset. The instrument records atmospheric absorption spectra as it observes the sun through the limb of the atmosphere. This limb viewing geometry facilitates the acquisition of altitude profiles for each molecule's volume mixing ratios (VMRs), providing ACE with a superior vertical resolution of 3–4 km. Figure 16 illustrates the ACE satellite's orbit around Earth, capturing measurements during sunrise and sunset while observing the sun through the atmosphere.

Equipped with three onboard instruments, ACE features Maestro, Imager, and FTS. Maestro, a spectrophotometer, incorporates two spectrographs covering the wavelength ranges of 285–550 nm and 525–1020 nm [3]. Additionally, the satellite has two visible and near-infrared imagers centered at 0.525 and $1.02 \mu\text{m}$, respectively, for measuring atmospheric extinction [3]. The primary instrument on board, the Fourier Transform Spectrometer (ACE-FTS), features a spectral resolution of 0.025 cm^{-1} , covering the range of $750\text{--}4400 \text{ cm}^{-1}$.

The ongoing data collection from 2004 to the present provided by ACE is invaluable for understanding the dynamics and trends of atmospheric molecules [53]. The process involves recording high-quality atmospheric transmission spectra as an initial step, then calculating atmospheric transmission using the Beer-Lambert law, spectroscopic line parameters, and absorption cross-sections. Subsequently, temperature, pressure, and tangent altitude profiles are retrieved using CO_2 absorption lines. The VMR profiles of atmospheric constituents are then retrieved by keeping temperature and pressure fixed. The retrieval process utilizes a preselected set of microwindows [54], and the

VMR profiles for all contributing molecules within a given microwindow are fitted simultaneously [54].

3.2 MONTREAL PROTOCOL AND STRATOSPHERIC OZONE DEPLETION

Ozone in the stratosphere serves as a barrier, preventing UV radiation in the 200–300 nm range from reaching Earth’s surface. Molina and Rowland [55] were the first to demonstrate that chlorine atoms, released through the photolysis of chlorofluorocarbons (CFCs), play a crucial role in destroying stratospheric ozone. The process involves Cl atoms reacting with ozone (O_3) to produce ClO, which then reacts with O atoms, regenerating Cl atoms and consequently depleting stratospheric O_3 . This cyclic process is commonly referred to as the ClO_x cycle.

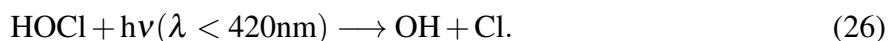
Implemented in 1987, the Montreal Protocol [56] is designed to safeguard the ozone layer by progressively eliminating the production and use of ozone-depleting substances (ODSs). This systematic phase-out is structured under specific schedules for developing (Article 5) and developed countries (non-Article 5). The global phase-out of chlorofluorocarbons (CFCs) has been universally implemented. Hydrochlorofluorocarbons (HCFCs), introduced as substitutes for CFCs, undergo reactions with OH radicals, reducing atmospheric lifespan. While HCFCs still reach the stratosphere and react with ozone, developed countries have initiated the phase-out of HCFCs, a process anticipated to extend globally by 2031. Hydrofluorocarbons (HFCs), with minimal ozone-depleting potential [57], have replaced HCFCs. However, the significant Global Warming Potentials (GWPs) [58] of HFCs indirectly contribute to ozone destruction by influencing the stratosphere’s temperature. In 2016, the Kigali Amendment was introduced to the Montreal Protocol, aiming to reduce the production of HFCs with high GWPs [59]. Developed countries began decreasing HFC production and consumption in 2019, targeting a 15% reduction by 2036. Simultaneously, developing countries are mandated to achieve a 15-20% reduction by 2045-2047.

3.3 HOCl

Hypochlorous acid (HOCl) is a minor chlorine-containing reservoir molecule formed by the reaction,

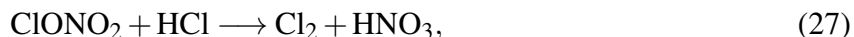


HO_2 is generated by the reaction of OH with O_3 . HOCl is destroyed by photolysis with wavelengths shorter than 420 nm,



HOCl plays a significant role in the polar stratosphere. Chlorine reservoir molecules like ClONO₂

and HCl are converted to Cl₂ and HOCl in the presence of polar stratospheric clouds (PSCs) during cold polar nights,



In the spring, Cl₂ and HOCl are converted to Cl atoms by photolysis. These Cl atoms go on to destroy O₃ and form ClO. The O atom abundance is too low to destroy ozone through ClO_x cycle, but through the formation of the ClO dimer, ClOOCl [60]. Müller et al. [61] explained the involvement of HOCl in destroying the ozone layer during Antarctic spring. During this time, the reaction of Cl with CH₄ forms HCl, and if not counteracted, it would end ozone destruction in a few days. HOCl is formed by reaction 25, followed by



in the presence of the PSCs. This reaction converts the HCl formed into active Cl₂, which maintains the destruction of ozone in the Antarctic spring for several months.

As part of monitoring the Montreal Protocol and the Antarctic ozone hole, a comprehensive understanding of HOCl is very important. This analysis of HOCl was performed using ACE-FTS version 5.0, which provides the VMR altitude profile.

HOCl data from ACE spanning February 2004 to August 2020 were retrieved and organized into 5° latitude bins at each altitude ranging from 14.5 km to 39.5 km. VMR values below -300 ppt and above 1500 ppt were filtered out to eliminate unphysical values. The averaged VMR values for the entire period are depicted in Figure 17. The highest HOCl VMR peak, approximately 160 ppt, occurred near 40 km in the mid-latitude region (around 40°S and 40°N). MIPAS, the Michelson Interferometer for Passive Atmospheric Sounding on ENVISAT, reported peak values below 200 ppt at an altitude of about 35-37 km near 30°N during the day and 35°S during night [62]. SMILES, the Superconducting Submillimeter-Wave Limb-Emission Sounder on the International Space Station, recorded HOCl peaks of 150-180 ppt just above 40 km at night and just below 40 km during the day [63]. The observed feature at 80°S and 30–35 km is associated with the descent in the Antarctic polar vortex, while the feature at the same latitude, around 18–23 km, is attributed to HOCl production on PSCs.

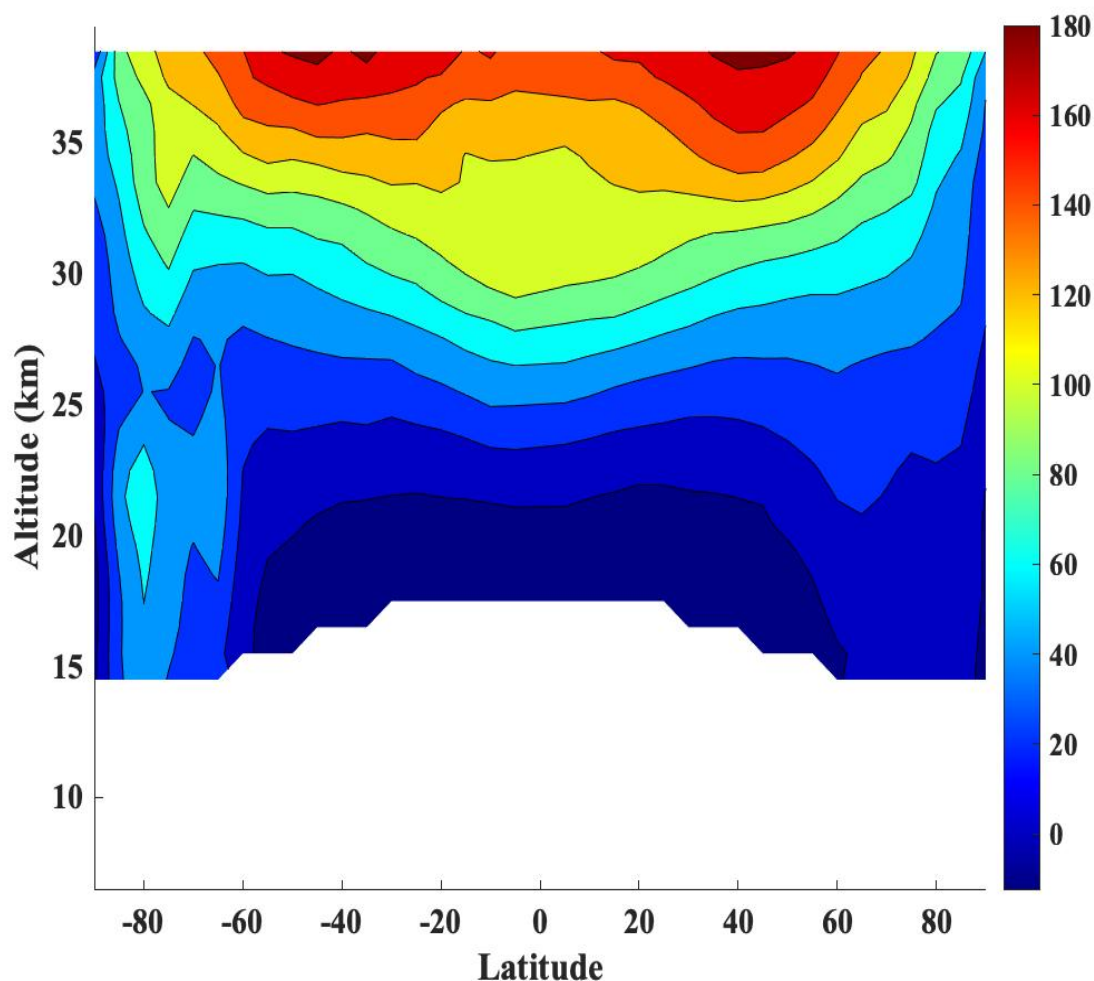


Figure 17. HOCl altitude-latitude VMR plot for the 2004-2020 mission average. The color scale is HOCl VMR in ppt. The figure is from Bernath et al. [51]

The VMR values were further categorized into four seasons: DJF (December, January, and February), MAM (March, April, and May), JJA (June, July, and August), and SON (September, October, and November). Seasonal average HOCl VMR values were plotted (Figure 18), mirroring the approach used for the global VMR plot. A descent of HOCl during DJF is evident in the Arctic vortex around 70°N, attributed to Arctic polar chemistry. Similar Antarctic features were observed during JJA and SON. Chlorine activation is more pronounced in the Antarctic than the Arctic, linked to the significantly heightened levels of HOCl in the Antarctic ozone hole. Manney et al. [64] reported a record-low Arctic stratospheric ozone in spring 2020. ACE observations recorded

a peak HOCl VMR of 1.25 ± 0.06 ppb at 20.5 km on February 11, 2020, at 68°N , 70.6°E .

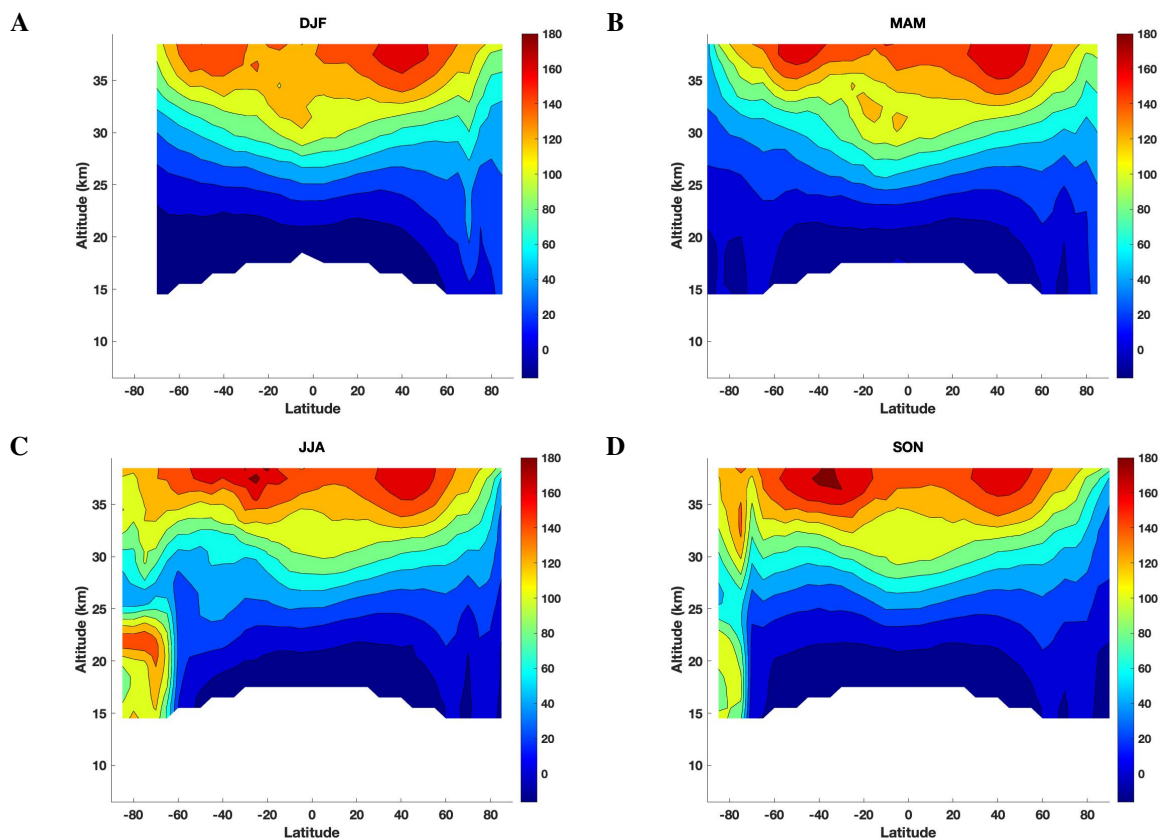


Figure 18. Seasonal distribution of HOCl VMR. VMR values are in ppt. The figure is from Bernath et al. [51]. (A) The figure shows the distribution in the months of December, January, and February. (B) The figure shows the distribution in the months of March, April, and May. (C) The figure shows the distribution in the months of June, July, and August. (D) The figure shows the distribution in the months of September, October, and November.

The ACE data proves invaluable for trend analysis, spanning from 2004 onward. The chosen region for quarterly time series analysis encompasses 60°S to 60°N , from 30.5 km to 39.5 km, as HOCl VMR peaks in the upper stratosphere. Quarterly averaged VMR values were computed from MAM 2004 to JJA 2020, and a linear trend was fitted. The resulting time series, depicted in Figure 19, indicates a decline in HOCl VMR by 0.23 ± 0.11 ppt/year, which is marginally significant. This evidence underscores the success of the Montreal Protocol in mitigating the chlorine burden in the

stratosphere. The observed change in stratospheric HOCl was approximately $-0.5\%/year$ [65], while HOCl exhibited a decrease of approximately $0.2\%/year$.

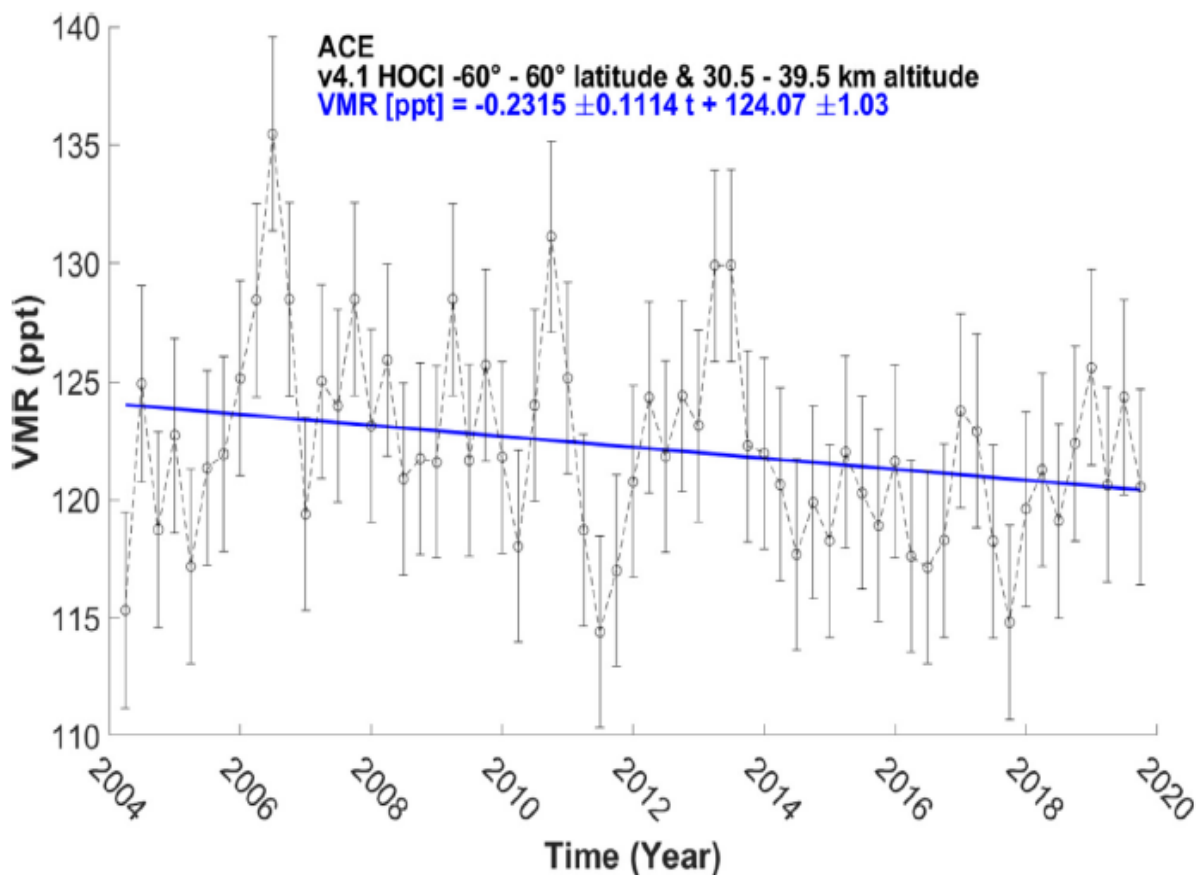


Figure 19. Time series of HOCl for the region 60°S to 60°N , 30.5 km to 39.5 km. The figure is from Bernath et al. [51].

HOCl is destroyed by rapid photolysis, as mentioned in Reaction 26, which suggests a variation in the HOCl VMR at sunrise and sunset. Figure 20 illustrates the mission average at sunrise and sunset, and Figure 21 shows the quarterly distributions at sunrise and sunset. Several differences observed in Figure 20 and 21 are from different spatial sampling distributions for sunrises and sunsets in the quarter. Sunrise and sunset occultations almost always sample different hemispheres [3].

MkIV, a mid-infrared solar absorption spectrometer, reported a HOCl concentration of 170 ppt at 37 km [66]. ACE observations revealed approximately 169 ppt at 37.5 km during the SON season for the 35°-40°N latitude bin. Notably, both values carried significant statistical errors. MIPAS (Michelson Interferometer for Passive Atmospheric Sounding) recorded an average VMR value of 180 ppt during the night at 37 km and 200 ppt during the day at 35 km, over the period 18-27 Sept. and 11-13 Oct. 2002 at 35°N [62]. MLS (Microwave Limb Sounder) measurements averaged from November 2009 to April 2010, within the range 20°S–20°N at 35 km, indicated a HOCl VMR of 153 ppt [67]. SMILES reported nighttime peak VMR values of about 150 ppt at 42 km and daytime values of approximately 160 ppt at 38 km from March to April 2010 in the range 20°S - 20°N [63]. ACE-FTS measurements, averaged from September to November 2004-2020, at altitudes between 35.5 km and 37.5 km, yielded HOCl VMR ranging from 158 ppt to 186 ppt.

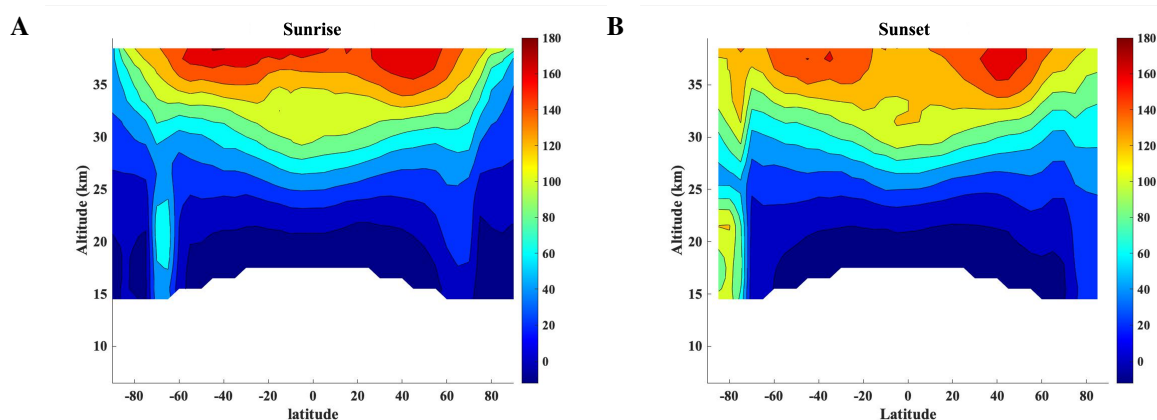


Figure 20. The mission average HOCl VMR distributions for (A) sunrise (B) sunset. VMR values are in ppt. The figure is from Bernath et al. [51].

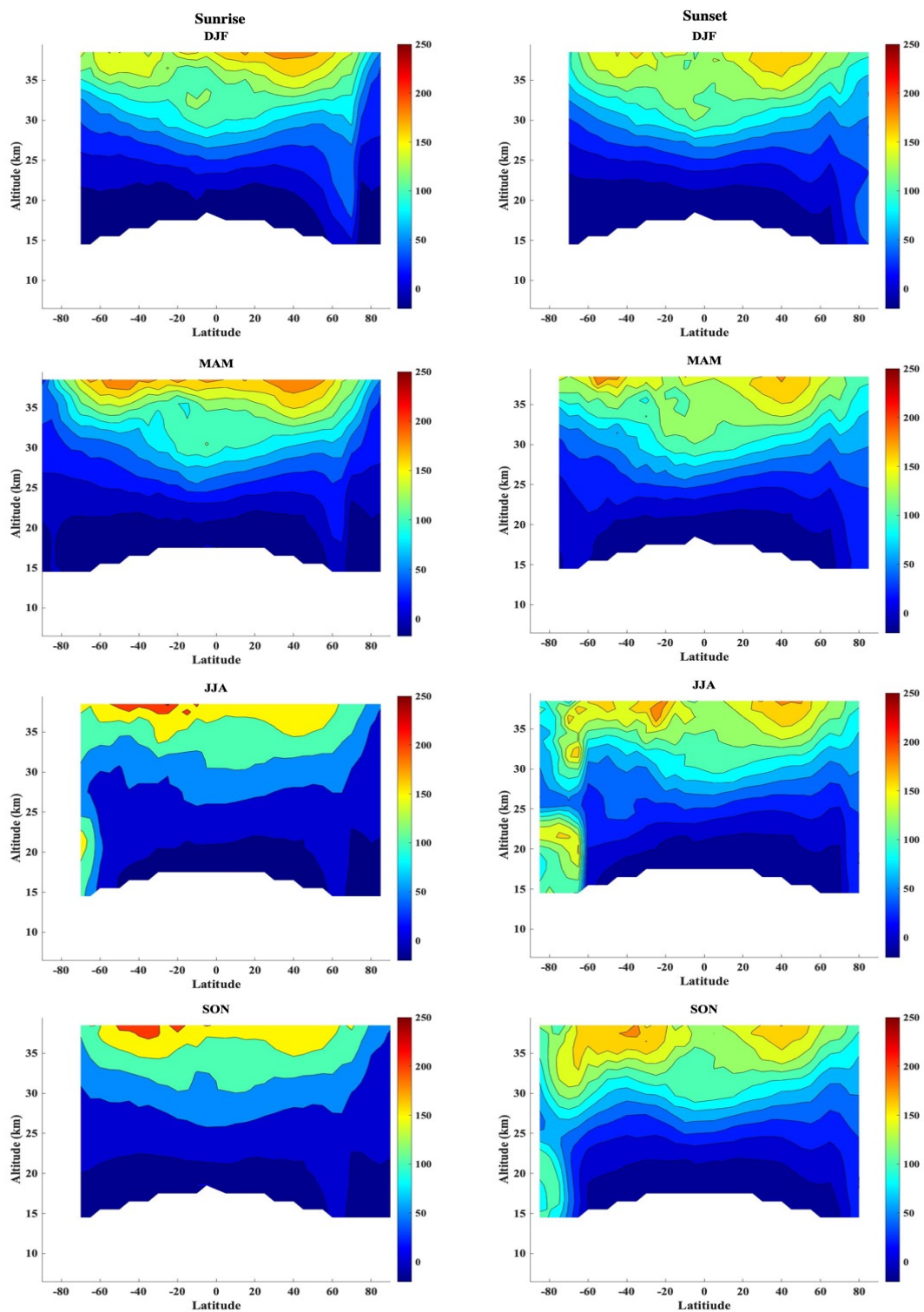


Figure 21. The mission average quarterly HOCl VMR distributions for sunrise (left) and sunset (right). The color scale is in ppt. The figure is from Bernath et al. [51].

3.4 HFC-32

HFCs are mainly used as refrigerants, in air conditioning systems, and as fire suppressants, thus accounting for their presence in the Earth's atmosphere. HFC-32 (CH_2F_2 , difluoromethane) has an atmospheric lifetime of 5.2 years [58] (5.4 years [57]), stratospheric lifetime of 124 years [58], a GWP of 809 (100-year) [58] (705 (100-year) [57]) and a radiative efficiency of $0.11 \text{ Wm}^{-2} \text{ ppb}^{-1}$ [57, 58]. The primary sinks for HFCs include their reaction with hydroxyl radicals (OH) in both the troposphere and stratosphere and their reaction with $\text{O}(^1\text{D})$ specifically in the stratosphere.

CFCs, HCFCs, and HFCs are global concerns, and their atmospheric abundances are assessed using various instruments. These measurements show that HFC-32 has increased rapidly in recent years. The Advanced Global Atmospheric Gases Experiment (AGAGE) stations reported a global abundance of 12.6 ppt in 2016 [68]. In 2004, the abundance of HFC-32 at Mace Head, Ireland, was 0.7 ppt, as reported by Greally et al. [69]. By December 2020, the concentration had risen to 28.7 ppt, as determined through NOAA flask measurements [52, 70].

The data on HFC-32 was obtained from ACE-FTS, and during that period, it was classified as a "research product." HFC-32 is currently part of ACE-FTS version 5.0 [71]. Microwindows were employed to facilitate the retrieval of HFC-32 and eliminate interference from numerous molecules [52, 54]. The data from Feb. 2004 to July 2020 were used in this analysis [52]. VMR values falling below -24 ppt or exceeding 50 ppt were filtered out, considering the anticipated VMR values and retrieval errors. The median average deviation (MAD) was computed at each altitude, and VMR values outside the range of median ± 4 MADs were excluded to eliminate any unphysical data. The associated statistical error for each VMR in an individual profile is about 8 ppt. The HFC-32 VMR value decreases as altitude increases, but the uncertainty remains relatively constant, thus increasing the percentage error.

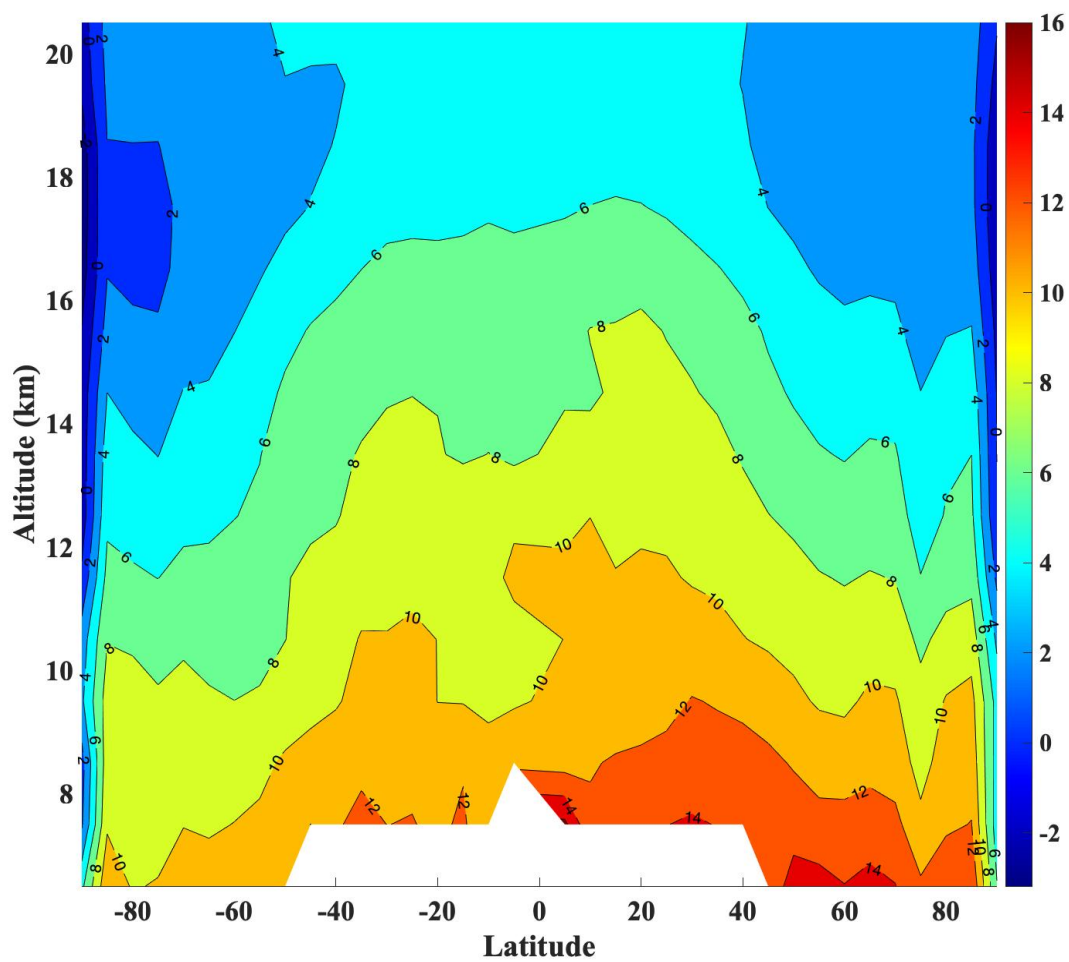


Figure 22. The average HFC-32 VMRs from Feb. 2004 to July 2020. The VMR values are given in ppt. The figure is from Dodangodage et al. [52].

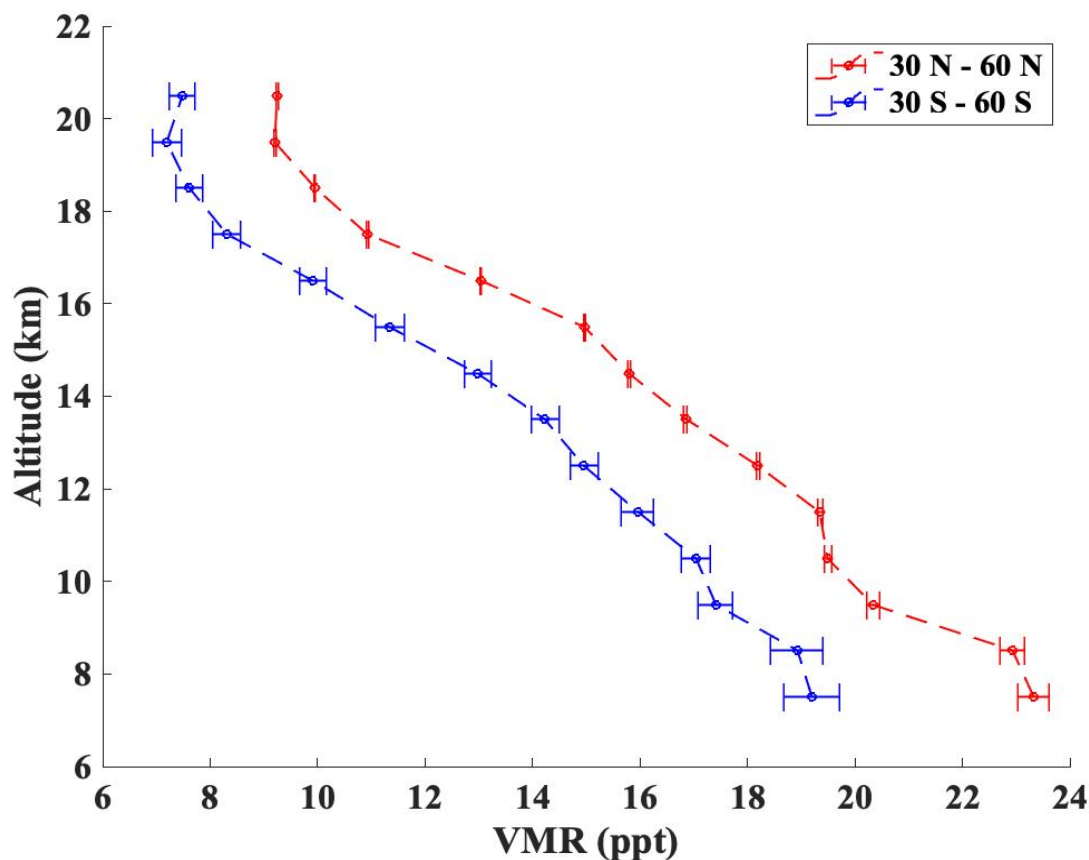


Figure 23. The average HFC-32 VMRs for the regions 30-60°N (red) and 30-60°S (blue) in the months of June, July, and August 2019. One standard deviation on the mean values are also shown. The figure is from Dodangodage et al. [52].

HFC-32 VMRs were sorted into bins of size 5° latitude and 1 km in altitude. The global mission average is shown in Figure 22. VMR values are enhanced in the northern hemisphere as expected since the major HFC emitters are located in the northern hemisphere. The mean VMR values for the areas 30-60°N and 30-60°S during June, July, and August 2019 are depicted against altitude in Figure 23. This illustrates a hemispherical asymmetry of approximately 3-4 ppt above 8 km, contrasting with a hemispherical discrepancy of around 6 ppt derived from National Oceanic and Atmospheric Administration (NOAA) surface data [52].

The HFC VMR values were categorized into four seasons: DJF (December, January, February), MAM (March, April, May), JJA (June, July, August), and SON (September, October, November). The mean VMR for each quarter from February 2004 to July 2020 was graphed, and all plots

Table 6. NOAA flask stations used.

Station Name	latitude	Height above sea level (m)	Data period start
Mauna Loa, USA	19.5°N	3397	2009
Cape Kumukahi, USA	19.5°N	3	2009
Niwot Ridge, USA	40.1°N	3475	2014
Trinidad Head, USA	41.0°N	120	2009
Wisconsin, USA	45.6°N	868	2014
Harvard Forest, USA	42.5°N	340	2014
Mace Head, Ireland	53.3°N	42	2014

closely resembled the global average distribution shown in Figure 22, except for a distinct localized stratospheric decrease in the SON quarter attributed to the descent in the Antarctic polar vortex.

The time series of HFC-32 VMR was established by averaging VMR values in the latitude region of 30-60°N and altitude from 7.5 km to 9.5 km for each quarter in each year from 2004 to 2020. The National Oceanic and Atmospheric Administration (NOAA) operates stations globally to measure atmospheric constituents. For comparison, seven stations from the northern hemisphere (Table 6) were chosen to obtain HFC-32 flask data.

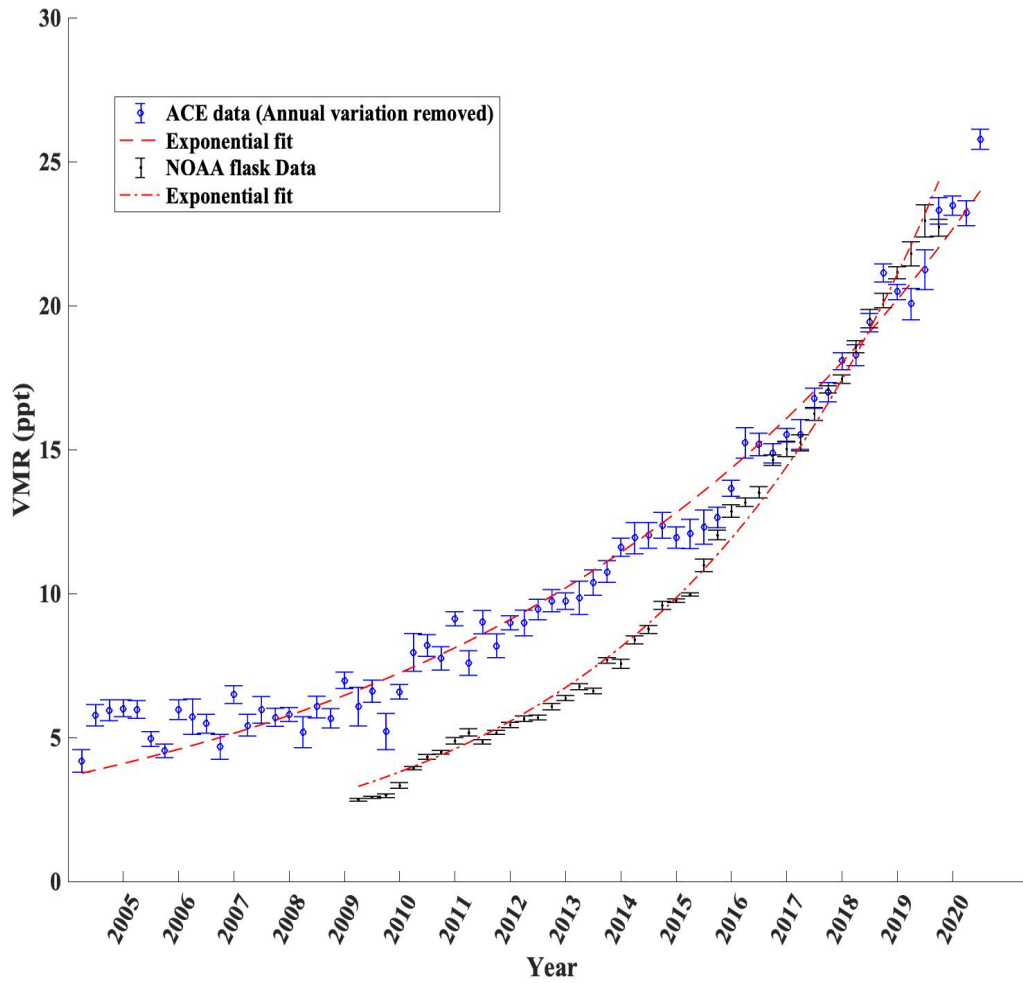


Figure 24. HFC-32 VMR time series. ACE data are shown in blue, and NOAA flask data are shown in black. The red curve is the exponential fit. Each averaged value is for the respective quarter in each year. ACE data are selected from the region 30-60°N, and altitude from 7.5 km to 9.5 km. The figure is from Dodangodage et al. [52].

Both flask data and ACE data show an exponential growth of HFC-32, as depicted in Figure 24. ACE data showed a small annual cycle that peaks in the summer and was removed. An exponential fit was used for both data. The ACE data is fitted to the equation,

$$VMR(t) = 3.65 \pm 0.23e^{0.114 \pm 0.0024t} \quad (30)$$

where t is year-2004, and NOAA flask data was fitted with

$$VMR(t) = 3.15 \pm 0.52e^{0.1903 \pm 0.0056t} \quad (31)$$

with $t = \text{year}-2009$. The derivatives of Equations (30) and (31) give the annual trend values in ppt/year. ACE values are biased high compared to NOAA values in the early part of the series, likely related to an interferer missing in the spectrum. This will also explain the slope in the tropospheric VMR in Figure 23. The ACE retrieval trends towards a constant value of 5 ppt for early times rather than trending towards 0. ACE data agrees better with NOAA data at later times, but a bias may still be present in the retrieval.

CHAPTER 4

SPECTROSCOPY OF DIATOMIC MOLECULES

Scientists have been interested in how elements are formed in the universe for a long time. Recent studies show that neutron star mergers play a significant role in the synthesis of heavy elements [72]. Heavy elements like La are formed in both the rapid neutron capture process (*r*-process) in kilonovae from neutron star mergers and in the slow neutron capture process (*s*-process) of asymptotic giant branch (AGB) stars [73]. The *s*-process is responsible for the formation of heavy elements like Y, Zr, Ba, and La from lighter elements by the repeated absorption of a neutron followed by a β -decay. Half of the elements heavier than Fe are thought to be synthesized through the *s*-process [74]. Measuring the abundances of these heavy elements will give insight into this *s*-process. S-stars which have a carbon-to-oxygen ratio of one, show spectral features associated with *s*-process elements. Line lists for the oxides of these *s*-process elements are required to determine the abundances of the molecules.

This chapter is based on rotational analysis of LaO $B^2\Sigma^+-X^2\Sigma^+$ [75], $A^2\Pi-X^2\Sigma^+$ [76], and $C^2\Pi-X^2\Sigma^+$ transitions and YO $B^2\Sigma^+-X^2\Sigma^+$ transition. The molecules LaO and YO have been observed in S-type stars, and these transitions have been previously analyzed by many others [77–89]. The present study involves a reevaluation of these spectral bands to derive more precise spectroscopic constants, resulting in a line list that is better suited for simulating stellar spectra.

4.1 SPECTROSCOPIC CONCEPTS

Solving the appropriate time-independent Schrödinger equation, we apply $\hat{H}\psi = E\psi$ to spectroscopic problems. The selection of an appropriate Hamiltonian operator and a basis set leads to obtaining the wavefunctions and energy levels and handling the general spectroscopic problem.

4.1.1 Born-Oppenheimer Approximation

The Schrödinger equation for diatomic molecules can be solved with the Born-Oppenheimer approximation, which allows the separation of the electronic motion from the nuclear motion. The nonrelativistic Hamiltonian operator for a molecule is given by,

$$\hat{H} = \hat{T}_N + \hat{T}_e + \hat{V}_{NN} + \hat{V}_{eN} + \hat{V}_{ee}, \quad (32)$$

in which $\hat{H}_{el} = \hat{T}_e + \hat{V}_{eN} + \hat{V}_{ee}$ describes the electronic structure. The electronic kinetic energy is

described by

$$\hat{T}_e = -\frac{\hbar^2}{2m_e} \sum_i \nabla_i^2, \quad (33)$$

the electron-nuclear attraction energy is given by

$$\hat{V}_{eN} = -\sum_{\alpha} \sum_i \frac{Z_{\alpha} e^2}{4\pi\epsilon_0 r_{i\alpha}}, \quad (34)$$

and the electron-electron repulsion energy is

$$\hat{V}_{ee} = \sum_i \sum_{j>i} \frac{e^2}{4\pi\epsilon_0 r_{ij}}. \quad (35)$$

The nuclear kinetic energy is given by

$$\hat{T}_N = -\frac{\hbar^2}{2} \sum_{\alpha} \frac{\nabla_{\alpha}^2}{M_{\alpha}}, \quad (36)$$

and the nuclear-nuclear repulsion energy is described by

$$\hat{V}_{NN} = \sum_{\alpha} \sum_{\beta>\alpha} \frac{Z_{\alpha} Z_{\beta} e^2}{4\pi\epsilon_0 r_{\alpha\beta}}. \quad (37)$$

The mass of an electron is given by m_e , Z_{α} and Z_{β} are the nuclear charges, e is the charge of the electron, and M_{α} is the nuclear masses. The Coulomb forces acting on the nuclei and electrons are similar in magnitude. Compared to nuclei, the electrons are lighter in mass and have much higher velocities. Thus, the electronic structure can be solved by fixing the nuclei at one position and separating the electronic motion from the nuclear motion. Since the nuclei are fixed in space, V_{NN} becomes a constant and can be added at the end to form the total electronic energy. The separation of the Schrödinger equation into electronic and nuclear motion, also known as vibration and rotation, allows the approximation of the wavefunction ψ to be the product of electronic and nuclear functions.

4.1.2 Rotational Spectroscopy

The molecule is considered to be a rotating rigid body. Using classical mechanics in the principal axis system, we can write the kinetic energy expression as

$$E_k = \frac{1}{2} I_x \omega_x^2 + \frac{1}{2} I_y \omega_y^2 + \frac{1}{2} I_z \omega_z^2, \quad (38)$$

where, I_x , I_y , and I_z gives the moment of inertia and ω_x , ω_y , and ω_z give the angular velocity around the x , y , and z axes, respectively. The x , y , and z axes are chosen in a way such that the highest-order axis of rotational symmetry is selected to be the z -axis. In rotational spectroscopy, another

labeling scheme is used based on the magnitude of moments of inertia. The a , b , and c axes are chosen to ensure the inequality $I_A \leq I_B \leq I_C$ is true [1]. For a linear diatomic molecule, $I_B = I_C$ and $I_A = 0$ or $I_x = I_y = I$ and $I_z = 0$. Then the kinetic energy can be written as

$$E_k = \frac{1}{2}I_x\omega_x^2 + \frac{1}{2}I_y\omega_y^2 = \frac{J_x^2}{2I} + \frac{J_y^2}{2I}$$

$$E_k = \frac{J^2}{2I}, \quad (39)$$

where J is the total angular momentum excluding the nuclear spin. Then, the rotational Hamiltonian operator becomes

$$\hat{H} = \frac{\hat{J}^2}{2I}. \quad (40)$$

Applying the rotational Hamiltonian operator to Schrödinger equation,

$$\frac{\hat{J}^2}{2I}\psi = E\psi, \quad (41)$$

resulting in

$$\frac{\hat{J}^2}{2I}\psi = \frac{J(J+1)\hbar^2}{2I}\psi. \quad (42)$$

The energy eigenvalue is defined as $F(J) = BJ(J+1)$ in which

$$B = \frac{\hbar^2}{2I}, \quad (43)$$

with B defined as the rotational spectroscopic constant. The intensity of the rotational transition depends on the transition dipole moment of the molecule. There will be no allowed transitions if the permanent dipole moment of the molecule is zero, otherwise, $\Delta J = \pm 1$ transitions may occur and are known as $R(\Delta J = +1)$ branches [1]. If there is additional angular momentum present, then $\Delta J = 0$ or Q branch rotational transitions are possible [1]. The frequencies of a transition involving $\Delta J = \pm 1$ is

$$\nu_{J+1 \leftarrow J} = F(J') - F(J'') = 2B(J+1). \quad (44)$$

J' denotes the upper state total angular momentum, and J'' is for the lower state total angular momentum. The first transition is $J = 1 \leftarrow 0$ and occurs at $2B$, while others are spaced by multiples of $2B$. So far, the molecule is assumed to be a rigid rotor, but as the molecule rotates, the atoms experience a centrifugal force, thus changing the internuclear distance. Therefore centrifugal distortion constants are added to the rotational energy expression ($F(J)$).

$$F(J) = BJ(J+1) - D[J(J+1)]^2 + H[J(J+1)]^3 + L[J(J+1)]^4 + \dots, \quad (45)$$

The rotational constants also depend on the vibrational state, meaning each vibrational state has its own rotational constants and centrifugal distortion constants. This dependence can be expressed as a power series of the vibrational state (v):

$$B_v = B_e - \alpha_e(v + \frac{1}{2}) + \gamma_e(v + \frac{1}{2})^2 + \dots, \quad (46)$$

$$D_v = D_e + \beta_e(v + \frac{1}{2}) + \dots, \quad (47)$$

4.1.3 Vibrational Spectroscopy

When considering a diatomic molecule, the motion of the two nuclei can be expressed using the reduced mass $\mu = \frac{m_A m_B}{m_A + m_B}$. Then, the Hamiltonian for the two-particle system can be expressed in terms of reduced mass and the momentum (P) of the system [1],

$$H = \frac{P^2}{2\mu} + V(r). \quad (48)$$

The potential energy ($V(r)$) of the system depends on the distance (r) between the two atoms. Then the quantum mechanical Schrödinger equation

$$\frac{-\hbar^2}{2\mu} \nabla^2 \psi + V(r) \psi = E \psi, \quad (49)$$

has energy eigenvalues

$$E_v = \hbar\omega(v + \frac{1}{2}). \quad (50)$$

While the provided solution serves as a general representation under the assumption of a harmonic oscillator potential, it's essential to note that due to the non-rigid nature of the rotating molecule, efforts have been made to formulate empirical expressions for the potential ($V(r)$). Using the Morse potential,

$$V(r) = D(1 - e^{-\beta(r-r_e)})^2, \quad (51)$$

is popular as it is convenient and asymptotically approaches a dissociation limit $V(r) = D$ as $r \rightarrow \infty$, and the Schrödinger equation can be solved analytically [1]. The energy eigenvalues can be written as

$$E = \omega_e \left(v + \frac{1}{2} \right) - \omega_e x_e \left(v + \frac{1}{2} \right)^2 + B_e J(J+1) - D_e [J(J+1)]^2 - \alpha_e \left(v + \frac{1}{2} \right) J(J+1). \quad (52)$$

The above equation can be rewritten using the Equations (45), (46) and (47),

$$E = \omega_e \left(v + \frac{1}{2} \right) - \omega_e x_e \left(v + \frac{1}{2} \right)^2 + F(J). \quad (53)$$

This energy equation consists of two additional terms to the previous rotational energy equation ($F(J)$), and is identified as the vibrational energy ($G(v)$),

$$G(v) = \omega_e \left(v + \frac{1}{2} \right) - \omega_e x_e \left(v + \frac{1}{2} \right)^2. \quad (54)$$

Note that this only has two terms, unlike the $F(J)$, which was a power series expansion. A more general form can be obtained using a Dunham potential, which is the Taylor expansion of $\xi = \frac{r-r_e}{r_e}$.

$$V(\xi) = a_0 \xi^2 (1 + a_1 \xi + a_2 \xi^2 + \dots), \quad (55)$$

where $a_0 = \frac{\omega_e^2}{4B_e}$. Approximate analytical solutions can be obtained for a Dunham potential, and the energy levels are given by

$$E_{vJ} = \sum_{ik} Y_{ik} \left(v + \frac{1}{2} \right)^i [J(J+1)]^k. \quad (56)$$

These Dunham parameters (Y_{ik}) are a match to the spectroscopic constants [1], and the energy level expressions can be written as

$$F_v(J) = B_v J(J+1) - D_v [J(J+1)]^2 + H [J(J+1)]^3 + \dots, \quad (57)$$

$$G(v) = \omega_e \left(v + \frac{1}{2} \right) - \omega_e x_e \left(v + \frac{1}{2} \right)^2 + \omega_e y_e \left(v + \frac{1}{2} \right)^3 + \omega_e z_e \left(v + \frac{1}{2} \right)^4 + \dots \quad (58)$$

4.1.4 Electronic Structure of a Diatomic Molecule

The electronic states of a molecule can be described using molecular orbital theory, where the wavefunction of the molecule is treated as a linear combination of atomic orbitals. The electronic structure of diatomic molecules is derived from considering the shapes of molecular orbitals constructed as linear combinations of atomic orbitals. Molecular orbitals are also filled with electrons following the Pauli principle. Each atomic orbital has an orbital angular momentum (λ), and the resultant orbital angular momentum about the internuclear axis is denoted Λ . The value of Λ is used to label the electronic state of a molecule; the electronic state is a Σ state if $\Lambda = 0$, the electronic state is a Π state if $\Lambda = \pm 1$, and so on. The two Σ states arising from the vector addition of λ are not degenerate and are split into two Σ^+ and Σ^- states. The total electronic spin (S) of the molecular state is obtained by summing the individual spins. Thus, the notation for the electronic state of a diatomic molecule is $^{2S+1}\Lambda_\Omega$, and Ω is sometimes used to denote a particular spin component. The ground electronic state is given a label X , and the successive excited states of the same spin multiplicity are labeled A , B , C , and so on. The excited states with different spin multiplicity are labeled with a , b , c , and so on. The low-lying electronic states of LaO molecule is illustrated in Figure 25.

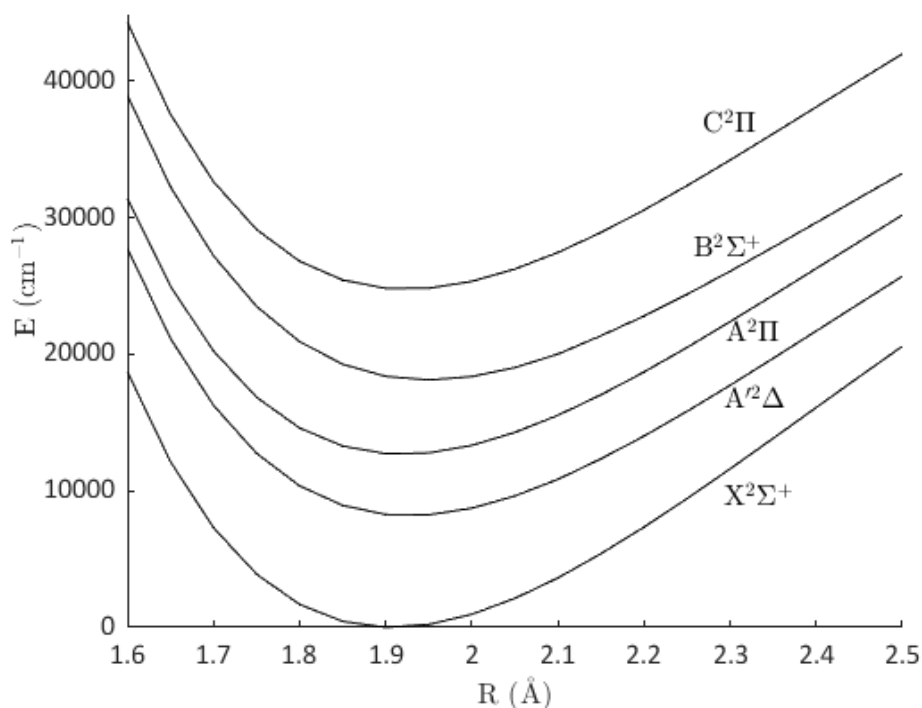


Figure 25. The low-lying electronic states of LaO molecule.

4.2 INTRODUCTION TO PGOPHER

PGOPHER [90] is a program developed by Colin Western for simulating and fitting molecular spectra. It has been developed as an open-source application that can simulate and fit rotational, vibrational, and electronic molecular spectra. The program is based on expanding the wavefunction for a given rovibrational level (Ψ_i) as a linear combination of basis states, $|j\rangle$:

$$\Psi_i = \sum_j c_{ij} |j\rangle. \quad (59)$$

The Hamiltonian matrix is diagonalized in the basis to calculate the energy levels and the coefficients c_{ij} , and the Hamiltonian and the basis set depend on the molecular system, and it will include vibrational and electronic state, total electron spin, symmetry, total angular momentum, and nuclear spin. PGOPHER can be set up to use specific Hamiltonian forms, including rotation, spin-rotation, spin-orbit coupling, hyperfine structure, Λ -doubling, etc. The relevant sections of the diatomic molecules provide discussions on the specific Hamiltonians employed. Utilizing an

experimentally recorded spectrum as an overlay, the graphical user interface enables the assignment of transition lines and calculates the relevant spectroscopic parameters.

4.3 LaO TRANSITIONS

LaO has five low-lying electronic states: $X^2\Sigma^+$, $A'^2\Delta$, $A^2\Pi$, $B^2\Sigma^+$, and $C^2\Pi$ (Figure 25). LaO transitions have been studied over many years, starting with the vibrational analysis of many electronic transitions by Jevons [91]. Weltner Jr et al. [92] correctly identified the ground state of LaO to be a $^2\Sigma^+$ state with a large magnetic hyperfine structure. ^{139}La has a nuclear spin (I) of 7/2 and a magnetic moment (μ_B) of 2.78 Bohr magnetons [83]. Bernard and Sibäi [77] collected all the data available at the time to reanalyze the bands and provided a set of spectroscopic constants for the $X^2\Sigma^+$, $A'^2\Delta$, $A^2\Pi$, $B^2\Sigma^+$, and $C^2\Pi$ states. Steimle and Virgo [83] determined the dipole moments for the $A^2\Pi$ and $B^2\Sigma^+$ states as well as the hyperfine parameters for the $A^2\Pi$ state. Childs et al. [81], Törring et al. [82], and Suenram et al. [84] contributed to characterizing the ground state ($X^2\Sigma^+$) of LaO. Childs et al. [81] conducted a highly precise study of the hyperfine structure in the $X^2\Sigma^+$ and $B^2\Sigma^+$ states using laser-radio frequency double resonance in a molecular beam.

4.3.1 Experimental Spectrum of LaO

The analysis involved overlaying an experimentally recorded spectrum in PGOPHER. The emission spectrum was recorded at the National Solar Observatory at Kitt Peak in Arizona, utilizing a carbon tube furnace (King furnace) with the McMath-Pierce 1 m Fourier transform spectrometer. The recorded spectrum is accessible in the National Solar Observatory digital library. The furnace was heated to a temperature of 2100°C, and the spectrometer was equipped with silicon diode detectors and a visible beam splitter, which covered the 350 - 1100 nm spectral range. Eight scans were recorded in about 1 h at a spectral resolution of 0.05 cm^{-1} .

An overview of the $\Delta v = 0$ sequence of the $B^2\Sigma^+-X^2\Sigma^+$ transition is given in Figure 26A. Figure 26B shows the $\Delta v = 0$ sequence of the $A^2\Pi-X^2\Sigma^+$ transition. The splitting in the $A^2\Pi$ state due to large spin-orbit coupling is visible in Figure 26B, and the separation of the two spin components is about 860 cm^{-1} . The $A^2\Pi_{1/2}-X^2\Sigma^+$ subband lies at lower wavenumbers (higher wavelengths) than the $A^2\Pi_{3/2}-X^2\Sigma^+$ subband.

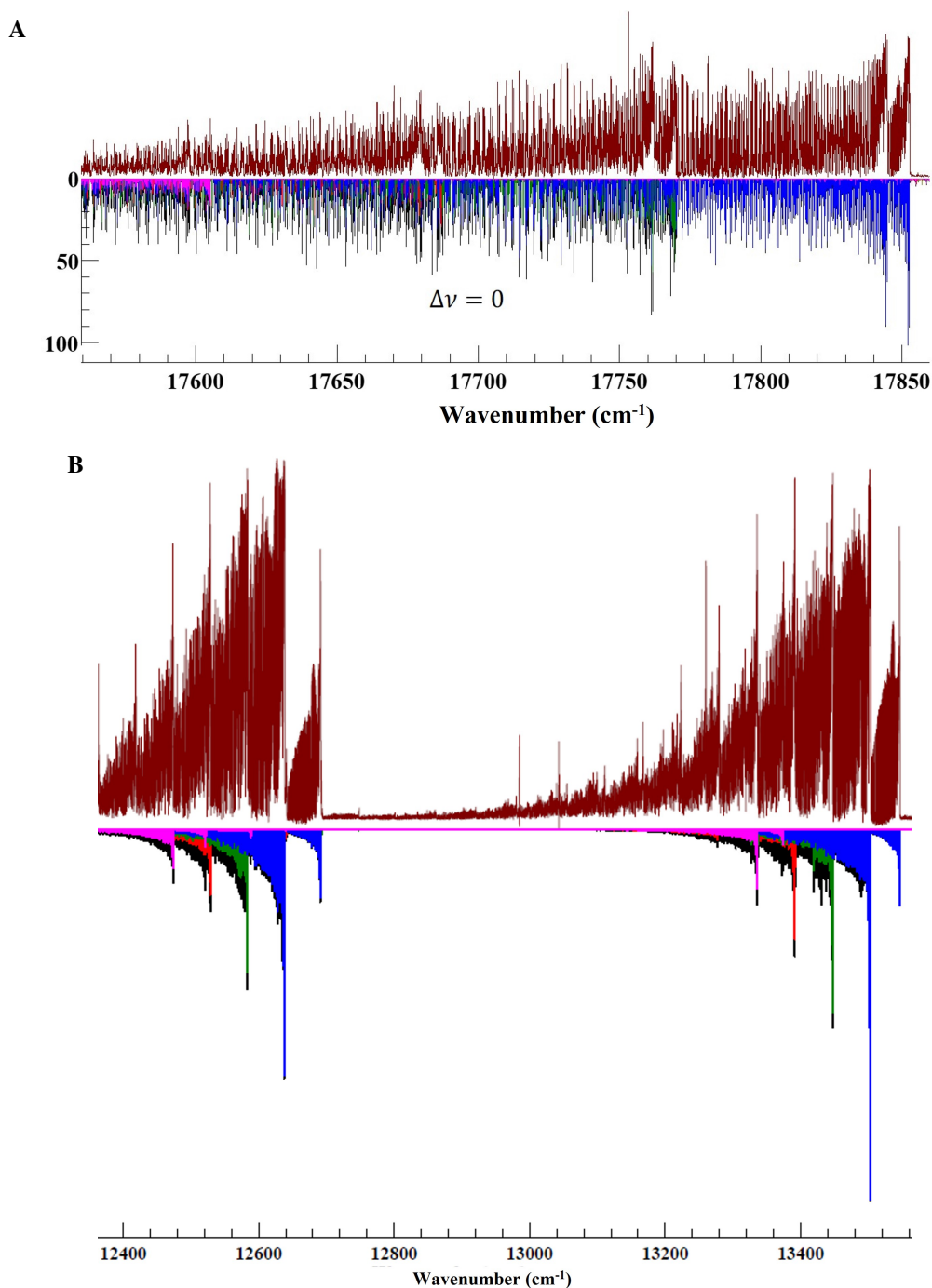


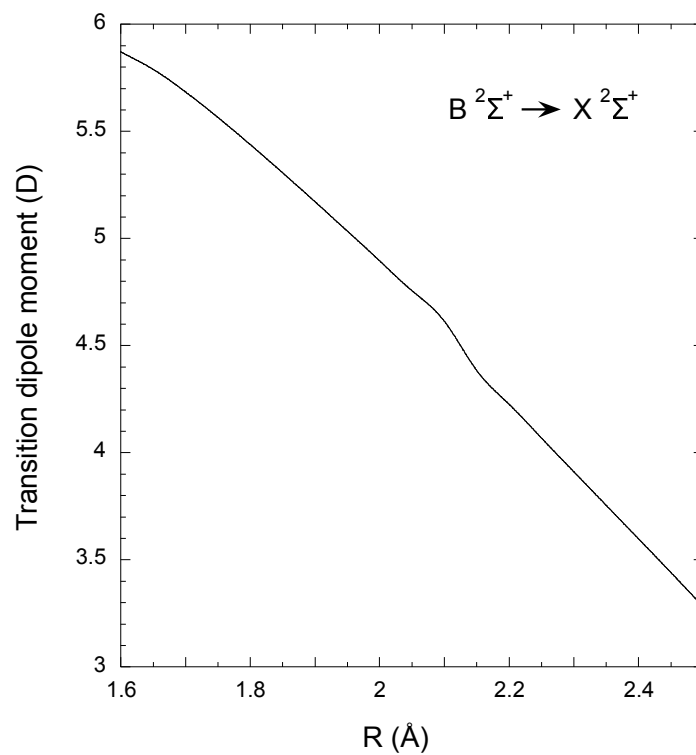
Figure 26. Overview emission spectrum of LaO $B^2\Sigma^+ - X^2\Sigma^+$ and $A^2\Pi - X^2\Sigma^+$ transitions. The experimentally recorded spectrum is shown in brown, and the simulated spectrum with various colors lies below it (Blue: 0-0 band, green: 1-1 band, red: 2-2 band, and pink: 3-3 band). (A) The $\Delta v = 0$ sequence of the $B^2\Sigma^+ - X^2\Sigma^+$ transition. The figure is from Bernath et al. [75]. (B) The $\Delta v = 0$ sequence of the $A^2\Pi - X^2\Sigma^+$ transition. $A^2\Pi_{1/2} - X^2\Sigma^+$ is on the left and $A^2\Pi_{3/2} - X^2\Sigma^+$ is on the right. The figure is from Bernath et al. [76].

4.3.2 Ab Initio Calculations

The electric transition dipole moment (TDM) curves have been calculated with the internally contracted configuration interaction method (ic-MRCI) [93, 94] using MOLPRO Quantum chemistry package [95, 96]. The ab initio calculations for the transition dipoles were done by J. Liévin from Université Libre de Bruxelles. A detailed description of the method, basis sets, and active space for $B^2\Sigma^+ - X^2\Sigma^+$ and $A^2\Pi - X^2\Sigma^+$ transitions are given in Bernath et al. [75] and Bernath et al. [76] respectively.

The TDM calculations were carried out at a set of internuclear distances (R), ranging from 1.6 to 2.5 Å, in steps of 0.05 Å and interpolated using B-splines to create a set of 1592 points. The TDM curves for each transition are given in Figure 27.

A



B

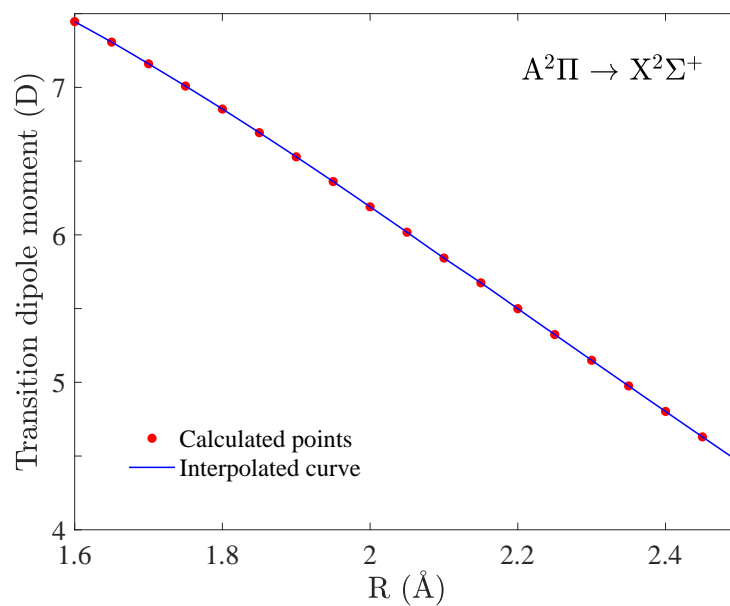


Figure 27. (A) Ab initio transition dipole moment curves for the $B^2\Sigma^+ - X^2\Sigma^+$ transition of LaO. The figure is from Bernath et al. [75]. (B) Ab initio transition dipole moment curves for the $A^2\Pi - X^2\Sigma^+$ transition of LaO. The figure is from Bernath et al. [76].

4.3.3 ${}^2\Sigma^+$ States of LaO

The rotational structure of a ${}^2\Sigma^+$ state can be described with the standard \mathbf{N}^2 Hamiltonian (H_{rot}),

$$H_{rot} = B\mathbf{N}^2 - D\mathbf{N}^4 + H\mathbf{N}^6, \quad (60)$$

where \mathbf{N} is the rotational angular momentum ($\mathbf{N} = \mathbf{J} - \mathbf{S}$), \mathbf{J} is the total angular momentum excluding nuclear spin, \mathbf{S} is the total electron spin, B is the rotational constant, and D and H are the centrifugal distortion constants. The interaction between electron spin and molecular rotation, known as spin-rotation interaction, is described by the Hamiltonian H_{sr} , where γ is the spin-rotation constant and γ_D is the centrifugal distortion correction:

$$H_{sr} = \gamma\mathbf{N} \cdot \mathbf{S} + \gamma_D\mathbf{N} \cdot \mathbf{S}(\mathbf{N}^2). \quad (61)$$

The interaction of nuclear spin (\mathbf{I}) with the total angular momentum (\mathbf{J}) creates a hyperfine structure ($\mathbf{F} = \mathbf{J} + \mathbf{I}$) to the nucleus of LaO. The hyperfine structure is described with Frosh and Foley constants [97], and the Hamiltonian (H_{hfs}) is written as [2, 81–83]

$$H_{hfs} = b\mathbf{I} \cdot \mathbf{S} + cI_z S_z + C_I \mathbf{I} \cdot \mathbf{N} + eqQ \frac{3I_z^2 - I(I+1)}{4I(2I-1)}, \quad (62)$$

in which b is the Fermi contact parameter, c is the dipole-dipole interaction constant, C_I is the nuclear spin-rotation interaction constant, and eqQ is the nuclear quadrupole coupling constant. The summation of these interactions describes the effective Hamiltonian (H_{eff}) for LaO ${}^2\Sigma^+$ states,

$$H_{eff} = H_{rot} + H_{sr} + H_{hfs}. \quad (63)$$

LaO possesses an unpaired electron, and in the excited $B^2\Sigma^+$ state, the spin \mathbf{S} of this unpaired electron couples with the rotational angular momentum \mathbf{N} ($\mathbf{J} = \mathbf{N} + \mathbf{S}$). The spin-rotation constant (γ) of the $B^2\Sigma^+$ state is negative, resulting in $J = N + 1/2$ (F_1) lying lower and $J = N - 1/2$ (F_2) lying higher. The resultant \mathbf{J} then couples with the nuclear spin \mathbf{I} ($I = 0$ for ${}^{16}\text{O}$ and $I = 7/2$ for ${}^{139}\text{La}$) to form up to eight $(2I + 1)$ hyperfine levels ($\mathbf{F} = \mathbf{J} + \mathbf{I}$), known as $b_{\beta J}$ coupling [2, 78]. Figure 28 illustrates the hyperfine splitting in the $B^2\Sigma^+$ state.

The ground state ($X^2\Sigma^+$) differs from the $B^2\Sigma^+$ state, with the Fermi contact parameter (b) being more significant than the spin-rotation interaction. This characteristic leads to the coupling of nuclear spin (\mathbf{I}) with electron spin (\mathbf{S}), resulting in the formation of an intermediate angular momentum $\mathbf{G} = \mathbf{I} + \mathbf{S}$. Consequently, all rotational levels undergo splitting into two components, $G = 4$ and $G = 3$. Each \mathbf{G} level couples with the rotational angular momentum \mathbf{N} to generate up to $2G + 1$ hyperfine levels, denoted as $\mathbf{F} = \mathbf{G} + \mathbf{N}$ and known as $b_{\beta s}$ coupling [2, 78]. The $G = 4$

resides at a higher energy level than $G = 3$, with a separation of about 0.52 cm^{-1} , leading to an unusual doubling of the spectral lines. See Figure 28 for the hyperfine splitting in the ground $X^2\Sigma^+$ state.

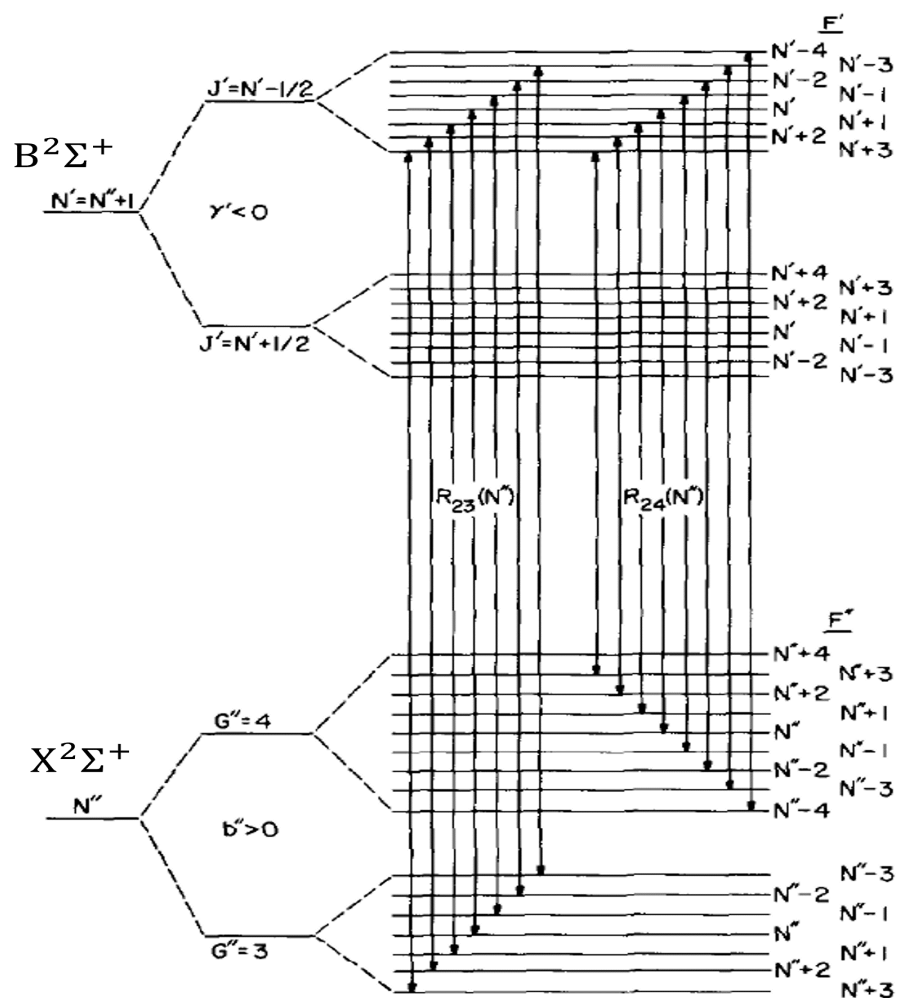


Figure 28. Hyperfine splitting of the LaO $B^2\Sigma^+$ and $X^2\Sigma^+$ states. The figure is from Childs et al. [81].

4.3.4 ${}^2\Pi$ States of LaO

The rotational structure for a ${}^2\Pi$ state can also be described using the standard \mathbf{N}^2 Hamiltonian (Equation (60)). The electron spin (\mathbf{S}) and orbital angular momentum (\mathbf{L}) couples to create spin-orbit interaction and is described with the Hamiltonian H_{so} [98]:

$$H_{so} = AL_zS_z + \frac{A_D}{2}[\mathbf{N}^2, L_zS_z]_+ + \frac{A_H}{2}[\mathbf{N}^4, L_zS_z]_+, \quad (64)$$

$$[O, Q]_+ = OQ + QO, \quad (65)$$

where A is the spin-orbit coupling constant, A_D and A_H are the centrifugal distortion constants of A . Λ -doubling can be seen in ${}^2\Pi$ states and is described with the p and q parameters [99]:

$$H_\Lambda = -\frac{1}{2}p(e^{-2i\phi}N_+S_+ + e^{2i\phi}N_-S_-) + \frac{1}{2}q(e^{-2i\phi}N_+^2 + e^{2i\phi}N_-^2). \quad (66)$$

The hyperfine structure of the ${}^2\Pi$ state is described by the Frosh and Foley parameters a , b , c and d [83]:

$$H_{hf} = aL_zS_z + b\mathbf{I} \cdot \mathbf{S} + c\left(I_zS_z - \frac{1}{3}\mathbf{I} \cdot \mathbf{S}\right) + \frac{d}{2}\left(e^{2i\phi}I_-S_- + e^{-2i\phi}I_+S_+\right). \quad (67)$$

The unpaired electron has a zero spin density at the La nucleus, and therefore, the Fermi contact parameter b for the $A^2\Pi$ state is constrained to zero [83]. The effective Hamiltonian for a ${}^2\Pi$ state can be written as

$$H_{eff} = H_{rot} + H_{so} + H_\Lambda + H_{hf}. \quad (68)$$

4.3.5 LaO $B^2\Sigma^+$ - $X^2\Sigma^+$ Transition

PGOPHER was used to analyze the spectrum. The spectroscopic constants described in Section 4.3.3 have a vibrational and rotational dependence, and it can be taken into account by expanding each spectroscopic constant ($X_{v,N}$) in a Dunham-type power series,

$$X_{v,N} = \sum_{i,j} X_{i,j} \left(v + \frac{1}{2}\right)^i [N(N+1)]^j. \quad (69)$$

Childs et al. [81] determined the vibrational dependence of the hyperfine constants and the spin-rotation constants for both $B^2\Sigma^+$ and $X^2\Sigma^+$ states. We incorporated their hyperfine structure (hfs) values for both the ground and excited states, as they are more precise compared to those that can be derived from the experimental spectrum we used (refer to Table 7 and 8). The spin-rotation constants (γ , γ_D , γ_H) of the $X^2\Sigma^+$ state were computed using the parameters provided by Childs et al. [81] in Equation (69), and these values were also held constant throughout the fitting process

(refer to Table 7). Rotational constants for $v = 0 - 2$ in the $X^2\Sigma^+$ state were obtained by Törring et al. [82] using microwave spectroscopy. Equations (46) and (47) were applied to calculate the rotational constants B_v and D_v in the $X^2\Sigma^+$ state, and these values were kept constant during the fitting procedure (Table 7).

The equilibrium constants reported by Bernard et al. [79] for the $B^2\Sigma^+$ and $X^2\Sigma^+$ states served as the basis for determining initial values for the origins and spectroscopic parameters of vibrational levels up to $v = 5$. The resultant fitted values for the $X^2\Sigma^+$ state origins are presented in Table 7, while Table 8 displays the final fitted values for the $B^2\Sigma^+$ state.

In the analysis with PGOPHER, 12120 lines were assigned in the 2-0, 3-1, 4-2, 5-3, 1-0, 2-1, 3-2, 4-3, 5-4, 0-0, 1-1, 2-2, 3-3, 4-4, 5-5, 0-1, 1-2, 2-3, 3-4, 4-5, 0-2, 1-3, 2-4, and 3-5 bands. Maximum J'' values were 120.5, 131.5, 120.5, 125.5, 93.5 and 89.5 for $v'' = 0, 1, 2, 3, 4$ and 5, respectively. Table 9 provides a sample of the assigned lines along with the calculated line positions and the residual value between observed and calculated line positions. The entire list is provided as a supplementary file to the Bernath et al. [75]. The labeling for the lines provided in Table 9 is $\Delta^N \Delta J_{(F'_i)F''_j}(J'')F', F''$, in which N is the quantum number for rotational angular momentum, J is the quantum number for total angular momentum exclusive of nuclear spin, and F'_i, F''_j and F ; subscripted $F_{i,j}$ are the customary labels for the two spin components of a $^2\Sigma^+$ states, 1 has $J = N + 1/2$ and 2 has $J = N - 1/2$ and the trailing F' and F'' values are the total angular momentum including nuclear spin. Customarily, primes are for the upper B state, and double primes are for the lower X state.

A set of equilibrium constants for both $B^2\Sigma^+$ and $X^2\Sigma^+$ states are calculated and are given in Table 10. These equilibrium constants were used as inputs to Le Roy's RKR program [100] to calculate the RKR (Rydberg-Klein-Rees) potential curves. The two RKR potential curves and the transition dipole moments calculated in Section 4.3.2 were used as inputs to Le Roy's LEVEL program [101] to calculate transition dipole matrix elements $\langle \psi_{e',v'} | \mu | \psi_{e'',v''} \rangle$ for $R(0)$ for all bands with v' and $v'' \leq 5$. The input files to the RKR and LEVEL programs are given in the appendix A. The calculated transition dipole matrix elements were used as the band strengths in PGOPHER and are listed in Table 11.

Table 7. Spectroscopic parameters for $X^2\Sigma^+$ state of LaO. The Table is from Bernath et al. [75].

	$v=0$	$v=1$	$v=2$	$v=3$	$v=4$	$v=5$
T_v	0 ^a	812.73754(70)	1621.19342(72)	2425.35172(82)	3225.18499(94)	4020.6780(12)
B_v	0.351807477 ^a	0.350377881 ^a	0.348942339 ^a	0.347500853 ^a	0.346053423 ^a	0.344600047 ^a
$10^7 D_v$	2.6246 ^a	2.6224 ^a	2.6201 ^a	2.61788 ^a	2.61561 ^a	2.6133 ^a
$10^3 \gamma_v$	2.2081 ^b	2.22181 ^b	2.23685 ^b	2.25321 ^b	2.2709 ^b	2.28992 ^b
$10^8 \gamma_{Dv}$	-1.45734 ^b	-1.43666 ^b	-1.41598 ^b	-1.3953 ^b	-1.3746 ^b	-1.3539 ^b
$10^{14} \gamma_{Hv}$	4.4364 ^b					
b	0.121147 ^b	0.121232 ^b	0.121317 ^b	0.121401 ^b	0.1214860 ^b	0.121571 ^b
$10^3 c$	3.1596 ^b	3.18 ^b	3.200 ^b	3.2208 ^b	3.2412 ^b	3.2617 ^b
$10^3 eqQ$	-2.8131 ^b	-2.807 ^b	-2.8017 ^b	-2.7961 ^b	-2.7904 ^b	-2.7847 ^b
$10^7 C_I$	4.818 ^b					
$10^8 b_D$	2.66851 ^b					
$10^9 c_D$	6.2543 ^b					
$10^8 eqQ_D$	-1.4777 ^b					

Notes. One standard deviation is given in parenthesis. All values are in cm^{-1} .

^a Held fixed during fitting. Values are from Dunham constants of Törring et al. [82].

^b Held fixed during fitting. Values are from Childs et al. [81].

Table 8. Spectroscopic parameters for $B^2\Sigma^+$ state of LaO. The Table is from Bernath et al. [75].

	$\nu = 0$	$\nu = 1$	$\nu = 2$	$\nu = 3$	$\nu = 4$	$\nu = 5$
T_ν	17837.3937(17)	18567.6509(13)	19293.8973(14)	20016.1283(14)	20734.2972(21)	21448.3950(39)
B_ν	0.34055994(56)	0.33902396(38)	0.33748655(53)	0.33594209(46)	0.3343991(11)	0.3328452(22)
$10^7 D_\nu$	2.93981(39)	2.93253(23)	2.92742(40)	2.92026(33)	2.9266(13)	2.9182(25)
γ_ν	-0.253556(35)	-0.253450(25)	-0.253252(30)	-0.253266(25)	-0.253778(31)	-0.253434(51)
$10^7 \gamma_{D\nu}$	-2.674(40)	-2.624(26)	-2.666(39)	-2.390(33)	-	-
$10^2 b$	1.94 ^a	1.905 ^a	1.871 ^a	1.837 ^a	1.802 ^a	1.768 ^a
$10^3 c$	6.409 ^a	5.939 ^a	5.469 ^a	4.998 ^a	4.528 ^a	4.058 ^a
$10^3 eqQ$	-6.56 ^a	-6.776 ^a	-6.993 ^a	-7.21 ^a	-7.43 ^a	-7.64 ^a

Notes. One standard deviation is given in parenthesis. All values are in cm^{-1}

^a Held fixed during fitting. Values are from Childs et al. [81].

Table 9. Sample of observed and calculated line list of the LaO $B^2\Sigma^+ - X^2\Sigma^+$ transition. The Table is from Bernath et al. [75].

F'	p'	F''	p''	Obs (cm^{-1})	Calc (cm^{-1})	Obs-Calc (cm^{-1})	Line assignment
55	f	54	f	17849.6052	17849.6233	-0.0181	rR2(50.5)55,54 : B v=0 51.5 52 F2f 55 - X v=0 50.5 51 F2f 54
47	e	46	e	17849.6052	17849.5800	0.0252	rR2(49.5)47,46 : B v=0 50.5 51 F2f 47 - X v=0 49.5 50 F2f 46
54	e	53	e	17849.6052	17849.6214	-0.0162	rR2(50.5)54,53 : B v=0 51.5 52 F2f 54 - X v=0 50.5 51 F2f 53
48	f	47	f	17849.6052	17849.5533	0.0519	rR2(49.5)48,47 : B v=0 50.5 51 F2f 48 - X v=0 49.5 50 F2f 47
53	f	52	f	17849.6052	17849.6187	-0.0135	rR2(50.5)53,52 : B v=0 51.5 52 F2f 53 - X v=0 50.5 51 F2f 52

Note: F' and F'' are the total angular momentum of the $B^2\Sigma^+$ and $X^2\Sigma^+$ states, respectively. p is the parity. Obs is the observed line position in cm^{-1} , Calc is the calculated line position in cm^{-1} , and Obs-Calc is the difference between the observed and calculated line position in cm^{-1} . Line assignment illustrate the transition ${}^{\Delta N} \Delta J_{(F'), F''} (J') F', F''$: B v $J' N' F 1 p / F 2 p F' - X v J'' N'' F 1 p / F 2 p F''$

Table 10. Equilibrium constants of LaO for $X^2\Sigma^+$ and $B^2\Sigma^+$ states. The Table is from Bernath et al. [75].

	$X^2\Sigma^+$	$B^2\Sigma^+$
ω_e	816.9969(25)	734.2344(78)
$\omega_e x_e$	2.1243(11)	1.9830(36)
$10^3 \omega_e y_e$	-3.48(13)	-4.09(45)
B_e	0.352520046 ^a	0.3413261(17)
$10^3 \alpha_e$	1.42365 ^a	1.5319(16)
$10^6 \gamma_e$	-2.9724 ^a	-1.77(32)

Notes. All values are in cm^{-1} . ^a Held fixed during fitting and the values are from Dunham constants of Törring et al. [82].

Table 11. Band strengths of $B^2\Sigma^+ - X^2\Sigma^+$ transition of LaO. The Table is from Bernath et al. [75].

	$v'' = 0$	$v'' = 1$	$v'' = 2$	$v'' = 3$	$v'' = 4$	$v'' = 5$
$v' = 0$	4.94309	1.78918	0.505466	0.116356	2.25885×10^{-2}	3.34618×10^{-3}
$v' = 1$	-2.00225	4.18192	2.33711	0.8376475	0.226165	4.75155×10^{-2}
$v' = 2$	0.545388	-2.64277	3.45503	2.62842	1.12914	0.341525
$v' = 3$	-0.106461	0.923692	-2.99886	2.76845	2.77356	1.38171
$v' = 4$	1.20215×10^{-2}	-0.218389	1.27280	-3.17634	2.13129	2.82974
$v' = 5$	1.1576×10^{-3}	3.13752×10^{-2}	-0.354142	1.59862	-3.20517	1.55462

Notes: These band strengths should be multiplied by a correction factor of 0.77. All values are in debye.

Transition moments ($\mu_{v' \rightarrow v''}$) given in Table 11 were used in,

$$A_{v' \rightarrow v''} = 3.136 \times 10^{-7} \nu^3 \mu_{v' \rightarrow v''}^2, \quad (70)$$

to calculate the Einstein $A_{v' \rightarrow v''}$ (s^{-1}) values [1], where ν is the band origin for the $B^2\Sigma^+ - X^2\Sigma^+$ $v' - v''$ transition in cm^{-1} . The Einstein A values were used to calculate the radiative lifetime:

$$\tau_{v'} = \frac{1}{\sum_{v''} A_{v' \rightarrow v''}}, \quad (71)$$

of the $B^2\Sigma^+$ state.

Dagdikian et al. [102] have measured radiative lifetimes of alkaline earth monohalides. Being isoelectronic to the alkaline earth monohalides, LaO is anticipated to have a radiative lifetime for the $B^2\Sigma^+$ state within the range of 20-40 ns [103]. The radiative lifetimes of the $B^2\Sigma^+$ state $\nu = 0$ were experimentally determined by Liu and Parson [103] to be 34.2 ± 1.5 and 35.5 ± 1.2 ns at two distinct wavelengths. Similarly, for the $B^2\Sigma^+$ state $\nu = 1$, the measured lifetimes were 36.0 ± 1.8 and 35.9 ± 2.4 ns. Carette and Bencheikh [104] determined the radiative lifetime of the $B^2\Sigma^+$ state $\nu = 0$ to be 32 ± 2 ns. The calculated radiative lifetimes were comparatively lower than the measured values. To address this difference, an average lifetime of 33.9 ns for $\nu = 0$ was determined, suggesting the application of a correction factor of 0.77 to the transition dipole matrix elements presented in Table 11. The radiative lifetimes after correcting are provided in Table 12. Calculating the properties of heavy elements is difficult, and therefore, this correction factor is not unreasonable and strictly applies to the 0-0 band. The application to the other bands is an assumption [75].

Table 12. Radiative lifetimes of LaO $B^2\Sigma^+$ state. The Table is from Bernath et al. [75].

$B^2\Sigma^+ \nu =$	0	1	2	3	4
τ_ν (ns)	33.90	34.42	34.94	35.63	38.97

A line list for the $B^2\Sigma^+ - X^2\Sigma^+$ transition of LaO was generated with PGOPHER for $J < 200$ and a sample is provided in Table 13. The complete list is provided as a supplementary file in Bernath et al. [75]. The predicted line positions become unreliable for the J values beyond the observed maximum value but they provide opacity for low-resolution astronomical applications [75].

Table 13. Sample line list of the LaO $B^2\Sigma^+-X^2\Sigma^+$ transition. The Table is from Bernath et al. [75].

F'	F''	Position (cm^{-1})	E_{up} (cm^{-1})	E_{low} (cm^{-1})	A (s^{-1})	Line assignment
199	200	13451.4782	30773.5841	17322.1059	2.168176	pP1(199.5)199,200 : B v=0 198.5 198 F1e 199 - X v=5 199.5 199 F1e 200
200	200	13451.4882	30773.5941	17322.1059	.0004978	pP1(199.5)200,200 : B v=0 198.5 198 F1e 200 - X v=5 199.5 199 F1e 200
198	199	13451.5029	30773.5744	17322.0715	2.013565	pP1(199.5)198,199 : B v=0 198.5 198 F1e 198 - X v=5 199.5 199 F1e 199
199	199	13451.5126	30773.5841	17322.0715	.0005141	pP1(199.5)199,199 : B v=0 198.5 198 F1e 199 - X v=5 199.5 199 F1e 199
197	198	13451.5323	30773.5649	17322.0326	1.831155	pP1(199.5)197,198 : B v=0 198.5 198 F1e 197 - X v=5 199.5 199 F1e 198
198	198	13451.5418	30773.5744	17322.0326	.0004662	pP1(199.5)198,198 : B v=0 198.5 198 F1e 198 - X v=5 199.5 199 F1e 198
196	197	13451.5689	30773.5558	17321.9869	1.598742	pP1(199.5)196,197 : B v=0 198.5 198 F1e 196 - X v=5 199.5 199 F1e 197
197	197	13451.5781	30773.5649	17321.9869	.0003621	pP1(199.5)197,197 : B v=0 198.5 198 F1e 197 - X v=5 199.5 199 F1e 197

Notes: F' and F'' are the total angular momentum of the $B^2\Sigma^+$ and $X^2\Sigma^+$ states, respectively. Position is the line position in cm^{-1} . E_{up} and E_{low} are the energies of the $B^2\Sigma^+$ and $X^2\Sigma^+$ states in cm^{-1} . Einstein A coefficients in s^{-1} are given under A. Line assignment illustrate the transition

$$\Delta^N \Delta J_{(F')F''}(J'')F' : B v J' N' F1p/F2p F' - X v J'' N'' F1p/F2p F''$$

Spectroscopic parameters and origins for various vibrational levels of the $B^2\Sigma^+$ and $X^2\Sigma^+$ states have been previously computed. Bernard and Sibai [77] reported the origin of $v = 0$ for the $B^2\Sigma^+$ state as $17837.345(30) \text{ cm}^{-1}$ and, for $v = 1$ of the $B^2\Sigma^+$ and $X^2\Sigma^+$ states, $18567.613(69) \text{ cm}^{-1}$ and $812.676(69) \text{ cm}^{-1}$, respectively. The calculated values (Tables 7 and 8) for the corresponding vibrational levels exhibit agreement within the margin of error. Equilibrium constants for the $X^2\Sigma^+$, as calculated by Bernard et al. [79], are $\omega_e = 817.0264(78) \text{ cm}^{-1}$, $\omega_e x_e = 2.1292(24) \text{ cm}^{-1}$, and $\omega_e y_e = -0.00315(24) \text{ cm}^{-1}$. Similarly, for the $B^2\Sigma^+$ state, the reported values are $\omega_e = 734.2811(87) \text{ cm}^{-1}$, $\omega_e x_e = 1.9922(29) \text{ cm}^{-1}$, and $\omega_e y_e = -0.00354(32) \text{ cm}^{-1}$. The calculated values for B_e and α_e for the $B^2\Sigma^+$ by Bernard et al. [79] are $0.34133169(95) \text{ cm}^{-1}$ and $0.00154227(34) \text{ cm}^{-1}$, respectively. Employing a three-parameter fit with six vibrational levels in both $B^2\Sigma^+$ and $X^2\Sigma^+$ states, we derived equilibrium constants (Table 10) that align with the reported values by Bernard et al. [79]. A limited number of lines in the 5-5 band could be confidently assigned, and slight deviations between the simulated spectrum and the observed spectrum in the higher J lines were observed. However, on the whole, the simulated spectrum exhibits a good overall agreement with the observed spectrum. Figure 29 shows a closer look at the 1-0 band head of the LaO $B^2\Sigma^+ - X^2\Sigma^+$ transition.

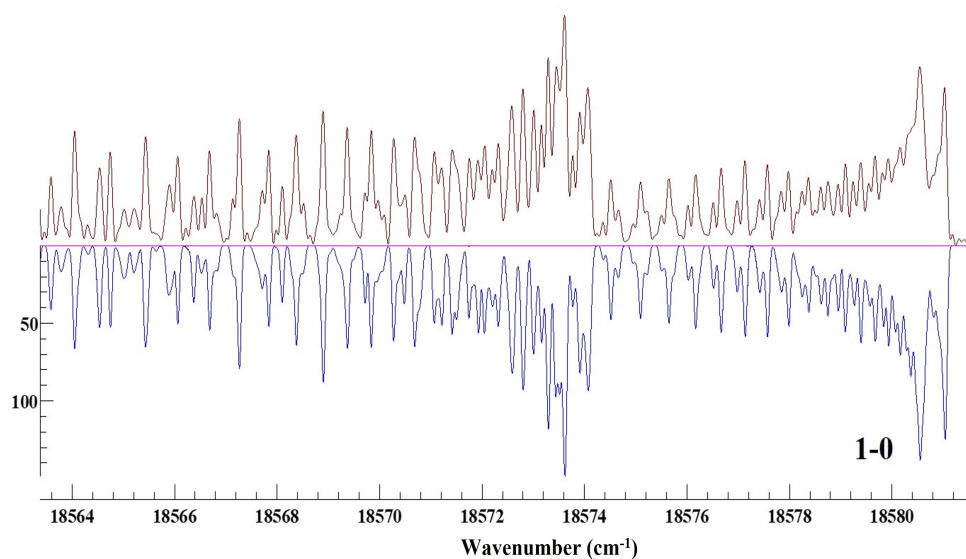


Figure 29. The spectrum of LaO (above) and simulation (below) of the $B^2\Sigma^+ - X^2\Sigma^+$ 1-0 band. The figure is from Bernath et al. [75].

4.3.6 LaO A²Π-X²Σ⁺ Transition

The A²Π-X²Σ⁺ transition of LaO was analyzed using PGOPHER, utilizing the experimental spectrum detailed in Section 4.3.1 as an overlay. Equilibrium constants from Bernard and Vergés [80] were employed to derive initial values for the origins, B , D , A , and p for vibrational levels ranging from $\nu = 0$ to $\nu = 3$ in the A²Π state. Parameters for the nuclear hyperfine structure in the A²Π state, as provided by Steimle and Virgo [83], were maintained as fixed constants during the fitting process. The spectroscopic parameters in Table 7 served as the ground state (X²Σ⁺) constants. For this analysis, 8068 lines were assigned in the 0-0, 1-1, 2-2, 3-3, 3-4, 2-3, 1-2, 0-1, 1-0, 2-1 and 3-2 bands. Maximum J'' values are 75.5, 90.5, 79.5, 40.5, 75.5, 78.5, 80.5, 82.5, 44.5, 85.5, and 72.5 for the 0-0, 1-1, 2-2, 3-3, 3-4, 2-3, 1-2, 0-1, 1-0, 2-1 and 3-2 bands, respectively. The final calculated spectroscopic parameters for the A²Π state are provided in Table 14.

Many spectroscopic parameters given in Table 14 are irregular functions of ν , particularly the constants for $\nu = 1$ that deviate from the expected pattern. Higher-order parameters, which are nonphysical, were included in the fit. The vibrational levels of the A²Π state are globally perturbed. The equilibrium vibrational frequency of 762 cm⁻¹ closely approximates the spin-orbit constant ($A \approx 862$ cm⁻¹), resulting in an internal perturbation within the A²Π state. For example, the $\nu = 0$ of ²Π_{3/2} perturbs with $\nu = 1$ of ²Π_{1/2}, $\nu = 1$ of ²Π_{3/2} with $\nu = 2$ of ²Π_{1/2} and so on. Bernard and Vergés [80] also noted this interaction in the LaO A²Π state. Efforts to incorporate this interaction into the fit were unsatisfactory, leading to the utilization of a substantial number of empirical constants to characterize the energy levels of the A²Π state.

The observed and calculated line positions for the A²Π-X²Σ⁺ transition of LaO are given in Table 15 and the entire list is provided as a supplementary file to Bernath et al. [76]. The lines are labeled as ${}^{\Delta N}\Delta J_{(F'_i)(F''_j)}(J'')F', F''$, in which N is the quantum number for total angular momentum without electron spin, subscripted $F_{i,j}$ are the customary labels for the two spin components of a ²Π and a ²Σ⁺ state, 1 has $J = N + 1/2$ and 2 has $J = N - 1/2$ (i.e. for the A state, 1 is ²Π_{1/2} and 2 is ²Π_{3/2}) and the trailing F' and F'' are the total angular momentum with nuclear spin.

Table 14. Spectroscopic constants for the $A^2\Pi$ state. The Table is from Bernath et al. [76].

	$\nu = 0$	$\nu = 0^a$	$\nu = 1$	$\nu = 1^a$	$\nu = 2$	$\nu = 3$
T_ν	13066.6492(11)	13066.951(11)	13824.2952(48)	13824.166(10)	14577.6096(18)	15326.4404(50)
B_ν	0.34633907(84)	0.346162(82)	0.3447145(55)	0.344564(63)	0.3431243(12)	0.3414104(39)
$10^7 D_\nu$	2.8714(15)	2.741(78)	3.2744(224)	2.891(80)	2.8755(20)	2.7838(67)
$10^{12} H_\nu$	-	-	6.230(313)	-	-	-
A_ν	862.4104(20)	862.434(22)	861.5701(96)	862.434	860.5999(36)	860.0181(60)
$10^4 A_{D\nu}$	1.9537(83)	3.095(97)	0.90(12)	3.1	2.422(26)	0.190(20)
$10^8 A_{H\nu}$	-	-0.77(12)	-6.643(450)	-	-0.276(41)	-
$10^{-12} A_{L\nu}$	-	-	9.698(630)	-	-	-
p_ν	-0.237942(95)	-0.26743(24)	-0.21823(38)	-0.267	-0.242335(80)	-0.22721(14)
$10^5 p_{D\nu}$	0.0631(30)	-	-1.3443(240)	-	-0.0163(19)	0.1421(47)
$10^9 p_{H\nu}$	-	-	1.131(30)	-	-	-
$10^2 q_\nu$	-0.0275(36)	-0.0096(100)	-1.030(12)	-0.0096	-	-
$10^7 q_{D\nu}$	0.298(49)	-	8.94(28)	-	-	-
$10^3 a$	7.74 ^b	-	7.74 ^b	-	7.74 ^b	7.74 ^b
$10^3 c$	-8.71 ^b	-	-8.71 ^b	-	-8.71 ^b	-8.71 ^b
$10^2 d$	1.37 ^b	-	1.37 ^b	-	1.37 ^b	1.37 ^b

Notes. One standard deviation is given in parentheses. All values are in cm^{-1} . ^a Values reported by Bernard and Sibai [77]. Note that a slightly different Hamiltonian was used. ^b Held fixed during fitting. Values are from Steimle and Virgo [83].

Table 15. Sample of observed and calculated line list of the LaO $A^2\Pi-X^2\Sigma^+$ transition. The Table is from Bernath et al. [76].

F'	p'	F''	p''	Obs (cm^{-1})	Calc (cm^{-1})	Obs-Calc (cm^{-1})	Line assignment
43	f	43	e	13502.8655	13502.8517	0.0138	rQ21(39.5)43,43 : A2Pi v=0 39.5 40 F2f 43 - X2Sigma+ v=0 39.5 39 F1e 43
42	e	42	f	13502.8655	13502.8607	0.0048	rQ21(39.5)42,42 : A2Pi v=0 39.5 40 F2f 42 - X2Sigma+ v=0 39.5 39 F1e 42
41	f	41	e	13502.8655	13502.8701	-0.0046	rQ21(39.5)41,41 : A2Pi v=0 39.5 40 F2f 41 - X2Sigma+ v=0 39.5 39 F1e 41
40	e	40	f	13502.8655	13502.88	-0.0145	rQ21(39.5)40,40 : A2Pi v=0 39.5 40 F2f 40 - X2Sigma+ v=0 39.5 39 F1e 40
44	f	44	e	13502.7856	13502.769	0.0166	rQ21(40.5)44,44 : A2Pi v=0 40.5 41 F2f 44 - X2Sigma+ v=0 40.5 40 F1e 44
43	e	43	f	13502.7856	13502.7783	0.0073	rQ21(40.5)43,43 : A2Pi v=0 40.5 41 F2f 43 - X2Sigma+ v=0 40.5 40 F1e 43
42	f	42	e	13502.7856	13502.7879	-0.0023	rQ21(40.5)42,42 : A2Pi v=0 40.5 41 F2f 42 - X2Sigma+ v=0 40.5 40 F1e 42
41	e	41	f	13502.7856	13502.798	-0.0124	rQ21(40.5)41,41 : A2Pi v=0 40.5 41 F2f 41 - X2Sigma+ v=0 40.5 40 F1e 41
40	f	40	e	13502.7856	13502.8085	-0.0229	rQ21(40.5)40,40 : A2Pi v=0 40.5 41 F2f 40 - X2Sigma+ v=0 40.5 40 F1e 40
45	f	45	e	13502.7091	13502.6753	0.0338	rQ21(41.5)45,45 : A2Pi v=0 41.5 42 F2f 45 - X2Sigma+ v=0 41.5 41 F1e 45
44	e	44	f	13502.7091	13502.6847	0.0244	rQ21(41.5)44,44 : A2Pi v=0 41.5 42 F2f 44 - X2Sigma+ v=0 41.5 41 F1e 44
43	f	43	e	13502.7091	13502.6946	0.0145	rQ21(41.5)43,43 : A2Pi v=0 41.5 42 F2f 43 - X2Sigma+ v=0 41.5 41 F1e 43
42	e	42	f	13502.7091	13502.7049	0.0042	rQ21(41.5)42,42 : A2Pi v=0 41.5 42 F2f 42 - X2Sigma+ v=0 41.5 41 F1e 42

Note: F' and F'' are the total angular momentum of the A and X states, respectively. p is the parity. Obs is the observed line position in cm^{-1} . Calc is the calculated line position in cm^{-1} . Obs-Calc is the difference between the observed and calculated line position in cm^{-1} . Line assignment illustrate the transition $^{\Delta N} \Delta J_{(F')F''}(J'')F', F'' : A^2\Pi v J' N' F1p/F2p F' - X^2\Sigma^+ v J'' N'' F1p/F2p F''$

Equilibrium constants were calculated for the $A^2\Pi$ state and are provided in Table 16. These equilibrium constants and the ground state equilibrium constants were used in Le Roy's RKR program [100] to calculate the RKR potential curves. The input file for the RKR program is given in Appendix A. Calculated RKR potential curves along with the transition dipole moments calculated in Section 4.3.2 were used in Le Roy's LEVEL program [101] to calculate the transition dipole matrix elements $\langle \psi_{e'v'} | \mu | \psi_{e''v''} \rangle$. The matrix elements were calculated for the levels connecting $v'' = 0 - 4$ and $v' = 0 - 3$, and are given in Table 17.

The band strengths were used in Equation (70) to calculate the Einstein A coefficients. Here v denotes the band origin for A-X $v' - v''$ transition, and $\mu_{v' \rightarrow v''}$ is the transition moment given in Table 17. The radiative lifetime for each vibrational level in the $A^2\Pi$ state was calculated with Equation (71) and is provided in Table 18. A line list was generated for the LaO $A^2\Pi-X^2\Sigma^+$ transition with PGOPHER for $J'' < 200$, and a sample is provided in Table 19. The complete list is provided as a supplementary file to Bernath et al. [76].

Table 16. Equilibrium constants of LaO for the $A^2\Pi$ state. The Table is from Bernath et al. [76].

$A^2\Pi$	
ω_e	762.104(37)
$\omega_e x_e$	2.209(11)
B_e	0.347149(18)
$10^3 \alpha_e$	1.615(12)

Note. All values are in cm^{-1}

Origins for the $v = 0$ and $v = 1$ of the $A^2\Pi$ state, as reported by Bernard and Sibai [77], are $13066.951(11) \text{ cm}^{-1}$ and $13824.166(10) \text{ cm}^{-1}$, respectively. These values align with ours (Table 14) within the margin of error. Equilibrium constants for each spin component of the A state were determined by Schoonveld and Sundaram [105]: for $A^2\Pi_{1/2}$, $\omega_e = 762.57 \text{ cm}^{-1}$, and $\omega_e x_e = 2.224 \text{ cm}^{-1}$; for $A^2\Pi_{3/2}$, $\omega_e = 761.60 \text{ cm}^{-1}$, and $\omega_e x_e = 2.235 \text{ cm}^{-1}$. Bernard and Sibai [77], in their analysis, provided the average values $\omega_e = 762.09 \text{ cm}^{-1}$ and $\omega_e x_e = 2.230 \text{ cm}^{-1}$, obtained from Schoonveld and Sundaram [105], and deduced $B_e = 0.34696 \text{ cm}^{-1}$ and $\alpha_e = 1.60 \times 10^{-3} \text{ cm}^{-1}$. Furthermore, Bernard and Vergés [80] presented $\omega_e = 762.0746 \text{ cm}^{-1}$, $\omega_e x_e = 2.18484 \text{ cm}^{-1}$,

Table 17. Band strengths of $A^2\Pi-X^2\Sigma^+$ transition of LaO. The Table is from Bernath et al. [76].

	$v'' = 0$	$v'' = 1$	$v'' = 2$	$v'' = 3$	$v'' = 4$
$v' = 0$	6.62051	1.10032	0.201760	2.56126×10^{-2}	3.15113×10^{-3}
$v' = 1$	-1.36251	6.35614	1.55011	0.352263	5.19018×10^{-2}
$v' = 2$	0.140159	-1.93922	6.07417	1.88565	0.499735
$v' = 3$	5.10630×10^{-3}	0.262560	-2.38161	5.77639	2.15735

Notes: All values are in debye.

Table 18. Radiative lifetimes of LaO $A^2\Pi$ state. The Table is from Bernath et al. [76].

$A^2\Pi v =$	0	1	2	3
τ_v (ns)	31.86	32.39	32.92	33.67

and $\omega_e y_e = -0.189 \times 10^{-2} \text{ cm}^{-1}$, along with $B_e = 0.3471671(36) \text{ cm}^{-1}$, $\alpha_e = 1.6094(14) \times 10^{-3} \text{ cm}^{-1}$, and $\gamma_e = 2.531(81) \times 10^{-6} \text{ cm}^{-1}$ for the $A^2\Pi$ state. In our $A^2\Pi-X^2\Sigma^+$ transition analysis, vibrational levels from $v' = 0$ up to $v' = 3$ were obtained, and for calculating equilibrium constants, a two-parameter fit was implemented. The calculated values in Table 16 align well with those reported in the literature. While no measured radiative lifetimes of the $A^2\Pi$ state are available, Ying and Gang [106] have performed calculations for $v = 0$ up to $v = 5$, with lifetimes ranging from 34.18 to 36.74 ns. The calculated lifetimes presented in Table 18 exhibit similar values.

In contrast to the $B^2\Sigma^+-X^2\Sigma^+$ transition of LaO, the $A^2\Pi-X^2\Sigma^+$ transition exhibits a highly dense spectrum (Figure 26). A closer examination of the 0-0 band head of the $A^2\Pi_{3/2}-X^2\Sigma^+$ sub-band is presented in Figure 30, where the simulated 0-0 band aligns well with the observed spectrum. However, there are slight disparities between the calculated band heads and the experimental spectrum. This minor discrepancy may be attributed to the discussed perturbations; nevertheless, the overall simulated $A^2\Pi-X^2\Sigma^+$ transition of LaO concurs with the observed spectrum.

Table 19. Sample line list of the LaO $A^2\Pi-X^2\Sigma^+$ transition. The Table is from Bernath et al. [76].

F'	F''	Position (cm^{-1})	E_{up} (cm^{-1})	E_{low} (cm^{-1})	A (s^{-1})	Line assignment
200	200	11320.5092	26810.0446	15489.5355	314729.9	pP1(202.5)200,200:A v=1 201.5 201 F1e 200 - X v=2 202.5 202 F1e 200
199	200	11320.5154	26810.0509	15489.5355	85673.51	pP1(202.5)199,200:A v=1 201.5 201 F1e 199 - X v=2 202.5 202 F1e 200
199	199	11320.5719	26810.0509	15489.479	435574.2	pQ12(201.5)199,199:A v=1 201.5 201 F1e 199 - X v=2 201.5 202 F2f 199
198	199	11320.5781	26810.0572	15489.479	65665.48	pQ12(201.5)198,199:A v=1 201.5 201 F1e 198 - X v=2 201.5 202 F2f 199
198	198	11320.6716	26810.0572	15489.3855	830192.2	pQ12(201.5)198,198:A v=1 201.5 201 F1e 198 - X v=2 201.5 202 F2f 198
199	199	11320.8984	26810.0509	15489.1525	394513	pP1(202.5)199,199:A v=1 201.5 201 F1e 199 - X v=2 202.5 202 F1e 199
198	199	11320.9046	26810.0572	15489.1525	66766.19	pP1(202.5)198,199:A v=1 201.5 201 F1e 198 - X v=2 202.5 202 F1e 199
200	200	11320.9491	26810.0446	15489.0956	515292.9	pQ12(201.5)200,200:A v=1 201.5 201 F1e 200 - X v=2 201.5 202 F2f 200
199	200	11320.9554	26810.0509	15489.0956	46800.07	pQ12(201.5)199,200:A v=1 201.5 201 F1e 199 - X v=2 201.5 202 F2f 200

Notes: F' and F'' are the total angular momentum of the A and X states, respectively. Position is the line position in cm^{-1} . E_{up} and E_{low} are the energies of the A and X states in cm^{-1} . Einstein A coefficients in s^{-1} are given under A. Line assignment illustrate the transition $\Delta^N \Delta_{(F')F_j} (J'') F' ; A^2\Pi v J' N' F1p/F2p F' - X^2\Sigma^+ v J'' N'' F1p/F2p F''$.

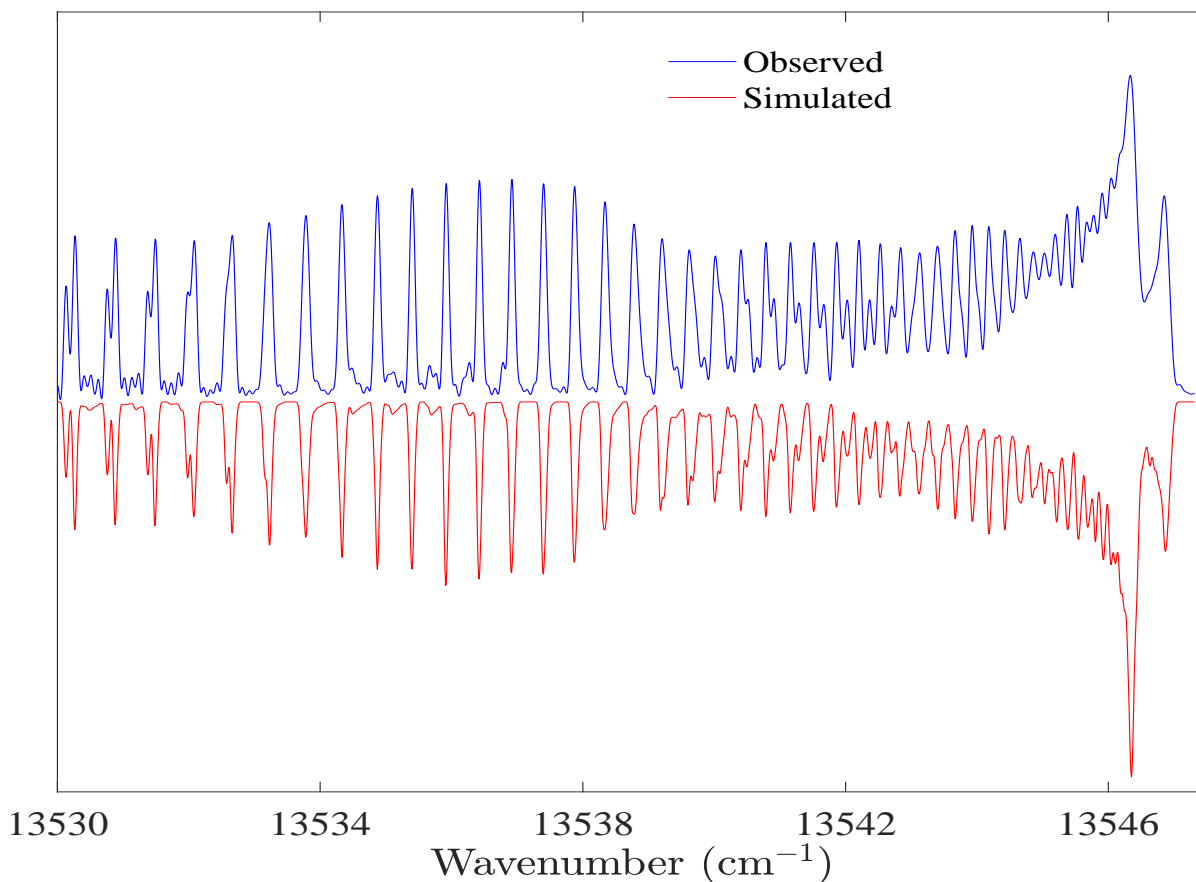


Figure 30. The 0-0 band of the $A^2\Pi_{3/2}-X^2\Sigma^+$ transition of LaO. (The observed spectrum appears in blue, while the simulated spectrum is represented in red.) The figure is from Bernath et al. [76].

4.4 YO TRANSITIONS

YO plays a significant role in stellar atmospheres, and the identification of the YO absorption spectrum serves as an indicator of S-type stars [107, 108]. YO exhibits six low-lying doublet states: $X^2\Sigma^+$, $A'^2\Delta$, $A^2\Pi$, $B^2\Sigma^+$, $C^2\Pi$, and $D^2\Sigma^+$. The electronic transitions $A^2\Pi - X^2\Sigma^+$ (orange system) and $B^2\Sigma^+ - X^2\Sigma^+$ have been identified in numerous spectra of cool S-type stars [21, 109–111]. Microwave studies have determined the spectroscopic parameters of the ground $X^2\Sigma^+$ state [84, 112, 113]. Johnson and Johnson [114] were the first to study the vibrational analysis of both $A^2\Pi - X^2\Sigma^+$ and $B^2\Sigma^+ - X^2\Sigma^+$ bands. Uhler and Akerlind [115] conducted the rotational analysis of the 0-0 band of the $A^2\Pi - X^2\Sigma^+$ and $B^2\Sigma^+ - X^2\Sigma^+$ transitions. Since then, there have been several studies on $A^2\Pi - X^2\Sigma^+$ and $B^2\Sigma^+ - X^2\Sigma^+$ transitions [85, 116–118]. The analysis of YO $A^2\Pi - X^2\Sigma^+$

and $B^2\Sigma^+-X^2\Sigma^+$ bands by Bernard et al. [85] was improved to include more vibrational levels, thus allowing for a detailed and precise analysis of both $A^2\Pi-X^2\Sigma^+$ [87] and $B^2\Sigma^+-X^2\Sigma^+$ bands [86]. The analysis on the $A^2\Pi-X^2\Sigma^+$ and $B^2\Sigma^+-X^2\Sigma^+$ transitions of YO is completed (*Manuscript in preparation*), and the rotational analysis on the $B^2\Sigma^+-X^2\Sigma^+$ transition of YO was carried out by myself.

4.4.1 Experimental Line Positions

Bernard and Gravina [86] conducted experiments by exciting YO in a hollow cathode discharge cooled with water circulation at room temperature. The discharge was achieved with argon at a total pressure of 2 Torr. A conventional Jaco-Ebert spectrograph was used in the second and third order of the grating, providing reciprocal dispersions of about 1 and 0.4 \AA mm^{-1} in the second and third order, respectively. The work conducted by Bernard and Gravina [86], represented an enhancement over the recorded spectrum, and the analysis performed by Bernard et al. [85].

Leung et al. [89] conducted an experimental study to observe the B-X transition's 2-0 and 2-1 bands using laser vaporization/reaction with free-jet expansion and cavity ring-down laser absorption spectroscopy. The generation of YO molecules involved the reaction of laser-vaporized Y atoms with a gas mixture containing approximately 2% oxygen and helium. A tunable Nd:YAG pump-dye laser operating in the 440-520 nm range was employed. The cavity ring-down absorption signal was detected using a photomultiplier tube. They measured the lines with an estimated absolute accuracy of about $\pm 0.2 \text{ cm}^{-1}$, however, the relative accuracy is reported to be about $\pm 0.05 \text{ cm}^{-1}$.

Experimental line positions reported by Bernard and Gravina [86] and Leung et al. [89] were utilized in the analysis of the $B^2\Sigma^+-X^2\Sigma^+$ transition.

4.4.2 $B^2\Sigma^+-X^2\Sigma^+$ Transition of YO

The rotational analysis of the YO $B^2\Sigma^+-X^2\Sigma^+$ transition was performed using PGOPHER. The standard Hamiltonians describing a $^2\Sigma^+$ state (Section 4.3.3) were employed to characterize the YO $B^2\Sigma^+$ and $X^2\Sigma^+$ states. The hyperfine interaction in these states, being too small to be observed, was omitted from the Hamiltonian [118].

Bernard and Gravina [86] explored nine emission bands (0-0, 0-1, 0-2, 1-0, 1-1, 1-2, 1-3, 3-2, and 4-3) within the $B^2\Sigma^+-X^2\Sigma^+$ system, successfully assigning 1740 lines. They provided a comprehensive catalog of experimental line positions, including the differences between observed and calculated values. These experimental data were utilized in our analysis of the YO $B^2\Sigma^+-X^2\Sigma^+$ transition. The higher J lines exhibited larger residual values between the observed and our

calculated line positions; as a result, some of these lines were fitted with reduced weights (see Table 20) to minimize the residual value. The rotational lines associated with the 2-0 and 2-1 bands of the $B^2\Sigma^+-X^2\Sigma^+$ transition were reported by Leung et al. [89]. Due to their relative accuracy of about $\pm 0.05 \text{ cm}^{-1}$, these measurements were deweighted in our analysis. Leung et al. [89] identified that the $v = 2$ level of the $B^2\Sigma^+$ is perturbed with the $C^2\Pi$ state of YO. The spectroscopic parameters to this perturbing $C^2\Pi$ and the perturbations were calculated. We have included this perturbation in the analysis of $B^2\Sigma^+-X^2\Sigma^+$ transition.

Ground state constants were derived from the analysis of $A^2\Pi-X^2\Sigma^+$ transition of YO and were kept fixed in the analysis of $B^2\Sigma^+-X^2\Sigma^+$ transition. A total of 1908 lines were assigned in the 0-0, 0-1, 0-2, 1-0, 1-1, 1-2, 1-3, 2-0, 2-1, 3-2, and 4-3 bands. A sample of the assigned lines of the $B^2\Sigma^+-X^2\Sigma^+$ transition is given in Table 20, and the whole set of lines will be provided as a supplementary file to the paper. The weighted average of the residual line positions in our fit is 0.058 cm^{-1} . The labeling for the lines provided in Table 20 is $\Delta J_{(F'_i)F''_j}(J'')$ in which J is the quantum number for total angular momentum exclusive of nuclear spin, and F'_i, F''_j ; subscripted $F_{i,j}$ are the customary labels for the two spin components of a $^2\Sigma^+$ state, 1 has $J = N + 1/2$ and 2 has $J = N - 1/2$. Single prime denotes the upper B state, and double prime denotes the lower X state. Ground state constants and the calculated $B^2\Sigma^+$ state constants are given in Table 21.

All bands resulting from the combinations of the $B^2\Sigma^+$ state and $X^2\Sigma^+$ state ($v = 0, 1, 2, 3$) were simulated using PGOPHER. Figure 31 displays the simulated bands of the $B^2\Sigma^+-X^2\Sigma^+$ system. Bands 1-3, 0-2, 4-1, and 3-0 exhibit low visibility, while bands 0-3, 3-3, and 4-0 are entirely invisible due to their low intensity compared to the other bands.

Table 20. Sample of observed and calculated line list of the $B^2\Sigma^+-X^2\Sigma^+$ transition of YO

J'	p'	J''	p''	Obs (cm^{-1})	Calc (cm^{-1})	Obs-Calc (cm^{-1})	StdDev	Line assignment
11.5	f	10.5	f	20749.4210	20749.4199	0.0011	1	R2(10.5) B v=0 11.5 12 F2f - X v=0 10.5 11 F2f
12.5	f	11.5	f	20749.8500	20749.8492	0.0008	1	R2(11.5) B v=0 12.5 13 F2f - X v=0 11.5 12 F2f
13.5	f	12.5	f	20750.2460	20750.2460	0.0000	1	R2(12.5) B v=0 13.5 14 F2f - X v=0 12.5 13 F2f
14.5	f	13.5	f	20750.6100	20750.6104	-0.0004	1	R2(13.5) B v=0 14.5 15 F2f - X v=0 13.5 14 F2f
15.5	f	14.5	f	20750.9430	20750.9424	0.0006	1	R2(14.5) B v=0 15.5 16 F2f - X v=0 14.5 15 F2f
16.5	f	15.5	f	20751.2390	20751.2419	-0.0029	1	R2(15.5) B v=0 16.5 17 F2f - X v=0 15.5 16 F2f
80.5	f	81.5	f	20575.8570	20575.7770	0.0800	10	P2(81.5) B v=0 80.5 81 F2f - X v=0 81.5 82 F2f
81.5	f	82.5	f	20572.3960	20572.3588	0.0372	10	P2(82.5) B v=0 81.5 82 F2f - X v=0 82.5 83 F2f
82.5	f	83.5	f	20568.9550	20568.9052	0.0498	10	P2(83.5) B v=0 82.5 83 F2f - X v=0 83.5 84 F2f
84.5	f	85.5	f	20561.9680	20561.8919	0.0761	10	P2(85.5) B v=0 84.5 85 F2f - X v=0 85.5 86 F2f
85.5	f	86.5	f	20558.4010	20558.3319	0.0691	10	P2(86.5) B v=0 85.5 86 F2f - X v=0 86.5 87 F2f
15.5	e	16.5	e	21353.9700	21354.0592	-0.0892	5	P1(16.5) B v=2 15.5 15 F1e - X v=1 16.5 16 F1e
16.5	e	17.5	e	21352.4500	21352.5615	-0.1115	5	P1(17.5) B v=2 16.5 16 F1e - X v=1 17.5 17 F1e
17.5	e	18.5	e	21350.8900	21351.0201	-0.1301	5	P1(18.5) B v=2 17.5 17 F1e - X v=1 18.5 18 F1e
18.5	e	19.5	e	21349.2400	21349.4344	-0.1944	5	P1(19.5) B v=2 18.5 18 F1e - X v=1 19.5 19 F1e
19.5	e	20.5	e	21347.6100	21347.8040	-0.1940	5	P1(20.5) B v=2 19.5 19 F1e - X v=1 20.5 20 F1e
20.5	e	21.5	e	21345.9100	21346.1282	-0.2182	5	P1(21.5) B v=2 20.5 20 F1e - X v=1 21.5 21 F1e

Notes: J' and J'' are the total angular momentum of the B and X states, respectively. p is the parity. Obs is the observed line position in cm^{-1} . Observed line positions are from Bernard and Gravina [86] and Leung et al. [89]. Calc is the calculated line position in cm^{-1} . Obs-Calc is the difference between the observed and calculated line position in cm^{-1} . StdDev is the deweighting factor. Less certain measurements are given larger values [90]. Line assignment illustrates the transition $\Delta J_{(F_1)F_2}^{\prime\prime}(J'') B v' J' N' F1p/F2p - X v'' J'' N'' F1p/F2p$.

Table 21. Spectroscopic constants of YO $B^2\Sigma^+$ and $X^2\Sigma^+$ states.

	$v=0$	$v=1$	$v=2$	$v=3$	$v=4$
T_v	0^a	855.7463 ^a	1705.8339 ^a	2550.2684 ^a	3389.0242 ^a
B_v	0.38800114 ^a	0.38628209 ^a	0.38454129 ^a	0.38283258 ^a	0.38105255 ^a
$10^7 D_v$	3.11368 ^a	3.14201 ^a	2.6550 ^a	3.18740 ^a	3.1233 ^a
T_v	20741.6778(49)	21492.4790(54)	22228.035(42)	22941.635(50)	23615.386(84)
B_v	0.3719086(34)	0.3694043(68)	0.36648(44)	0.362489(36)	0.3568669(531)
$10^7 D_v$	3.5720(41)	3.739(17)	12.7(84)	7.118(61)	5.661(79)
γ_v	-0.14521(10)	-0.14279(15)	-0.1359(77)	-0.13554(21)	-0.11186(20)

Notes: One standard deviation is given in parentheses. All values are in cm^{-1} . ^a Held Fixed during the analysis of $B^2\Sigma^+$ - $X^2\Sigma^+$.

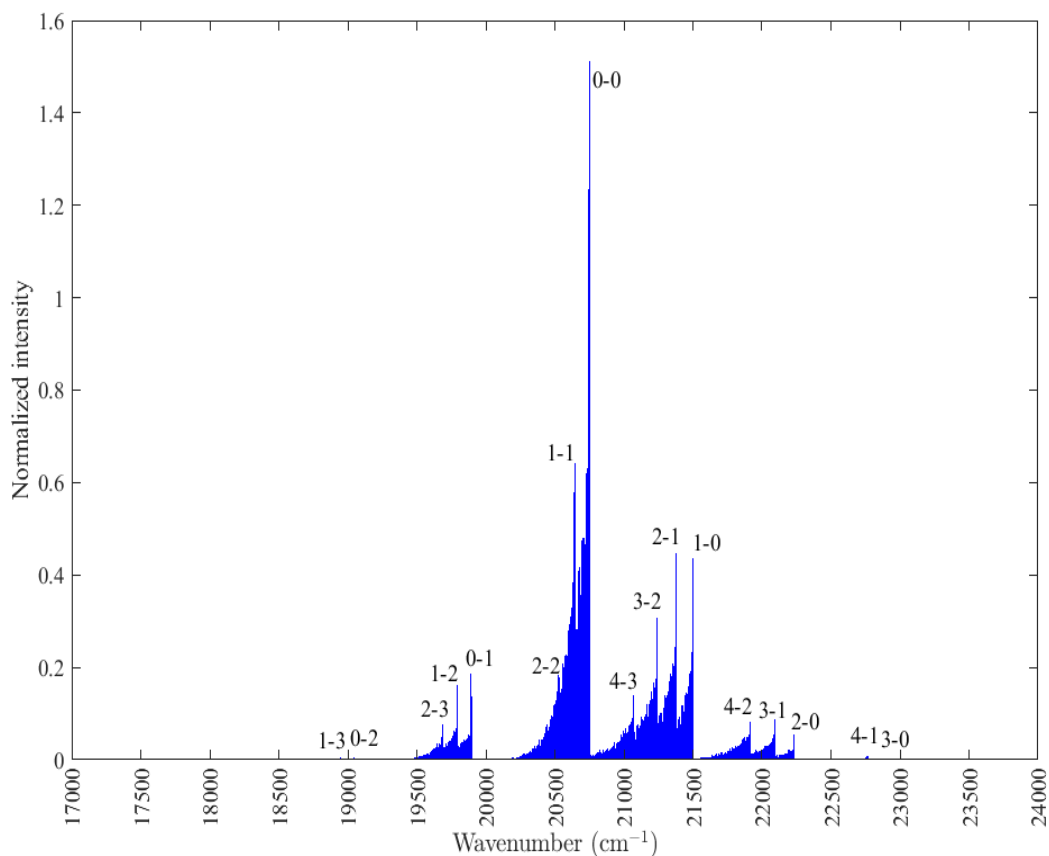


Figure 31. The simulated bands of $B^2\Sigma^+-X^2\Sigma^+$ transition of YO. The lines are assigned only in the 0-0, 0-1, 0-2, 1-0, 1-1, 1-2, 1-3, 2-0, 2-1, 3-2, and 4-3 bands.

The equilibrium coefficients for the $B^2\Sigma^+$ and $X^2\Sigma^+$ states were calculated (Table 22) and were used in Le Roy's RKR program [100] to calculate the RKR potential curves. The input files for the RKR program to calculate the RKR curves of YO $B^2\Sigma^+$ and $X^2\Sigma^+$ states are given in Appendix B. Smirnov et al. [119] calculated the transition dipole moments for $A^2\Pi-X^2\Sigma^+$ and $B^2\Sigma^+-X^2\Sigma^+$ transitions using CCSD(T)/CBS and MRCI methods. These dipole moments are calculated for bond lengths ranging from 1.58 to 2.36 Å, and can be found as supplementary data in Smirnov et al. [119]. Le Roy's LEVEL program [101] utilized these transition dipole moments along with RKR potentials (See Appendix B for the input file) to compute the transition dipole matrix elements $\langle \Psi_{e've} | \mu | \Psi_{e''ve''} \rangle$ for R(0), as presented in Table 23. The dissociation energies for each state were set to the values specified by Yurchenko et al. [88].

Table 22. Equilibrium constants for the $X^2\Sigma^+$ and $B^2\Sigma^+$ states of YO.

	$X^2\Sigma^+$	$B^2\Sigma^+$
ω_e	861.4121(71)	770.7(18)
$\omega_e x_e$	2.8310(14)	9.87(71)
B_e	0.388879(18)	0.372860(79)
$\alpha_e \times 10^3$	1.7347(63)	1.71(14)
$\gamma_e \times 10^4$...	3.89(43)

Notes: One standard deviation is given in parentheses. All values are in cm^{-1} .

Table 23. Band strengths of $B^2\Sigma^+ - X^2\Sigma^+$ transition.

	$v'' = 0$	$v'' = 1$	$v'' = 2$	$v'' = 3$
$v' = 0$	-3.36633	-1.34867	-0.297601	0.0256901
$v' = 1$	1.92170	-2.35639	-1.51862	-0.356792
$v' = 2$	-0.716153	2.39632	-1.34969	-1.37376
$v' = 3$	0.229068	-1.18746	2.48896	-0.392832
$v' = 4$	-0.0692750	0.464917	-1.63178	2.18785

Notes: All values are in debye. Band strengths should be multiplied by 0.96 (See text for details).

The band strengths were used in Equation (70) to calculate the Einstein A coefficients. Here $\mu_{v' \rightarrow v''}$ is the transition moment (band strength) given in Table 23. The radiative lifetime for each vibrational level in the $B^2\Sigma^+$ state was calculated using Equation (71). The radiative lifetimes of the $B^2\Sigma^+$ state at vibrational levels $v = 0$ and $v = 1$ were determined through experimental and theoretical methods. Using the laser-induced fluorescence technique, Liu and Parson [103] reported measured lifetimes of 30 ± 0.9 ns and 32.5 ± 1.2 ns for the $B^2\Sigma^+$ state at $v = 0$ and $v = 1$, respectively. An alternative experimental study by Zhang et al. [108] resulted in a measured lifetime of 38 ± 5 ns for the $B^2\Sigma^+$ state at $v = 0$. Theoretical calculations by Smirnov et al. [119]

yielded radiative lifetimes of 26.7 ns and 29.2 ns for the $B^2\Sigma^+$ state at $v = 0$ and $v = 1$, respectively. Yurchenko et al. [88] computed lifetimes of 31.1 ns and 30.8 ns for the $B^2\Sigma^+$ state at $v = 0$ and $v = 1$, respectively. We scaled our results to align our calculated lifetimes with the experimental values reported by Liu and Parson [103]. The initially calculated radiative lifetime values for $v = 0$ and $v = 1$ were 27.48 ns and 30.60 ns, respectively. Correction factors for each lifetime were calculated, and the average correction factor was applied to scale the reported band strengths for $B^2\Sigma^+ - X^2\Sigma^+$ (Table 23). The corrected band strengths are obtained by multiplying the values in Table 23 by a factor of 0.96. The scaled lifetimes for the $B^2\Sigma^+$ state at different vibrational levels are presented in Table 24.

Table 24. Radiative lifetimes of YO $B^2\Sigma^+$ state.

v'	0	1	2	3	4
$\tau_{v'}$ (ns)	29.82	33.21	37.68	45.25	45.91

A line list was generated for the YO $B^2\Sigma^+ - X^2\Sigma^+$ transition with PGOPHER for $J'' < 150$, and a sample is provided in Table 25. The complete list will be provided as a supplementary file with the manuscript.

The $B^2\Sigma^+ - X^2\Sigma^+$ transition exhibits weak intensity, as depicted in Figure 31, with the exception of bands $\Delta v = 0$ and $\Delta v = 1$. Our analysis of the $B^2\Sigma^+ - X^2\Sigma^+$ transition relies on previously reported observational lines from Bernard and Gravina [86] and Leung et al. [89] covering the spectral bands 0-0, 0-1, 0-2, 1-0, 1-1, 1-2, 1-3, 2-0, 2-1, 3-2, and 4-3. All bands involving $v'' = 0, 1, 2, 3$ and $v' = 0, 1, 2, 3, 4$ are simulated using PGOPHER. The energy levels of the $B^2\Sigma^+$ state for $v = 0$ to $v = 4$ were determined, with agreement on the origins of these levels with Bernard and Gravina [86]. However, discrepancies with Bernard et al. [85] were noted for $v = 1$. Vibrational perturbations became apparent in the $B^2\Sigma^+$ state for $v \geq 2$, and reported constants by Bernard and Gravina [86] include the influence of these perturbations. Iterative calculations by Bernard and Gravina [86] using Pekeris's formula yielded effective constants, $\omega_e = 758.73 \text{ cm}^{-1}$ and $\omega_e x_e = 3.97 \text{ cm}^{-1}$. Ab initio calculations by Smirnov et al. [119] included several basis sets with $\omega_e = 780.6 - 785.3 \text{ cm}^{-1}$ and $\omega_e x_e = 2.94 - 3.01 \text{ cm}^{-1}$. Our calculated value, $\omega_e = 770.7(18) \text{ cm}^{-1}$ has a large standard deviation, and $\omega_e x_e = 9.87(71) \text{ cm}^{-1}$, showed deviations, likely influenced

Table 25. Sample line list of the YO B²Σ⁺-X²Σ⁺ transition.

J'	J''	Position (cm ⁻¹)	E_{up} (cm ⁻¹)	E_{low} (cm ⁻¹)	A (s ⁻¹)	$f \times 10^6$	Line Assignment
68.5	69.5	18081.9566	22473.872	4391.9154	616.2448	2.7853	pP1(69.5) B v=0 68.5 68 F1e - X v=3 69.5 69 F1e
67.5	68.5	18084.3109	22423.8143	4339.5035	616.5498	2.78536	pP1(68.5) B v=0 67.5 67 F1e - X v=3 68.5 68 F1e
66.5	67.5	18086.6417	22374.4809	4287.8392	616.8545	2.78542	pP1(67.5) B v=0 66.5 66 F1e - X v=3 67.5 67 F1e
65.5	66.5	18088.9492	22325.8724	4236.9232	617.1588	2.78546	pP1(66.5) B v=0 65.5 65 F1e - X v=3 66.5 66 F1e
64.5	65.5	18091.2333	22277.9892	4186.7559	617.4630	2.78549	pP1(65.5) B v=0 64.5 64 F1e - X v=3 65.5 65 F1e
63.5	64.5	18093.4942	22230.8321	4137.3379	617.7671	2.78551	pP1(64.5) B v=0 63.5 63 F1e - X v=3 64.5 64 F1e
66.5	67.5	18094.1123	22433.6158	4339.5035	617.6192	2.78657	pP2(67.5) B v=0 66.5 67 F2f - X v=3 67.5 68 F2f
62.5	63.5	18095.7319	22184.4015	4088.6696	618.0712	2.78551	pP1(63.5) B v=0 62.5 62 F1e - X v=3 63.5 63 F1e
65.5	66.5	18096.2979	22384.1372	4287.8392	617.9113	2.78659	pP2(66.5) B v=0 65.5 66 F2f - X v=3 66.5 67 F2f
61.5	62.5	18097.9464	22138.698	4040.7516	618.3754	2.7855	pP1(62.5) B v=0 61.5 61 F1e - X v=3 62.5 62 F1e

Notes: J' and J'' are the total angular momentum of the B and X states, respectively. E_{up} and E_{low} are the energies of B and X state in (cm⁻¹).

Einstein coefficients are given under A in s⁻¹. f is the oscillator strength. Line assignment illustrate the transition $\Delta N \Delta J_{(F)} F''(J'')$ B v' J' N'

$F1p/F2p - X v'' J'' N'' F1p/F2p$.

by perturbations in vibrational states $v \geq 2$. Agreement was found for B_e and α_e values, with our calculations matching those of Bernard and Gravina [86]. Perturbations in the $B^2\Sigma^+$ state, especially for $v \geq 2$, were noted by Leung et al. [89], emphasizing the importance of identifying specific perturbations for precise line assignments.

CHAPTER 5

CONCLUSION AND FUTURE WORKS

The successful detection of hydrocarbons in planetary atmospheres hinges upon the availability of accurate spectroscopic line lists, parameters, and absorption cross-sections. Given the diverse range of environments across exoplanets, moons, and earth's atmosphere, variations in temperature, pressure, and broadening gases necessitate comprehensive spectroscopic data for meaningful interpretation of planetary spectra.

Our work encompasses high-resolution absorption cross-sections for ethane, neopentane, propene, and *n*-butane across different temperatures, pressures, and broadening gases, including hydrogen, helium, and nitrogen. By expanding the absorption cross sections to incorporate diverse atmospheric conditions, we enhance our capacity to analyze and interpret planetary spectra effectively. This comprehensive approach not only contributes to our understanding of planetary atmospheres but also lays the foundation for future investigations into the composition and dynamics of hydrocarbons in atmospheres of exoplanets, earth, and moons. Opportunities for enhancement in hydrocarbon data persist, presenting avenues for refining existing datasets by acquiring high-resolution spectra. Expansion of the spectral coverage to encompass broader wavenumber regions, alongside the inclusion of additional pressures and temperatures, stands as a viable means to enrich existing spectroscopic data sets. Furthermore, including additional hydrocarbons of interest would further enrich the catalog, facilitating a more comprehensive understanding of their spectroscopic properties and their role in various planetary atmospheres.

HOCl is a chlorine reservoir molecule in the earth's stratosphere and a key species in polar ozone destruction. Atmospheric HFC abundances are rapidly increasing because of the phase-out of the production and consumption of CFCs and HCFCs. HFCs are also responsible for indirect stratospheric ozone destruction due to the higher global warming potentials. Utilizing solar occultation spectra from the ACE satellite, we have examined both HOCl and HFC-32, shedding light on their vertical distribution profiles, altitude-latitude profiles, and seasonal variations. Our analysis of HOCl volume mixing ratios (VMRs) and presentation of altitude-latitude profiles reveal noteworthy insights, mainly showcasing a marginally significant decline in HOCl VMRs over time, a testament to the effectiveness of the Montreal Protocol in ozone preservation. ACE-FTS data was able to provide the first remote sensing retrievals of HFC-32. The altitude-latitude profiles and the time series quarterly averages are provided for the HFC-32. The data reveals a pronounced increase in HFC-32 VMRs in the northern hemisphere, where most emitters are concentrated. Our

comparison of ACE HFC-32 data with in situ flask measurements from NOAA offers valuable validation. Moreover, a noticeable trend of exponential growth in HFC-32 VMRs underscores the critical need to implement effective mitigation strategies outlined by the Montreal Protocol to limit its atmospheric buildup and mitigate potential environmental repercussions.

For two decades, ACE has orbited Earth, capturing infrared spectra during sunrise and sunset for 46 atmospheric molecules, alongside monitoring sulfate aerosols from volcanic eruptions and smoke from wildfires. Continuously expanding its collection, ACE offers a wealth of data products through infrared spectroscopy. Looking ahead, ACE data holds promise for investigating atmospheric dynamics and chemistry, biomass burning, and assessing aerosols and clouds, among other avenues of research.

Throughout history, astronomers have been fascinated by the universe and the complex processes involved in creating elements. Heavy elements such as LaO and YO are formed in the cool atmospheres of S-type stars through the *s*-process. This process involves the absorption of neutrons followed by β -decay, and it mainly occurs during the late asymptotic giant branch (AGB) phase of stellar evolution. Spectral signatures of LaO and YO have been found in the spectra of S-type stars, providing valuable information about their chemical composition and evolution. In this study, we conducted a thorough analysis of the vibrational bands in the $B^2\Sigma^+-X^2\Sigma^+$ and $A^2\Pi-X^2\Sigma^+$ transitions of LaO, as well as the $B^2\Sigma^+-X^2\Sigma^+$ transitions of YO. We calculated spectroscopic parameters and compiled a detailed line list to help astronomers interpret and understand the spectra of S-type stars. Our goal is to provide essential tools for interpreting stellar spectra and deepen the understanding of the formation of heavy elements in the cosmos.

The $C^2\Pi-X^2\Sigma^+$ transition of LaO is under investigation. The states' Hamiltonian is described in Sections 4.3.3 and 4.3.4. Much like the $A^2\Pi-X^2\Sigma^+$ transition of LaO, the $C^2\Pi-X^2\Sigma^+$ transition also exhibits two spin components separated by approximately 220 cm^{-1} . The origin of the 0-0 transition in $C^2\Pi_{1/2}-X^2\Sigma^+$ is approximately 22600 cm^{-1} , while for $C^2\Pi_{3/2}-X^2\Sigma^+$, it is around 22800 cm^{-1} . Green [120] have studied the $C^2\Pi-X^2\Sigma^+$ transition through an Ebert mount spectrograph and published a line list containing the 0-0 band. Similar to other analyses of LaO transition, we are using the experimental spectrum recorded at Kitt Peak (Section 4.3.1) as an overlay. $C^2\Pi-X^2\Sigma^+$ transition is a weak transition compared to other LaO transitions, and hence assigning lines is difficult. We have also recorded an experimental spectrum of LaO here at ODU using the hollow cathode discharge technique. A hollow Cu cathode was prepared by mixing LaO powder with pure Cu powder and was placed in an evacuated gas flow chamber, and Ar was used as a buffer gas. An electric discharge was obtained using a DC voltage source. The LaO spectrum was recorded with a Bruker IFS 125 HR spectrometer. This recorded spectrum shows

the $C^2\Pi_{1/2}-X^2\Sigma^+$ well but not the other subband. We simultaneously use Kitt Peak's recorded spectrum and ours to assign lines and continue the rotational analysis with PGOPHER.

Propene ($\text{CH}_2=\text{CHCH}_3$) stands as the first unsaturated C_3 hydrocarbon species detected in the stratosphere of Titan by Cassini [121]. To further enhance our understanding of Titan's atmosphere and those of giant planets, we have generated absorption cross sections of propene broadened by hydrogen, helium, and nitrogen (See Section 2.2.3). These cross sections, spanning the 450–1250 cm^{-1} region and the CH stretching region, facilitate atmospheric characterization efforts. With the recent launch of the James Webb Space Telescope (JWST), there is an opportunity to gather additional data on these celestial bodies. The higher resolution of JWST enables the detection of features stemming from weak bands, underscoring the importance of our ongoing rotational analysis of propene.

Propene is a molecule with an internal methyl rotor. Propene has a considerable potential barrier against the torsional motion of the methyl group [45, 122]. The symmetry of the CH_3 group makes the rotational levels split into two levels, A and E. This splitting appears as a fine structure on the rotational levels [122]. Propene has 21 fundamental vibrational modes, all of which are infrared active [45]. The absorption cross sections we publish cover the fundamental band ν_{20} which is centered around 576.27 cm^{-1} , and this work focuses on the rotational analysis of the ν_{20} band of propene.

Propene is regarded as a molecule with C_s symmetry and has dipole moments of $\mu_a = 0.36$ D and $\mu_b = 0.05$ D [122]. The propene can be simulated with PGOPHER as an asymmetric top, thus simulating only the A symmetry. A modified version of the ERHAM program is also employed to simulate the entire ν_{20} band of propene. ERHAM, an Effective Rotational Hamiltonian model, handles molecules with two periodic large-amplitude internal motions or a single internal rotor [123]. Peter Groner has adapted the ERHAM program to simulate the infrared active bands of propene, and our collaborative effort with him encompasses the rotational analysis of the ν_{20} band.

REFERENCES

- [1] Bernath, P.F.: *Spectra of Atoms and Molecules*. Oxford university press, New York (2020)
- [2] Brown, J.M., Carrington, A.: *Rotational Spectroscopy of Diatomic Molecules*. Cambridge university press, Cambridge (2003)
- [3] Bernath, P.: The Atmospheric Chemistry Experiment (ACE). *Journal of Quantitative Spectroscopy and Radiative Transfer* **186**, 3–16 (2017)
- [4] Finlayson-Pitts, B.J., Pitts Jr, J.N.: *Chemistry of the Upper and Lower Atmosphere: Theory, Experiments, and Applications*. Academic press, California (1999)
- [5] Taylor, F.W.: Planetary atmospheres. *Meteorological Applications* **17**(4), 393–403 (2010)
- [6] Hörst, S.M.: Titan’s atmosphere and climate. *Journal of Geophysical Research: Planets* **122**(3), 432–482 (2017)
- [7] Marcq, E., Mills, F.P., Parkinson, C.D., Vandaele, A.C.: Composition and chemistry of the neutral atmosphere of Venus. *Space Science Reviews* **214**, 1–55 (2018)
- [8] Seager, S.: The future of spectroscopic life detection on exoplanets. *Proceedings of the National Academy of Sciences* **111**(35), 12634–12640 (2014)
- [9] Kostiuk, T., Espenak, F., Mumma, M.J., Romani, P.: Infrared studies of hydrocarbons on Jupiter. *Infrared physics* **29**(2-4), 199–204 (1989)
- [10] Sagan, C., Khare, B., Thompson, W., McDonald, G., Wing, M.R., Bada, J.L., Vo-Dinh, T., Arakawa, E.: Polycyclic aromatic hydrocarbons in the atmospheres of Titan and Jupiter. *Astrophysical Journal, Part 1 (ISSN 0004-637X), vol. 414, no. 1, p. 399-405.* **414**, 399–405 (1993)
- [11] Sada, P.V., Bjoraker, G.L., Jennings, D.E., McCabe, G.H., Romani, P.N.: Observations of CH₄, C₂H₆, and C₂H₂ in the stratosphere of Jupiter. *Icarus* **136**(2), 192–201 (1998)
- [12] Fouchet, T., Lellouch, E., Bézard, B., Feuchtgruber, H., Drossart, P., Encrenaz, T.: Jupiter’s hydrocarbons observed with ISO-SWS: vertical profiles of C₂H₆ and C₂H₂, detection of CH₃C₂H. *Astronomy and Astrophysics* **355**, 13–17 (2000)

- [13] Bézard, B., Feuchtgruber, H., Encrenaz, T.: Observations of hydrocarbons in the giant planets. In: *The Universe as Seen by ISO*, vol. 427, p. 153 (1999)
- [14] Moses, J.I., Bézard, B., Lellouch, E., Gladstone, G.R., Feuchtgruber, H., Allen, M.: Photochemistry of Saturn's atmosphere: I. hydrocarbon chemistry and comparisons with ISO observations. *Icarus* **143**(2), 244–298 (2000)
- [15] Sada, P.V., Bjoraker, G.L., Jennings, D.E., Romani, P.N., McCabe, G.H.: Observations of C_2H_6 and C_2H_2 in the stratosphere of Saturn. *Icarus* **173**(2), 499–507 (2005)
- [16] Meadows, V.S., Orton, G., Line, M., Liang, M.-C., Yung, Y.L., Van Cleve, J., Burgdorf, M.J.: First Spitzer observations of Neptune: Detection of new hydrocarbons. *Icarus* **197**(2), 585–589 (2008)
- [17] Clark, R.N., Curchin, J.M., Barnes, J.W., Jaumann, R., Soderblom, L., Cruikshank, D.P., Brown, R.H., Rodriguez, S., Lunine, J., Stephan, K., et al.: Detection and mapping of hydrocarbon deposits on Titan. *Journal of Geophysical Research: Planets* **115**(E10) (2010)
- [18] Wakelam, V., Herbst, E.: Polycyclic aromatic hydrocarbons in dense cloud chemistry. *The Astrophysical Journal* **680**(1), 371 (2008)
- [19] Cernicharo, J., Agúndez, M., Cabezas, C., Tercero, B., Marcelino, N., Pardo, J.R., De Vicente, P.: Pure hydrocarbon cycles in TMC-1: Discovery of ethynyl cyclopropenyldiene, cyclopentadiene, and indene. *Astronomy & Astrophysics* **649**, 15 (2021)
- [20] Cernicharo, J., Agúndez, M., Kaiser, R., Cabezas, C., Tercero, B., Marcelino, N., Pardo, J., De Vicente, P.: Discovery of benzyne, $o-C_6H_4$, in TMC-1 with the QUIJOTE line survey. *Astronomy & Astrophysics* **652**, 9 (2021)
- [21] Wyckoff, S., Clegg, R.: Molecular spectra of pure S stars. *Monthly Notices of the Royal Astronomical Society* **184**(1), 127–143 (1978)
- [22] O'Brien, J.J., Cao, H.: Absorption spectra and absorption coefficients for methane in the 750–940 nm region obtained by intracavity laser spectroscopy. *Journal of Quantitative Spectroscopy and Radiative Transfer* **75**(3), 323–350 (2002)
- [23] Melin, H., Fletcher, L., Donnelly, P., Greathouse, T., Lacy, J., Orton, G., Giles, R., Sinclair, J., Irwin, P.: Assessing the long-term variability of acetylene and ethane in the stratosphere of Jupiter. *Icarus* **305**, 301–313 (2018)

- [24] Hesman, B.E., Jennings, D.E., Sada, P.V., Bjoraker, G.L., Achterberg, R.K., Simon-Miller, A.A., Anderson, C.M., Boyle, R.J., Nixon, C.A., Fletcher, L.N., *et al.*: Saturn's latitudinal C₂H₂ and C₂H₆ abundance profiles from Cassini/CIRS and ground-based observations. *Icarus* **202**(1), 249–259 (2009)
- [25] Greathouse, T.K., Richter, M., Lacy, J., Moses, J., Orton, G., Encrenaz, T., Hammel, H.B., Jaffe, D.: A spatially resolved high spectral resolution study of Neptune's stratosphere. *Icarus* **214**(2), 606–621 (2011)
- [26] Bishop, J., Atreya, S.K., Herbert, F., Romani, P.: Reanalysis of Voyager 2 UVS occultations at Uranus: Hydrocarbon mixing ratios in the equatorial stratosphere. *Icarus* **88**(2), 448–464 (1990)
- [27] Trainer, M.G., Pavlov, A.A., DeWitt, H.L., Jimenez, J.L., McKay, C.P., Toon, O.B., Tolbert, M.A.: Organic haze on Titan and the early Earth. *Proceedings of the National Academy of Sciences* **103**(48), 18035–18042 (2006)
- [28] Raulin, F., Cerceau, F., Hakdaoui, M., Vargas, A.: Prebiotic chemical evolution in Titan's ocean. *Origins of life and evolution of the biosphere* **16**, 401–402 (1986)
- [29] Bernath, P., Dodangodage, R., Dulick, M., Zhao, J., Billinghamurst, B.: Absorption cross sections for neopentane broadened by nitrogen in the 3.3 μm region. *Journal of Quantitative Spectroscopy and Radiative Transfer* **251**, 107034 (2020)
- [30] Helmig, D., Rossabi, S., Hueber, J., Tans, P., Montzka, S.A., Masarie, K., Thoning, K., Plass-Duelmer, C., Claude, A., Carpenter, L.J., *et al.*: Reversal of global atmospheric ethane and propane trends largely due to us oil and natural gas production. *Nature Geoscience* **9**(7), 490–495 (2016)
- [31] Guerlet, S., Fouchet, T., Bézard, B., Simon-Miller, A.A., Flasar, F.M.: Vertical and meridional distribution of ethane, acetylene and propane in Saturn's stratosphere from CIRS/Cassini limb observations. *Icarus* **203**(1), 214–232 (2009)
- [32] Dodangodage, R., Bernath, P.F., Zhao, J., Billinghamurst, B.: Absorption cross sections for ethane broadened by hydrogen and helium in the 3.3 micron region. *Journal of Quantitative Spectroscopy and Radiative Transfer* **253**, 107131 (2020)
- [33] Dodangodage, R., Bernath, P.F., Zhao, J., Billinghamurst, B.: Absorption cross sections in the CH stretching region for propene broadened by helium and nitrogen. *Journal of Quantitative Spectroscopy and Radiative Transfer* **271**, 107738 (2021)

- [34] Bernath, P.F., Dodangodage, R., Zhao, J., Billingham, B.: Infrared absorption cross sections for propene broadened by N₂ (450–1250 cm⁻¹) and by H₂ (2680–3220 cm⁻¹). *Journal of Quantitative Spectroscopy and Radiative Transfer* **296**, 108462 (2023)
- [35] Sorensen, J.J., Bernath, P.F., Johnson, R.M., Dodangodage, R., Cameron, W.D., LaBelle, K.: Absorption cross sections of *n*-butane, *n*-pentane, cyclopentane and cyclohexane. *Journal of Quantitative Spectroscopy and Radiative Transfer* **290**, 108284 (2022)
- [36] Hargreaves, R.J., Buzan, E., Dulick, M., Bernath, P.F.: High-resolution absorption cross sections of C₂H₆ at elevated temperatures. *Molecular Astrophysics* **1**, 20–25 (2015)
- [37] Dougherty, M., Esposito, L., Krimigis, S.M.: *Saturn from Cassini-Huygens*. Springer, Netherlands (2009)
- [38] Hewett, D., Bernath, P., Zhao, J., Billingham, B.: Near infrared absorption cross sections for ethane broadened by hydrogen and nitrogen. *Journal of Quantitative Spectroscopy and Radiative Transfer* **242**, 106780 (2020)
- [39] Harrison, J.J., Allen, N.D., Bernath, P.F.: Infrared absorption cross sections for ethane (C₂H₆) in the 3 μm region. *Journal of Quantitative Spectroscopy and Radiative Transfer* **111**(3), 357–363 (2010)
- [40] Bernath, P., Sibert III, E.L., LaBelle, K., Zhao, J., Billingham, B.: Absorption cross sections and local mode analysis for neopentane. *Journal of Quantitative Spectroscopy and Radiative Transfer* **293**, 108390 (2022)
- [41] Mirkin, N., Krimm, S.: Ab initio analysis of the vibrational spectra of conformers of some branched alkanes. *Journal of Molecular Structure* **550**, 67–91 (2000)
- [42] Bernath, P.F., Sibert III, E.L., Dulick, M.: Neopentane vibrations: High resolution spectra and anharmonic calculations. *The Journal of Physical Chemistry A* **124**(17), 3438–3444 (2020)
- [43] Gordon, I.E., Rothman, L.S., Hill, C., Kochanov, R.V., Tan, Y., Bernath, P.F., Birk, M., Boudon, V., Campargue, A., Chance, K., *et al.*: The HITRAN2016 molecular spectroscopic database. *Journal of Quantitative Spectroscopy and Radiative Transfer* **203**, 3–69 (2017)
- [44] Lord, R., Venkateswarlu, P.: The infrared spectra of propylene and propylene-d₆. *JOSA* **43**(11), 1079–1085 (1953)

- [45] Sung, K., Toon, G.C., Drouin, B.J., Mantz, A.W., Smith, M.A.H.: FT-IR measurements of cold propene (C_3H_6) cross-sections at temperatures between 150 and 299 K. *Journal of Quantitative Spectroscopy and Radiative Transfer* **213**, 119–132 (2018)
- [46] Mills, I., Whiffen, D.: Integration theorems on vibrational intensities. *The Journal of Chemical Physics* **30**(6), 1619–1620 (1959)
- [47] Es-sebbar, E.T., Alrefae, M., Farooq, A.: Infrared cross-sections and integrated band intensities of propylene: Temperature-dependent studies. *Journal of Quantitative Spectroscopy and Radiative Transfer* **133**, 559–569 (2014)
- [48] Sharpe, S.W., Johnson, T.J., Sams, R.L., Chu, P.M., Rhoderick, G.C., Johnson, P.A.: Gas-phase databases for quantitative infrared spectroscopy. *Applied spectroscopy* **58**(12), 1452–1461 (2004)
- [49] Durig, J., Wang, A., Beshir, W., Little, T.: Barrier to asymmetric internal rotation, conformational stability, vibrational spectra and assignments, and ab initio calculations of *n*-butane- d_0 , d_5 and d_{10} . *Journal of Raman spectroscopy* **22**(11), 683–704 (1991)
- [50] Gordon, I.E., Rothman, L.S., Hargreaves, R., Hashemi, R., Karlovets, E.V., Skinner, F., Conway, E.K., Hill, C., Kochanov, R.V., Tan, Y., *et al.*: The HITRAN2020 molecular spectroscopic database. *Journal of quantitative spectroscopy and radiative transfer* **277**, 107949 (2022)
- [51] Bernath, P., Dodandodage, R., Boone, C., Crouse, J.: HOCl retrievals from the Atmospheric Chemistry Experiment. *Journal of Quantitative Spectroscopy and Radiative Transfer* **264**, 107559 (2021)
- [52] Dodangodage, R., Bernath, P., Boone, C., Crouse, J., Harrison, J.: The first remote-sensing measurements of HFC-32 in the Earth's atmosphere by the Atmospheric Chemistry Experiment Fourier Transform Spectrometer (ACE-FTS). *Journal of Quantitative Spectroscopy and Radiative Transfer* **272**, 107804 (2021)
- [53] Bernath, P., Steffen, J., Crouse, J., Boone, C.: Sixteen-year trends in atmospheric trace gases from orbit. *Journal of Quantitative Spectroscopy and Radiative Transfer* **253**, 107178 (2020)
- [54] Boone, C., Bernath, P., Cok, D., Jones, S., Steffen, J.: Version 4 retrievals for the Atmospheric Chemistry Experiment fourier transform spectrometer (ACE-FTS) and imagers. *Journal of Quantitative Spectroscopy and Radiative Transfer* **247**, 106939 (2020)

- [55] Molina, M.J., Rowland, F.S.: Stratospheric sink for chlorofluoromethanes: chlorine atom-catalysed destruction of ozone. *Nature* **249**(5460), 810–812 (1974)
- [56] Montreal Protocol on substances that deplete the ozone layer. *Washington, DC: US Government Printing Office* **26**, 128–136 (1987)
- [57] Scientific assessment of ozone depletion: 2018, global ozone research and monitoring project-report no. 58. World Meteorological Organization (2018)
- [58] Hodnebrog, Ø., Aamaas, B., Fuglestvedt, J.S., Marston, G., Myhre, G., Nielsen, C.J., Sandstad, M., Shine, K.P., Wallington, T.J.: Updated global warming potentials and radiative efficiencies of halocarbons and other weak atmospheric absorbers. *Reviews of Geophysics* **58**(3) (2020)
- [59] Amendment to the Montreal Protocol on substances that deplete the ozone layer (Kigali amendment). *International Legal Materials* **56**(1), 193–205 (2017)
- [60] Solomon, S.: Stratospheric ozone depletion: A review of concepts and history. *Reviews of geophysics* **37**(3), 275–316 (1999)
- [61] Müller, R., Groöß, J.-U., Zafar, A.M., Robrecht, S., Lehmann, R.: The maintenance of elevated active chlorine levels in the Antarctic lower stratosphere through HCl null cycles. *Atmospheric Chemistry and Physics* **18**(4), 2985–2997 (2018)
- [62] Clarmann, T., Glatthor, N., Grabowski, U., Höpfner, M., Kellmann, S., Linden, A., Mengistu Tsidu, G., Milz, M., Steck, T., Stiller, G., et al.: Global stratospheric HOCl distributions retrieved from infrared limb emission spectra recorded by the Michelson Interferometer for Passive Atmospheric Sounding (MIPAS). *Journal of Geophysical Research: Atmospheres* **111**(D5) (2006)
- [63] Kreyling, D., Sagawa, H., Wohltmann, I., Lehmann, R., Kasai, Y.: SMILES zonal and diurnal variation climatology of stratospheric and mesospheric trace gasses: O₃, HCl, HNO₃, ClO, BrO, HOCl, HO₂, and temperature. *Journal of Geophysical Research: Atmospheres* **118**(20), 11–888 (2013)
- [64] Manney, G.L., Livesey, N.J., Santee, M.L., Froidevaux, L., Lambert, A., Lawrence, Z.D., Millán, L.F., Neu, J.L., Read, W.G., Schwartz, M.J., et al.: Record-low Arctic stratospheric ozone in 2020: MLS observations of chemical processes and comparisons with previous extreme winters. *Geophysical Research Letters* **47**(16), 2020–089063 (2020)

- [65] Bernath, P., Fernando, A.M.: Trends in stratospheric HCl from the ACE satellite mission. *Journal of Quantitative Spectroscopy and Radiative Transfer* **217**, 126–129 (2018)
- [66] Kovalenko, L., Jucks, K., Salawitch, R., Toon, G., Blavier, J.-F., Johnson, D., Kleinböhl, A., Livesey, N., Margitan, J., Pickett, H., et al.: Observed and modeled HOCl profiles in the midlatitude stratosphere: Implication for ozone loss. *Geophysical research letters* **34**(19) (2007)
- [67] Khosravi, M., Baron, P., Urban, J., Froidevaux, L., Jonsson, A., Kasai, Y., Kuribayashi, K., Mitsuda, C., Murtagh, D.P., Sagawa, H., et al.: Diurnal variation of stratospheric and lower mesospheric HOCl, ClO and HO₂ at the equator: comparison of 1-D model calculations with measurements by satellite instruments. *Atmospheric Chemistry and Physics* **13**(15), 7587–7606 (2013)
- [68] Prinn, R.G., Weiss, R.F., Arduini, J., Arnold, T., DeWitt, H.L., Fraser, P.J., Ganesan, A.L., Gasore, J., Harth, C.M., Hermansen, O., et al.: History of chemically and radiatively important atmospheric gases from the Advanced Global Atmospheric Gases Experiment (AGAGE). *Earth System Science Data* **10**(2), 985–1018 (2018)
- [69] Grealley, B., Simmonds, P., O’Doherty, S., McCulloch, A., Miller, B., Salameh, P., Mühle, J., Tanhua, T., Harth, C., Weiss, R., et al.: Improved continuous in situ measurements of C₁-C₃ PFCs, HFCs, HCFCs, CFCs and SF₆ in Europe and Australia. *Environmental Sciences* **2**(2-3), 253–261 (2005)
- [70] Montzka, S., McFarland, M., Andersen, S., Miller, B., Fahey, D., Hall, B., Hu, L., Siso, C., Elkins, J.: Recent trends in global emissions of hydrochlorofluorocarbons and hydrofluorocarbons: Reflecting on the 2007 adjustments to the Montreal Protocol. *The Journal of Physical Chemistry A* **119**(19), 4439–4449 (2015)
- [71] Boone, C., Bernath, P., Lecours, M.: Version 5 retrievals for ACE-FTS and ACE-imagers. *Journal of Quantitative Spectroscopy and Radiative Transfer*, 108749 (2023)
- [72] Ji, A.P., Drout, M.R., Hansen, T.T.: The lanthanide fraction distribution in metal-poor stars: a test of neutron star mergers as the dominant r-process site. *The Astrophysical Journal* **882**(1), 40 (2019)
- [73] Johnson, J.A.: Populating the periodic table: Nucleosynthesis of the elements. *Science* **363**(6426), 474–478 (2019)

- [74] Neyskens, P., Van Eck, S., Jorissen, A., Goriely, S., Siess, L., Plez, B.: The temperature and chronology of heavy-element synthesis in low-mass stars. *Nature* **517**(7533), 174–176 (2015)
- [75] Bernath, P., Dodangodage, R., Liévin, J.: S-type stars: LaO line list for the $B^2\Sigma^+-X^2\Sigma^+$ band system. *The Astrophysical Journal* **933**(1), 99 (2022)
- [76] Bernath, P., Dodangodage, R., Liévin, J.: S-type stars: Line list for the $A^2\Pi-X^2\Sigma^+$ band system of LaO. *The Astrophysical Journal* **953**(2) (2023)
- [77] Bernard, A., Sibai, A.: The spectrum of lanthanum oxide: A reanalysis of the rotational data. *Zeitschrift für Naturforschung A* **35**(12), 1313–1316 (1980)
- [78] Bacis, R., Collomb, R., Bessis, N.: Hyperfine structure of the $B^2\Sigma^+-X^2\Sigma^+$ transition of the LaO molecule. *Physical Review A* **8**(5), 2255 (1973)
- [79] Bernard, A., Taher, F., Topouzkhaniyan, A., Wannous, G.: Laser-excited fluorescence spectra of lanthanum monoxide-The $B^2\Sigma^+-X^2\Sigma^+$ system. *Astronomy and Astrophysics Supplement Series* **139**(1), 163–166 (1999)
- [80] Bernard, A., Vergés, J.: The infrared $A^2\Pi-A^2\Delta$ transition of LaO. *Journal of Molecular Spectroscopy* **201**(1), 172–174 (2000)
- [81] Childs, W., Goodman, G., Goodman, L., Young, L.: High-precision laser and RF spectroscopy of the spin-rotation and HFS interactions in the $X^2\Sigma^+$ and $B^2\Sigma^+$ states of LaO. *Journal of Molecular Spectroscopy* **119**(1), 166–180 (1986)
- [82] Törring, T., Zimmermann, K., Hoeft, J.: The microwave rotational spectrum of $X^2\Sigma^+$ LaO. *Chemical Physics Letters* **151**(6), 520–525 (1988)
- [83] Steimle, T., Virgo, W.: The permanent electric dipole moments for the $A^2\Pi$ and $B^2\Sigma^+$ states and the hyperfine interactions in the $A^2\Pi$ state of lanthanum monoxide, LaO. *The Journal of Chemical Physics* **116**(14), 6012–6020 (2002)
- [84] Suenram, R., Lovas, F., Fraser, G., Matsumura, K.: Pulsed-nozzle fourier-transform microwave spectroscopy of laser-vaporized metal oxides: Rotational spectra and electric dipole moments of YO, LaO, ZrO, and HfO. *The Journal of Chemical Physics* **92**(8), 4724–4733 (1990)

- [85] Bernard, A., Bacis, R., Luc, P.: Fourier transform spectroscopy: Extensive analysis of the $A^2\Pi-X^2\Sigma^+$ and $B^2\Sigma^+-X^2\Sigma^+$ systems of yttrium oxide. *Astrophysical Journal* **227**, 338–348 (1979)
- [86] Bernard, A., Gravina, R.: Further analysis of the $B^2\Sigma^+-X^2\Sigma^+$ system of the YO molecule. *Astrophysical Journal* **44**, 223–239 (1980)
- [87] Bernard, A., Gravina, R.: The emission spectrum of yttrium monoxide-new rotational and vibrational results on the $A^2\Pi-X^2\Sigma^+$ system. *The Astrophysical Journal Supplement Series* **52**, 443–450 (1983)
- [88] Yurchenko, S.N., Brady, R.P., Tennyson, J., Smirnov, A.N., Vasilyev, O.A., Solomonik, V.G.: ExoMol line lists–LIII: empirical rovibronic spectra of yttrium oxide. *Monthly Notices of the Royal Astronomical Society* **527**(3), 4899–4912 (2024)
- [89] Leung, J.-H., Ma, T., Cheung, A.: Cavity ring down absorption spectroscopy of the $B^2\Sigma^+-X^2\Sigma^+$ transition of YO. *Journal of Molecular Spectroscopy* **229**(1), 108–114 (2005)
- [90] Western, C.M.: PGOPHER: A program for simulating rotational, vibrational and electronic spectra. *Journal of Quantitative Spectroscopy and Radiative Transfer* **186**, 221–242 (2017)
- [91] Jevons, W.: The band spectrum of lanthanum monoxide. *Proceedings of the Physical Society* **41**(1), 520 (1928)
- [92] Weltner Jr, W., McLeod Jr, D., Kasai, P.: ESR and optical spectroscopy of ScO, YO, and LaO in neon and argon matrices; establishment of their ground electronic states. *The Journal of Chemical Physics* **46**(8), 3172–3184 (1967)
- [93] Knowles, P.J., Werner, H.-J.: An efficient method for the evaluation of coupling coefficients in configuration interaction calculations. *Chemical physics letters* **145**(6), 514–522 (1988)
- [94] Werner, H.-J., Knowles, P.J.: An efficient internally contracted multiconfiguration–reference configuration interaction method. *The Journal of chemical physics* **89**(9), 5803–5814 (1988)
- [95] Werner, H.-J., Knowles, P.J., Knizia, G., Manby, F.R., Schütz, M.: Molpro: a general-purpose quantum chemistry program package. *Wiley Interdisciplinary Reviews: Computational Molecular Science* **2**(2), 242–253 (2012)

- [96] Werner, H.-J., Knowles, P.J., Knizia, G., Manby, F.R., Schütz, M., et al.: MOLPRO, version 2019.2, a package of ab initio programs. see <https://www.molpro.net> (2019)
- [97] Frosch, R.A., Foley, H.: Magnetic hyperfine structure in diatomic molecules. *Physical Review* **88**(6), 1337 (1952)
- [98] Hirota, E., Brown, J.M., Hougen, J., Shida, T., Hirota, N.: Symbols for fine and hyperfine structure parameters (IUPAC Recommendations 1994). *Pure and applied chemistry* **66**(3), 571–576 (1994)
- [99] Brown, J., Merer, A.: Lambda-type doubling parameters for molecules in Π electronic states of triplet and higher multiplicity. *Journal of Molecular Spectroscopy* **74**(3), 488–494 (1979)
- [100] Le Roy, R.J.: RKR1: A computer program implementing the first-order RKR method for determining diatomic molecule potential energy functions. *Journal of Quantitative Spectroscopy and Radiative Transfer* **186**, 158–166 (2017)
- [101] Le Roy, R.J.: LEVEL: A computer program for solving the radial Schrödinger equation for bound and quasibound levels. *Journal of Quantitative Spectroscopy and Radiative Transfer* **186**, 167–178 (2017)
- [102] Dagdigian, P.J., Cruse, H.W., Zare, R.N.: Radiative lifetimes of the alkaline earth monohalides. *The Journal of Chemical Physics* **60**(6), 2330–2339 (1974)
- [103] Liu, K., Parson, J.: Laser fluorescence detection of nascent product state distributions in reactions of Sc and Y with O₂, NO, and SO₂. *The Journal of Chemical Physics* **67**(5), 1814–1828 (1977)
- [104] Carette, P., Bencheikh, M.: Measurements of the radiative lifetimes of the $v=0$ levels of the B²Σ⁺ and C²Π States of LaO. *Journal of Molecular Spectroscopy* **163**(1), 309–312 (1994)
- [105] Schoonveld, L., Sundaram, S.: Electronic transitions of LaO molecule. *The Astrophysical Journal Supplement Series* **27**, 307 (1974)
- [106] Ying, T., Gang, J.: Ab initio study on transition properties of LaO molecular. *Journal of Hebei University (Natural Science Edition)* **40**(2), 125 (2020)
- [107] Bernath, P.F.: Molecular astronomy of cool stars and sub-stellar objects. *International Reviews in Physical Chemistry* **28**(4), 681–709 (2009)

- [108] Zhang, D., Zhang, Q., Zhu, B., Gu, J., Suo, B., Chen, Y., Zhao, D.: High-resolution electronic spectra of yttrium oxide (YO): The $D^2\Sigma^+ - X^2\Sigma^+$ transition. *The Journal of chemical physics* **146**(11) (2017)
- [109] Murty, P.: Pi gruis: Molecular identifications and spectral classification. *Astrophysics and space science* **94**, 295–305 (1983)
- [110] Kamiński, T., Schmidt, M., Tylanda, R., Konacki, M., Gromadzki, M.: Keck/HIRES spectroscopy of V838 monocerotis in October 2005. *The Astrophysical Journal Supplement Series* **182**(1), 33 (2009)
- [111] Tylanda, R., Górny, S., Kamiński, T., Schmidt, M.: VLT/UVES spectroscopy of V4332 Sagittarii in 2005: The best view on a decade-old stellar-merger remnant. *Astronomy & Astrophysics* **578**, 75 (2015)
- [112] Steimle, T.C., Al-Ramadin, Y.: A microwave-optical double-resonance study of gas-phase yttrium monoxide. *Chemical physics letters* **130**(1-2), 76–78 (1986)
- [113] Hoeft, J., Törring, T.: The microwave rotational spectrum of $X^2\Sigma^+$ YO. *Chemical physics letters* **215**(4), 367–370 (1993)
- [114] Johnson, L., Johnson, R.: The band spectrum of yttrium oxide (YO). With a note on the ScO and LaO Systems. *Proceedings of the Royal Society of London. Series A, Containing Papers of a Mathematical and Physical Character* **133**(821), 207–219 (1931)
- [115] Uhler, U., Akerlind, L.: Rotational analysis of the blue-green and orange systems of yttrium oxide. *Arkiv Fysik* **Vol: 19** (1961)
- [116] Shin, J., Nicholls, R.: A high resolution study of the shock excited spectrum of yttrium oxide. *Spectroscopy Letters* **10**(11), 923–935 (1977)
- [117] Fried, D., Kushida, T., Reck, G.P., Rothe, E.W.: The yttrium oxide chemiluminescence from the 308 nm excimer laser ablation of $YBa_2Cu_3O_{7-x}$, Y_2O_3 , and YCl_3 . *Journal of Applied Physics* **73**(11), 7810–7817 (1993)
- [118] Mukund, S., Nakhate, S.: Rotational and deperturbation analysis of the interacting $A^2\Pi_{1/2}$, $v=11 \sim B^2\Sigma^+$, $v=6$ states of yttrium monoxide (YO) molecule. *Journal of Quantitative Spectroscopy and Radiative Transfer* **296**, 108452 (2023)

- [119] Smirnov, A.N., Solomonik, V.G., Yurchenko, S.N., Tennyson, J.: Spectroscopy of YO from first principles. *Physical Chemistry Chemical Physics* **21**(41), 22794–22810 (2019)
- [120] Green, D.W.: Rotational Analysis of the $C^2\Pi-X^2\Sigma^+$ Electronic Transition of LaO. *Canadian Journal of Physics* **49**(20), 2552–2564 (1971)
- [121] Nixon, C.A., Jennings, D.E., Bezdard, B., Vinatier, S., Teanby, N.A., Sung, K., Ansty, T.M., Irwin, P.G., Gorius, N., Cottini, V., *et al.*: Detection of propene in Titan's stratosphere. *The Astrophysical Journal Letters* **776**(1), 14 (2013)
- [122] Lide, D.R., Mann, D.: Microwave spectra of molecules exhibiting internal rotation. I. Propylene. *The Journal of Chemical Physics* **27**(4), 868–873 (1957)
- [123] Groner, P.: Effective rotational Hamiltonian for molecules with internal rotors: Principles, theory, applications and experiences. *Journal of Molecular Spectroscopy* **278**, 52–67 (2012)

APPENDIX A

RKR AND LEVEL INPUT FILES FOR LaO TRANSITIONS

Listing A.1. RKR input file for the $X^2\Sigma^+$ state

```

57 139 8 16 +0 0 0          % IAN1 IMN1 IAN2 IMN2 CHARGE NDEGv NDEBv
'LaO - Potential energy function and constants for X state [VEXT = 0]'
3                            % LMAXGv
816.9969 -2.1243 -3.48D-3    %Y10 Y20 Y30: calculated from PGOPHER fit
2                            % LMAXBv
0.35250046D0 -0.142365D-2 -2.972D-6 %Y01 Y11 Y21: From Bernard et al.
0 1 0.d0                    % Kaiser NSV VEXT
-0.4d0 0.1d0 4.6d0         %(1) V1 DV V2

```

Listing A.2. RKR input file for the $B^2\Sigma^+$ state

```

57 139 8 16 +0 0 0          % IAN1 IMN1 IAN2 IMN2 CHARGE NDEGv NDEBv
'LaO - Potential energy function and constants for B state [VEXT = 0]'
3                            % LMAXGv
734.2344 -1.9830D0 -4.09D-3  %Y10 Y20 Y30: calculated from PGOPHER fit
2                            % LMAXBv
0.3413261 -1.5319D-3 -1.77D-6 %Y01 Y11 Y21 Y31: calculated from PGOPHER fit
0 1 0.d0                    % Kaiser NSV VEXT
-0.4d0 0.1d0 4.6d0         %(1) V1 DV V2

```

Listing A.3. LEVEL input file for the $B^2\Sigma^+ - ^2\Sigma^+$ transition.

```

57 139 8 16 0 2            % IAN1 IMN1 IAN2 IMN2 CHARGE NUMPOT
'LaO B-X from RKR potentials with transition dipole moments (interpolated)'
0.0015 0.8 15.0 1.d-4     % RH RMIN RMAX EPS
99 0 0 65370.09535d0      % NTP LPPOT IOMEG VLIM
10 1 1 1 0.0D+0          % NUSE IR2 ILR NCN CNN
1.D0 1.D0 0.0d0          % RFACT EFACT VSHIFT & X-state turn. pnts.

1.6396000000000000 6505.78695212213
1.6464000000000000 5967.85526120584

```

1.65320000000000	5461.49389397055
1.66000000000000	4984.85004019116
1.66680000000000	4536.17962801873
1.67364766904215	4110.96952152000
1.67497601776893	4031.44200000000
1.67632098853836	3951.87094848000
1.67768309829561	3872.25638784000
1.67906289115588	3792.59833896000
1.68046094044261	3712.89682272000
1.68187785092637	3633.15186000000
1.68331426128916	3553.36347168000
1.68477084684259	3473.53167864000
1.68624832253247	3393.65650176000
1.68774744626775	3313.73796192000
1.68926902261744	3233.77608000000
1.69081390692670	3153.77087688000
1.69238300991147	3073.72237344000
1.69397730280155	2993.63059056000
1.69559782311424	2913.49554912000
1.69724568115572	2833.31727000000
1.69892206736540	2753.09577408000
1.70062826064085	2672.83108224000
1.70236563780815	2592.52321536000
1.70413568443630	2512.17219432000
1.70594000723647	2431.77804000000
1.70778034833935	2351.34077328000
1.70965860181047	2270.86041504000
1.71157683284766	2190.33698616000
1.71353730021283	2109.77050752000
1.71554248259005	2029.16100000000
1.71759510974379	1948.50848448000
1.71969819959074	1867.81298184000
1.72185510261756	1787.07451296000
1.72406955550547	1706.29309872000

1.72634574640710	1625.46876000000
1.72868839512760	1544.60151768000
1.73110285259206	1463.69139264000
1.73359522559074	1382.73840576000
1.73617253512549	1301.74257792000
1.73884292012748	1220.70393000000
1.74161590352296	1139.62248288000
1.74450274568323	1058.49825744000
1.74751692312083	977.33127456000
1.75067479135691	896.12155512000
1.75399652674741	814.86912000000
1.75750750574127	733.57399008000
1.76124039887786	652.23618624000
1.76523849212923	570.85572936000
1.76956124916133	489.43264032000
1.77429429643224	407.96694000000
1.77956908076329	326.45864928000
1.78560692422095	244.90778904000
1.79283946692507	163.31438016000
1.80238133483583	81.67844352000
1.82597098502407	0.00000000000
1.85036767705890	81.67844352000
1.86071712846108	163.31438016000
1.86875779704300	244.90778904000
1.87560430950783	326.45864928000
1.88168830671986	407.96694000000
1.88723111149147	489.43264032000
1.89236417139135	570.85572936000
1.89717311362641	652.23618624000
1.90171740261289	733.57399008000
1.90604032507459	814.86912000000
1.91017455230412	896.12155512000
1.91414546150515	977.33127456000
1.91797322978980	1058.49825744000

1.92167421343691	1139.62248288000
1.92526188971822	1220.70393000000
1.92874751976568	1301.74257792000
1.93214062726771	1382.73840576000
1.93544935191918	1463.69139264000
1.93868071548710	1544.60151768000
1.94184082552844	1625.46876000000
1.94493503373650	1706.29309872000
1.94796806068616	1787.07451296000
1.95094409530132	1867.81298184000
1.95386687503598	1948.50848448000
1.95673975115112	2029.16100000000
1.95956574233929	2109.77050752000
1.96234757914236	2190.33698616000
1.96508774102334	2270.86041504000
1.96778848752464	2351.34077328000
1.97045188462615	2431.77804000000
1.97307982717699	2512.17219432000
1.97567405809305	2592.52321536000
1.97823618487222	2672.83108224000
1.98076769387183	2753.09577408000
1.98326996270784	2833.31727000000
1.98574427106930	2913.49554912000
1.98819181018866	2993.63059056000
1.99061369116676	3073.72237344000
1.99301095231715	3153.77087688000
1.99538456566744	3233.77608000000
1.99773544273305	3313.73796192000
2.00006443966016	3393.65650176000

99 0 0 47532.70155	% NTP2 LPPOT2 IOMEG2 VLIM2
10 1 1 1 0.D0	% NUSE2 IR22 ILR2 NCN2 CNN2
1.D0 1.D0 17837.3938D0	% RFACT EFACT VSHIFT2 & B state

1.66050000000000	5862.15638722981
1.66760000000000	5374.42134091540
1.67470000000000	4915.76102020099
1.68180000000000	4484.44223065018
1.68890000000000	4078.83509653007
1.69609472112254	3692.47506741000
1.69747459986875	3621.08575000000
1.69887196568695	3549.65554559000
1.70028736377787	3478.18447872000
1.70172136799668	3406.67257393000
1.70317458300260	3335.11985576000
1.70464764662023	3263.52634875000
1.70614123243874	3191.89207744000
1.70765605267865	3120.21706637000
1.70919286136078	3048.50134008000
1.71075245781734	2976.74492311000
1.71233569059111	2904.94784000000
1.71394346177667	2833.11011529000
1.71557673186650	2761.23177352000
1.71723652517544	2689.31283923000
1.71892393593029	2617.35333696000
1.72064013512696	2545.35329125000
1.72238637827678	2473.31272664000
1.72416401418706	2401.23166767000
1.72597449494979	2329.11013888000
1.72781938734801	2256.94816481000
1.72970038593380	2184.74577000000
1.73161932808725	2112.50297899000
1.73357821143595	2040.21981632000
1.73557921410350	1967.89630653000
1.73762471836956	1895.53247416000
1.73971733847121	1823.12834375000
1.74185995346744	1750.68393984000
1.74405574634124	1678.19928697000

1.74630825084989	1605.67440968000
1.74862140808673	1533.10933251000
1.75099963533347	1460.50408000000
1.75344791063344	1387.85867669000
1.75597187770800	1315.17314712000
1.75857797753590	1242.44751583000
1.76127361537523	1169.68180736000
1.76406737564321	1096.87604625000
1.76696930256114	1024.03025704000
1.76999127297302	951.14446427000
1.77314750127551	878.21869248000
1.77645523861438	805.25296621000
1.77993576633194	732.24731000000
1.78361585082696	659.20174839000
1.78752995233868	586.11630592000
1.79172372836734	512.99100713000
1.79625990088299	439.82587656000
1.80122878888857	366.62093875000
1.80676904385523	293.37621824000
1.81311412039490	220.09173957000
1.82071932415271	146.76752728000
1.83076040278308	73.40360591000
1.85561966797726	0.00000000000
1.88137946994976	73.40360591000
1.89232163335292	146.76752728000
1.90082847074324	220.09173957000
1.90807573064216	293.37621824000
1.91451871956359	366.62093875000
1.92039089299003	439.82587656000
1.92583090326500	512.99100713000
1.93092907026558	586.11630592000
1.93574811683779	659.20174839000
1.94033370135960	732.24731000000
1.94472028494984	805.25296621000

1.94893463488863	878.21869248000
1.95299803340149	951.14446427000
1.95692773251923	1024.03025704000
1.96073794752536	1096.87604625000
1.96444055615257	1169.68180736000
1.96804560351268	1242.44751583000
1.97156167491533	1315.17314712000
1.97499617651284	1387.85867669000
1.97835555018005	1460.50408000000
1.98164544053629	1533.10933251000
1.98487082652474	1605.67440968000
1.98803612632882	1678.19928697000
1.99114528194546	1750.68393984000
1.99420182803744	1823.12834375000
1.99720894849514	1895.53247416000
2.00016952328681	1967.89630653000
2.00308616756075	2040.21981632000
2.00596126450970	2112.50297899000
2.00879699317231	2184.74577000000
2.01159535209309	2256.94816481000
2.01435817957103	2329.11013888000
2.01708717107901	2401.23166767000
2.01978389432284	2473.31272664000
2.02244980231922	2545.35329125000
2.02508624480210	2617.35333696000
2.02769447821145	2689.31283923000
2.03027567447378	2761.23177352000
2.03283092874843	2833.11011529000
2.03536126628479	2904.94784000000
2.03786764851187	2976.74492311000
2.04035097846279	3048.50134008000

-5 1 0 4 0 1 -1 0 % NLEV1 AUTO1 LCDC LXPCT NJM JDJR IWR LPRWF
0 0 % IV(1) IJ(1)

1	10	1.D0	% MORDR	IRFN	DREF
1592	0.2		% NRFN	RFLIM	
10	1	1	0.D0	% NUSEF	ILRF NCNF CNNF
1.d0	1.d0		% RFACTF	MFACTF	

1.60009 5.870559186
1.60046 5.86995636
1.60107 5.868959692
1.60185 5.867706032
1.60268 5.866366155
1.60345 5.865120776
1.60406 5.86413635
1.60443 5.86354334
1.60461 5.863255783
1.60498 5.862663918
1.6056 5.861684781
1.60637 5.860452115
1.6072 5.85913336
1.60797 5.857906376
1.60859 5.856935637
1.60896 5.856350506
1.60914 5.85606667
1.60951 5.855482258
1.61012 5.854514839
1.61089 5.853295833
1.61172 5.851990333
1.61249 5.850774409
1.61311 5.849811545
1.61348 5.849230785
1.61366 5.848948967
1.61403 5.848368499
1.61464 5.847406985
1.61541 5.846194305
1.61624 5.844894195

1.61702 5.843681996
1.61763 5.842721194
1.618 5.842141296
1.61818 5.841859794
1.61855 5.841279762
1.61916 5.84031834
1.61994 5.839104651
1.62077 5.837802064
1.62154 5.836586256
1.62215 5.835621702
1.62252 5.83503916
1.6227 5.83475627
1.62307 5.834173167
1.62369 5.833206022
1.62446 5.83198399
1.62529 5.830671061
1.62606 5.82944431
1.62668 5.828470191
1.62705 5.827881495
1.62723 5.827595515
1.6276 5.827005832
1.62821 5.826027153
1.62898 5.824789442
1.62981 5.823458305
1.63059 5.822213276
1.6312 5.821223779
1.63157 5.820625421
1.63175 5.820334648
1.63212 5.819734878
1.63273 5.81873885
1.6335 5.817478126
1.63433 5.816120916
1.63511 5.814850274
1.63572 5.813839586

1.63609 5.813228059
1.63627 5.81293079
1.63664 5.812317423
1.63725 5.811298235
1.63803 5.810007164
1.63886 5.808616014
1.63963 5.807312424
1.64024 5.806274732
1.64061 5.805646527
1.64079 5.80534106
1.64116 5.804710589
1.64178 5.803662427
1.64255 5.802333673
1.64338 5.800900719
1.64415 5.799556847
1.64477 5.798486337
1.64514 5.797837946
1.64532 5.797522578
1.64569 5.796871495
1.6463 5.795788545
1.64707 5.794414774
1.6479 5.792932149
1.64868 5.79154066
1.64929 5.79043152
1.64966 5.789759436
1.64984 5.789432463
1.65021 5.788757261
1.65082 5.787633774
1.6516 5.786208067
1.65242 5.784669111
1.6532 5.783224852
1.65381 5.782073945
1.65418 5.781376754
1.65436 5.781037636

1.65473 5.780337517
1.65534 5.779173075
1.65612 5.777696288
1.65695 5.776103292
1.65772 5.77460933
1.65833 5.773419502
1.6587 5.772699026
1.65888 5.772348659
1.65925 5.77162548
1.65987 5.77042316
1.66064 5.768899177
1.66147 5.767256305
1.66224 5.765716523
1.66286 5.764490853
1.66323 5.763748948
1.66341 5.763388235
1.66378 5.762643853
1.66439 5.761406733
1.66516 5.759839437
1.66599 5.758150854
1.66677 5.756569137
1.66738 5.755310701
1.66775 5.754549225
1.66793 5.754179068
1.6683 5.75341534
1.66891 5.752146498
1.66969 5.750539772
1.67052 5.748809643
1.67129 5.747189873
1.6719 5.74590175
1.67227 5.74512256
1.67245 5.74474386
1.67282 5.743962644
1.67343 5.742665158

1.67421 5.741022886
1.67504 5.739255375
1.67581 5.737601436
1.67642 5.736286703
1.67679 5.735491657
1.67697 5.735105315
1.67734 5.734308468
1.67796 5.732985416
1.67873 5.731311482
1.67956 5.729510754
1.68033 5.727826528
1.68095 5.726488264
1.68132 5.725679219
1.6815 5.725286137
1.68187 5.724475517
1.68248 5.723129976
1.68325 5.721428263
1.68408 5.719598482
1.68486 5.717887854
1.68547 5.716529136
1.68584 5.715707949
1.68602 5.715309029
1.68639 5.714486493
1.687 5.713121541
1.68778 5.711395932
1.68861 5.709541264
1.68938 5.707808117
1.68999 5.706432023
1.69036 5.705600552
1.69054 5.705196694
1.69091 5.7043641
1.69153 5.702982816
1.6923 5.701237194
1.69313 5.699361803

1.6939 5.69761002
1.69452 5.696219628
1.69489 5.69537973
1.69506 5.694971837
1.69543 5.694131042
1.69605 5.692736503
1.69682 5.690974752
1.69765 5.689082802
1.69842 5.687316267
1.69904 5.685914655
1.69941 5.685068188
1.69959 5.684657161
1.69996 5.683810022
1.70057 5.682405297
1.70134 5.680631206
1.70217 5.678726528
1.70295 5.676948471
1.70356 5.675537884
1.70393 5.674686041
1.70411 5.674272411
1.70448 5.673419913
1.70509 5.672006299
1.70587 5.670220968
1.7067 5.668304204
1.70747 5.666514849
1.70808 5.665095289
1.70845 5.664238022
1.70863 5.663821757
1.709 5.662963826
1.70962 5.661541195
1.71039 5.659744461
1.71122 5.65781544
1.71199 5.656014626
1.71261 5.654585963

1.71298 5.653723196
1.71316 5.653304258
1.71353 5.652440817
1.71414 5.651009041
1.71491 5.649200744
1.71574 5.647259292
1.71652 5.645446857
1.71713 5.644008965
1.7175 5.64314062
1.71768 5.642718972
1.71805 5.641849943
1.71866 5.640408895
1.71943 5.638588873
1.72026 5.636634817
1.72104 5.6348106
1.72165 5.633363351
1.72202 5.63248935
1.7222 5.632064955
1.72257 5.631190262
1.72318 5.629739812
1.72396 5.627907905
1.72479 5.625941071
1.72556 5.624104912
1.72617 5.622648177
1.72654 5.621768444
1.72672 5.621341264
1.72709 5.620460829
1.72771 5.619000851
1.72848 5.617156896
1.72931 5.615177112
1.73008 5.613328849
1.7307 5.611862501
1.73107 5.610976958
1.73125 5.610546956

1.73162 5.609660701
1.73223 5.608191067
1.733 5.606334904
1.73383 5.604341997
1.73461 5.602481467
1.73522 5.601005379
1.73559 5.600113949
1.73577 5.599681087
1.73614 5.598788936
1.73675 5.597309518
1.73752 5.595440985
1.73835 5.593434781
1.73913 5.591561825
1.73974 5.590075867
1.74011 5.589178473
1.74029 5.588742715
1.74066 5.58784459
1.74127 5.586355259
1.74205 5.584474195
1.74288 5.582454522
1.74365 5.580568978
1.74426 5.579073023
1.74463 5.578169588
1.74481 5.577730895
1.74518 5.57682672
1.7458 5.575327349
1.74657 5.573433593
1.7474 5.571400277
1.74817 5.569501983
1.74879 5.567995904
1.74916 5.56708635
1.74934 5.566644685
1.74971 5.565734383
1.75032 5.564224844

1.75109 5.562318245
1.75192 5.560271164
1.7527 5.558360067
1.75331 5.55684388
1.75368 5.555928248
1.75386 5.555483639
1.75423 5.554567289
1.75484 5.553047782
1.75562 5.551128707
1.75644 5.549068372
1.75722 5.547145033
1.75783 5.545619223
1.7582 5.544697819
1.75838 5.544250418
1.75875 5.543328333
1.75936 5.541799382
1.76014 5.53986849
1.76097 5.53779561
1.76174 5.535860689
1.76235 5.53432578
1.76272 5.533398919
1.7629 5.532948879
1.76327 5.532021376
1.76389 5.530483503
1.76466 5.528541456
1.76549 5.526456738
1.76626 5.524510895
1.76688 5.522967411
1.76725 5.522035409
1.76743 5.521582882
1.7678 5.520650277
1.76841 5.519104006
1.76918 5.517151464
1.77001 5.515055616

1.77079 5.513099512
1.7714 5.511547976
1.77177 5.510611149
1.77195 5.51015629
1.77232 5.509218898
1.77293 5.507664751
1.77371 5.505702374
1.77454 5.503596105
1.77531 5.501630401
1.77592 5.500071335
1.77629 5.499129999
1.77647 5.498672961
1.77684 5.497731098
1.77745 5.4961696
1.77823 5.494198049
1.77906 5.492082067
1.77983 5.490107422
1.78044 5.488541351
1.78081 5.487595821
1.78099 5.487136757
1.78136 5.486190739
1.78198 5.484622413
1.78275 5.482642347
1.78358 5.48051736
1.78435 5.478534435
1.78497 5.476961882
1.78534 5.476012475
1.78552 5.475551538
1.78589 5.474601681
1.7865 5.473027049
1.78727 5.47103913
1.7881 5.468905846
1.78888 5.466915301
1.78949 5.465336789

1.78986 5.464383821
1.79004 5.463921164
1.79041 5.462967784
1.79102 5.461387371
1.7918 5.459392259
1.79263 5.457251385
1.7934 5.455253881
1.79401 5.453669934
1.79438 5.452713719
1.79456 5.452249496
1.79493 5.451292909
1.79555 5.449707238
1.79632 5.447705592
1.79715 5.445557839
1.79792 5.443554036
1.79854 5.441965176
1.79891 5.441006031
1.79908 5.440540396
1.79945 5.439580916
1.80007 5.437990511
1.80084 5.435982989
1.80167 5.433829038
1.80244 5.431819536
1.80306 5.430226202
1.80343 5.429264372
1.80361 5.428797437
1.80398 5.427835284
1.80459 5.426240462
1.80536 5.424227381
1.80619 5.422067484
1.80697 5.420052452
1.80758 5.418454746
1.80795 5.417490281
1.80813 5.417022068

1.8085 5.416057286
1.80911 5.414458113
1.80989 5.412439556
1.81072 5.410273802
1.81149 5.408253323
1.8121 5.40665131
1.81247 5.405684251
1.81265 5.405214779
1.81302 5.404247407
1.81364 5.402643949
1.81441 5.400619999
1.81524 5.398448477
1.81601 5.396422634
1.81663 5.39481638
1.817 5.393846765
1.81718 5.393376055
1.81755 5.392406132
1.81816 5.390798456
1.81893 5.388769195
1.81976 5.386591993
1.82054 5.384560869
1.82115 5.38295044
1.82152 5.38197831
1.8217 5.381506379
1.82207 5.380533946
1.82268 5.378922117
1.82345 5.376887628
1.82428 5.374704836
1.82506 5.372668514
1.82567 5.371053975
1.82604 5.370079369
1.82622 5.369606238
1.82659 5.368631334
1.8272 5.367015417

1.82798 5.364975783
1.82881 5.36278749
1.82958 5.360746053
1.83019 5.35912747
1.83056 5.358150428
1.83074 5.357676115
1.83111 5.35669878
1.83173 5.355078841
1.8325 5.353034146
1.83333 5.35084044
1.8341 5.348793971
1.83472 5.347171409
1.83509 5.34619197
1.83527 5.345716496
1.83564 5.344736769
1.83625 5.343112874
1.83702 5.3410632
1.83785 5.338864171
1.83863 5.336812752
1.83924 5.335186277
1.83961 5.334204482
1.83979 5.333727865
1.84016 5.332745785
1.84077 5.331118
1.84154 5.32906343
1.84237 5.326859166
1.84315 5.324802881
1.84376 5.32317256
1.84413 5.322188447
1.84431 5.321710706
1.84468 5.320726314
1.84529 5.319094704
1.84607 5.317035321
1.8469 5.314825912

1.84767 5.312764843
1.84828 5.31113074
1.84865 5.31014435
1.84883 5.309665505
1.8492 5.308678841
1.84982 5.307043471
1.85059 5.304979358
1.85142 5.302764891
1.85219 5.300699118
1.85281 5.299061296
1.85318 5.298072664
1.85336 5.297592731
1.85373 5.296603828
1.85434 5.294964754
1.85511 5.292895973
1.85594 5.290676509
1.85672 5.288606085
1.85733 5.286964581
1.8577 5.28597373
1.85788 5.285492721
1.85825 5.284501601
1.85886 5.282858858
1.85964 5.280785456
1.86047 5.278561043
1.86124 5.276486013
1.86185 5.274840864
1.86222 5.273847815
1.8624 5.27336574
1.86277 5.272372426
1.86338 5.27072605
1.86416 5.268648071
1.86499 5.266418759
1.86576 5.264339168
1.86637 5.26269041

1.86674 5.261695186
1.86692 5.261212055
1.86729 5.260216568
1.86791 5.258566595
1.86868 5.256484085
1.86951 5.254249922
1.87028 5.252165816
1.8709 5.250513485
1.87127 5.249516106
1.87145 5.249031931
1.87182 5.248034293
1.87243 5.246380759
1.8732 5.244293762
1.87403 5.242054798
1.87481 5.239966222
1.87542 5.238310354
1.87579 5.237310843
1.87597 5.236825634
1.87634 5.235825866
1.87695 5.234168807
1.87773 5.23207737
1.87856 5.229833652
1.87933 5.227740651
1.87994 5.226081282
1.88031 5.225079661
1.88049 5.224593428
1.88086 5.223591552
1.88147 5.221931005
1.88225 5.219835173
1.88308 5.21758675
1.88385 5.215489371
1.88446 5.213826536
1.88483 5.212822827
1.88501 5.21233558

1.88538 5.211331618
1.886 5.209667618
1.88677 5.207567436
1.8876 5.205314357
1.88837 5.203212645
1.88899 5.201546381
1.88936 5.200540605
1.88954 5.200052356
1.88991 5.199046329
1.89052 5.197378912
1.89129 5.195274426
1.89212 5.19301674
1.8929 5.190910739
1.89351 5.189241083
1.89388 5.188233261
1.89406 5.18774402
1.89443 5.186735951
1.89504 5.185065153
1.89582 5.182956408
1.89665 5.180694163
1.89742 5.17858392
1.89803 5.176910906
1.8984 5.175901061
1.89858 5.175410838
1.89895 5.174400748
1.89957 5.172726605
1.90034 5.170613648
1.90117 5.168346902
1.90194 5.166232496
1.90256 5.164556216
1.90293 5.163544419
1.9031 5.163053254
1.90347 5.162041236
1.90409 5.160363941

1.90486 5.158247091
1.90569 5.155976287
1.90646 5.153858203
1.90708 5.152179084
1.90745 5.151165604
1.90763 5.150673631
1.908 5.149659966
1.90861 5.147979994
1.90938 5.14585986
1.91021 5.143585649
1.91099 5.141464497
1.9116 5.139783019
1.91197 5.138768148
1.91215 5.138275508
1.91252 5.137260487
1.91313 5.13557832
1.91391 5.13345551
1.91474 5.131178545
1.91551 5.129054932
1.91612 5.127371578
1.91649 5.126355606
1.91667 5.125862441
1.91704 5.124846355
1.91766 5.123162475
1.91843 5.121037597
1.91926 5.11875853
1.92003 5.116633065
1.92065 5.114948317
1.92102 5.113931535
1.9212 5.113437986
1.92157 5.112421125
1.92218 5.110736014
1.92295 5.108609677
1.92378 5.10632916

1.92456 5.104202451
1.92517 5.102516791
1.92554 5.101499491
1.92572 5.101005698
1.92609 5.099988354
1.9267 5.098302494
1.92747 5.096175305
1.9283 5.093893991
1.92908 5.091766647
1.92969 5.090080557
1.93006 5.089063028
1.93024 5.088569133
1.93061 5.087551597
1.93122 5.085865471
1.932 5.083738038
1.93283 5.081456579
1.9336 5.079329207
1.93421 5.077643169
1.93458 5.076625704
1.93476 5.076131848
1.93513 5.07511441
1.93575 5.073428499
1.93652 5.071301432
1.93735 5.06902048
1.93812 5.066893688
1.93874 5.065208184
1.93911 5.064191073
1.93929 5.063697397
1.93966 5.062680349
1.94027 5.060995135
1.94104 5.058869041
1.94187 5.056589249
1.94265 5.054463646
1.94326 5.052779158

1.94363 5.051762692
1.94381 5.051269338
1.94418 5.050252969
1.94479 5.048568935
1.94557 5.046444423
1.94639 5.044166442
1.94717 5.042042636
1.94778 5.040359647
1.94815 5.039344116
1.94833 5.038851225
1.9487 5.037835827
1.94931 5.036153455
1.95009 5.034031132
1.95092 5.031755595
1.95169 5.029634087
1.9523 5.027952881
1.95267 5.026938395
1.95285 5.026445998
1.95322 5.025431591
1.95384 5.023750753
1.95461 5.021630128
1.95544 5.019356058
1.95621 5.01723558
1.95683 5.01555496
1.9572 5.014540727
1.95738 5.014048427
1.95775 5.013034162
1.95836 5.011353397
1.95913 5.009232571
1.95996 5.006957923
1.96074 5.004836568
1.96135 5.00315502
1.96172 5.002140128
1.9619 5.001647482

1.96227 5.000632448
1.96288 4.998950243
1.96366 4.996827308
1.96449 4.994550036
1.96526 4.992425896
1.96587 4.99074191
1.96624 4.989725447
1.96642 4.989232011
1.96679 4.988215295
1.9674 4.986530139
1.96818 4.984403188
1.96901 4.982121247
1.96978 4.979992414
1.97039 4.978304477
1.97076 4.977285531
1.97094 4.976790863
1.97131 4.975771553
1.97193 4.974081934
1.9727 4.971949059
1.97353 4.969660402
1.9743 4.96752497
1.97492 4.965831571
1.97529 4.964809229
1.97547 4.964312885
1.97584 4.963290069
1.97645 4.961594475
1.97722 4.959453769
1.97805 4.957156352
1.97883 4.955012412
1.97944 4.953312038
1.97981 4.952285388
1.97999 4.951786927
1.98036 4.950759691
1.98097 4.94905661

1.98175 4.946906166
1.98258 4.944597942
1.98335 4.942443588
1.98396 4.940734728
1.98433 4.939702857
1.98451 4.939201835
1.98488 4.938169268
1.9855 4.936457189
1.98627 4.934295099
1.9871 4.931974022
1.98787 4.929807346
1.98848 4.928088487
1.98885 4.927050484
1.98903 4.926546459
1.9894 4.925507648
1.99002 4.923785058
1.99079 4.921609414
1.99162 4.91927344
1.99239 4.917092534
1.99301 4.915362166
1.99338 4.914317118
1.99356 4.913809645
1.99393 4.912763679
1.99454 4.911029067
1.99531 4.908837962
1.99614 4.906485044
1.99692 4.904288
1.99753 4.902544611
1.9979 4.901491605
1.99808 4.900980243
1.99845 4.899926209
1.99906 4.898178063
1.99984 4.895969589
2.00067 4.893597711

2.00144 4.891382886
2.00205 4.88962552
2.00242 4.888564191
2.0026 4.888048832
2.00297 4.886986664
2.00359 4.88522542
2.00436 4.883001277
2.00519 4.880613919
2.00596 4.878385973
2.00658 4.876619108
2.00695 4.875552433
2.00712 4.875034583
2.00749 4.8739675
2.00811 4.872198749
2.00888 4.869966271
2.00971 4.867571385
2.01048 4.865337733
2.0111 4.863567246
2.01147 4.862498771
2.01165 4.861980152
2.01202 4.860911699
2.01263 4.859141318
2.0134 4.856907921
2.01423 4.854513457
2.01501 4.852281514
2.01562 4.850513282
2.01599 4.849446553
2.01617 4.848928886
2.01654 4.847862611
2.01715 4.846096477
2.01793 4.843869574
2.01876 4.841483486
2.01953 4.839260665
2.02014 4.837500565

2.02051 4.836439129
2.02069 4.835924136
2.02106 4.834863585
2.02168 4.833107574
2.02245 4.830894581
2.02328 4.828524818
2.02405 4.826318536
2.02467 4.824572444
2.02504 4.823519848
2.02522 4.823009249
2.02559 4.821957969
2.0262 4.820217958
2.02697 4.818026289
2.0278 4.815680805
2.02858 4.813498475
2.02919 4.811772269
2.02956 4.810732058
2.02974 4.810227576
2.03011 4.809189112
2.03072 4.807470978
2.03149 4.805308049
2.03232 4.802994794
2.0331 4.800843832
2.03371 4.799143388
2.03408 4.798119109
2.03426 4.797622465
2.03463 4.796600364
2.03524 4.794909983
2.03602 4.792783208
2.03685 4.790510135
2.03762 4.788397956
2.03823 4.78672915
2.0386 4.785724349
2.03878 4.785237264

2.03915 4.784235073
2.03977 4.782578323
2.04054 4.780495116
2.04137 4.778270176
2.04214 4.776204194
2.04276 4.774572904
2.04313 4.773591128
2.04331 4.773115324
2.04368 4.772136589
2.04429 4.770519345
2.04506 4.768487123
2.04589 4.766318267
2.04667 4.764305898
2.04728 4.762717999
2.04765 4.761762795
2.04783 4.761299993
2.0482 4.76034826
2.04881 4.7587764
2.04959 4.756802576
2.05041 4.75469773
2.05119 4.752745772
2.0518 4.751205548
2.05217 4.750278782
2.05235 4.749829648
2.05272 4.748905729
2.05333 4.747378657
2.05411 4.74545831
2.05494 4.743405953
2.05571 4.741497843
2.05632 4.739988858
2.05669 4.739079442
2.05687 4.738638323
2.05724 4.737730073
2.05786 4.736226479

2.05863 4.734331324
2.05946 4.732300488
2.06023 4.730407324
2.06085 4.728906674
2.06122 4.728000785
2.0614 4.72756097
2.06177 4.726654568
2.06238 4.725151545
2.06315 4.72325268
2.06398 4.721212373
2.06476 4.719305254
2.06537 4.717790032
2.06574 4.716873848
2.06592 4.716428627
2.06629 4.71551025
2.0669 4.713984893
2.06768 4.712053417
2.06851 4.709972644
2.06928 4.70802267
2.06989 4.706469971
2.07026 4.705529667
2.07044 4.705072332
2.07081 4.704128156
2.07142 4.702557559
2.0722 4.700564571
2.07303 4.69841234
2.0738 4.69639061
2.07441 4.694777527
2.07478 4.693799281
2.07496 4.693323122
2.07533 4.692339323
2.07595 4.69070058
2.07672 4.688617181
2.07755 4.686362497

2.07832 4.684240109
2.07894 4.682543738
2.07931 4.681513727
2.07949 4.681012034
2.07986 4.67997479
2.08047 4.678244995
2.08124 4.676042283
2.08207 4.673654152
2.08285 4.671402207
2.08346 4.669599641
2.08383 4.668504041
2.08401 4.667970105
2.08438 4.666865593
2.08499 4.665021841
2.08577 4.662670914
2.0866 4.660118344
2.08737 4.657707939
2.08798 4.655776273
2.08835 4.654601262
2.08853 4.654028372
2.0889 4.652842769
2.08952 4.650862154
2.09029 4.648334112
2.09112 4.645586109
2.09189 4.642988344
2.09251 4.640904672
2.09288 4.639636426
2.09305 4.639017874
2.09342 4.637737355
2.09404 4.635596972
2.09481 4.632862914
2.09564 4.629888484
2.09641 4.627074458
2.09703 4.624815874

2.0974 4.62344057
2.09758 4.622769646
2.09795 4.62138039
2.09856 4.619057332
2.09933 4.616088357
2.10016 4.61285651
2.10094 4.60979795
2.10155 4.607343774
2.10192 4.605850161
2.1021 4.605121826
2.10247 4.603614461
2.10308 4.601096736
2.10386 4.597885454
2.10469 4.594400109
2.10546 4.591112737
2.10607 4.588482544
2.10644 4.58688499
2.10662 4.586106823
2.10699 4.584498068
2.10761 4.581816114
2.10838 4.578404345
2.10921 4.57471234
2.10998 4.571240039
2.1106 4.56846861
2.11097 4.566788104
2.11115 4.565970293
2.11152 4.564281137
2.11213 4.561469734
2.1129 4.557901365
2.11373 4.55404976
2.1145 4.550436413
2.11512 4.547558529
2.11549 4.545816062
2.11567 4.544968794

2.11604 4.543220227
2.11665 4.540314157
2.11742 4.53663307
2.11825 4.532668927
2.11903 4.528958419
2.11964 4.526008861
2.12001 4.524225422
2.12019 4.523358885
2.12056 4.521571897
2.12117 4.518605939
2.12195 4.514856019
2.12278 4.5108264
2.12355 4.507062615
2.12416 4.504076163
2.12453 4.502272741
2.12471 4.501397124
2.12508 4.499592703
2.1257 4.49660164
2.12647 4.49282677
2.1273 4.488778737
2.12807 4.485005559
2.12869 4.482016995
2.12906 4.480214579
2.12924 4.479340069
2.12961 4.477539206
2.13022 4.474557817
2.13099 4.470801882
2.13182 4.466782496
2.1326 4.463043808
2.13321 4.460087913
2.13358 4.458307493
2.13376 4.457444279
2.13413 4.455667962
2.13474 4.452731029

2.13551 4.449037913
2.13634 4.445094235
2.13712 4.441433923
2.13773 4.438545476
2.1381 4.436808042
2.13828 4.435966311
2.13865 4.434235531
2.13926 4.431377834
2.14004 4.427791421
2.14087 4.423970513
2.14164 4.42043246
2.14225 4.417646244
2.14262 4.415972784
2.1428 4.415162725
2.14317 4.41349847
2.14379 4.41075479
2.14456 4.407318964
2.14539 4.403667889
2.14616 4.400295978
2.14678 4.397646773
2.14715 4.396058277
2.14733 4.395290078
2.1477 4.393713338
2.14831 4.391118457
2.14908 4.387877101
2.14991 4.384442919
2.15069 4.381280797
2.1513 4.378802004
2.15167 4.377317648
2.15185 4.376600265
2.15222 4.375128631
2.15283 4.372708628
2.15361 4.369687794
2.15443 4.366487768

2.15521 4.363539878
2.15582 4.361227693
2.15619 4.359842519
2.15637 4.359172908
2.15674 4.357798933
2.15735 4.3555385
2.15813 4.352714983
2.15896 4.349721582
2.15973 4.34696172
2.16034 4.344795375
2.16071 4.343496851
2.16089 4.342868928
2.16126 4.34158008
2.16188 4.339458448
2.16265 4.336806045
2.16348 4.333991166
2.16425 4.331393129
2.16487 4.329351856
2.16524 4.328127448
2.16542 4.32753513
2.16579 4.326318875
2.1664 4.324315277
2.16717 4.321807783
2.168 4.319143327
2.16878 4.31668091
2.16939 4.314743941
2.16976 4.313581116
2.16994 4.31301832
2.17031 4.311862124
2.17092 4.309955792
2.1717 4.307567004
2.17253 4.305024868
2.1733 4.302671867
2.17391 4.300818435

2.17428 4.299704659
2.17446 4.299165302
2.17483 4.298056633
2.17544 4.296226798
2.17622 4.293930512
2.17705 4.291482595
2.17782 4.289212808
2.17843 4.287422142
2.1788 4.286344884
2.17898 4.285822881
2.17935 4.284749206
2.17997 4.282975101
2.18074 4.280745112
2.18157 4.278363313
2.18234 4.276150535
2.18296 4.274401869
2.18333 4.273348594
2.18351 4.272837863
2.18388 4.271786649
2.18449 4.270047505
2.18526 4.26785761
2.18609 4.265513828
2.18687 4.263331855
2.18748 4.261604421
2.18785 4.260562596
2.18803 4.260057053
2.1884 4.259015766
2.18901 4.257290815
2.18979 4.255114811
2.19062 4.252780944
2.19139 4.250603573
2.192 4.248876602
2.19237 4.247833694
2.19255 4.247327256

2.19292 4.246283363
2.19354 4.244551837
2.19431 4.24236352
2.19514 4.240011467
2.19591 4.237812494
2.19653 4.236065218
2.1969 4.235008694
2.19707 4.234495278
2.19744 4.233436246
2.19806 4.231677376
2.19883 4.229450541
2.19966 4.227052202
2.20043 4.224805452
2.20105 4.223017475
2.20142 4.221935397
2.2016 4.221409347
2.20197 4.220323879
2.20258 4.218520241
2.20335 4.216235866
2.20418 4.213775541
2.20496 4.211471733
2.20557 4.20963937
2.20594 4.208530868
2.20612 4.207992091
2.20649 4.206880605
2.2071 4.205034453
2.20788 4.202697506
2.20871 4.200182127
2.20948 4.197828217
2.21009 4.195956993
2.21046 4.194825402
2.21064 4.194275515
2.21101 4.193141345
2.21163 4.191258204

2.2124 4.188875655
2.21323 4.186312697
2.214 4.183915657
2.21462 4.182011096
2.21499 4.180859749
2.21517 4.180300371
2.21554 4.17914685
2.21615 4.177232245
2.21692 4.174811065
2.21775 4.172208004
2.21853 4.169774803
2.21914 4.16784243
2.21951 4.166674661
2.21969 4.166107412
2.22006 4.164937874
2.22067 4.162997329
2.22144 4.160544488
2.22227 4.157908799
2.22305 4.155446409
2.22366 4.153491748
2.22403 4.152310892
2.22421 4.151737388
2.22458 4.150555168
2.22519 4.148594207
2.22597 4.146116677
2.2268 4.143455835
2.22757 4.140971225
2.22818 4.138999802
2.22855 4.137809191
2.22873 4.137231051
2.2291 4.136039483
2.22972 4.134063632
2.23049 4.131568382
2.23132 4.128889862

2.23209 4.126390005
2.23271 4.124407343
2.23308 4.123210312
2.23326 4.122629155
2.23363 4.121431571
2.23424 4.119446354
2.23501 4.116940355
2.23584 4.114251634
2.23662 4.111743498
2.23723 4.109755123
2.2376 4.108555007
2.23778 4.107972449
2.23815 4.106772186
2.23876 4.104783127
2.23953 4.10227335
2.24036 4.099581901
2.24114 4.097072458
2.24175 4.095083894
2.24212 4.093884026
2.2423 4.093301687
2.24267 4.092102077
2.24328 4.090114701
2.24406 4.087608117
2.24489 4.084921417
2.24566 4.082417637
2.24627 4.080434408
2.24664 4.079238122
2.24682 4.078657621
2.24719 4.077461998
2.24781 4.07548183
2.24858 4.072985408
2.24941 4.070310932
2.25018 4.067819785
2.2508 4.06584737

2.25117 4.064657901
2.25135 4.064080777
2.25172 4.062892234
2.25233 4.060924101
2.2531 4.058443226
2.25393 4.055785601
2.25471 4.053310064
2.25532 4.05134982
2.25569 4.050167604
2.25587 4.049593976
2.25624 4.048412584
2.25685 4.046456147
2.25763 4.043989759
2.25846 4.041347334
2.25923 4.038885657
2.25984 4.036936183
2.26021 4.035760375
2.26039 4.035189832
2.26076 4.034014745
2.26137 4.032068603
2.26215 4.029614934
2.26298 4.026985812
2.26375 4.024536227
2.26436 4.022596123
2.26473 4.021425877
2.26491 4.020858008
2.26528 4.01968838
2.2659 4.017751133
2.26667 4.015308415
2.2675 4.012690701
2.26827 4.01025144
2.26889 4.008319303
2.26926 4.007153773
2.26944 4.006588169

2.26981 4.005423155
2.27042 4.0034934
2.27119 4.001059864
2.27202 3.998451662
2.2728 3.996020957
2.27341 3.994095386
2.27378 3.992933727
2.27396 3.992369977
2.27433 3.991208731
2.27494 3.989285067
2.27572 3.986858946
2.27655 3.98425836
2.27732 3.981834443
2.27793 3.979914037
2.2783 3.978755403
2.27848 3.978193096
2.27885 3.977034772
2.27946 3.975115799
2.28024 3.972695325
2.28107 3.970100458
2.28184 3.967681561
2.28245 3.965764919
2.28282 3.964608464
2.283 3.96404719
2.28337 3.962890943
2.28399 3.960975259
2.28476 3.958558663
2.28559 3.955967619
2.28636 3.953551974
2.28698 3.951637695
2.28735 3.950482574
2.28753 3.949921922
2.2879 3.948766906
2.28851 3.94685311

2.28928 3.944438625
2.29011 3.941849508
2.29089 3.939435347
2.2915 3.937522029
2.29187 3.936367396
2.29205 3.935806957
2.29242 3.934652326
2.29303 3.932739015
2.29381 3.930324873
2.29464 3.927735788
2.29541 3.925321342
2.29602 3.923407584
2.29639 3.922252594
2.29657 3.921691956
2.29694 3.920536865
2.29756 3.91862264
2.29833 3.916207072
2.29916 3.913616122
2.29993 3.911199624
2.30055 3.909284028
2.30092 3.908127849
2.30109 3.907566614
2.30146 3.906410259
2.30208 3.90449385
2.30285 3.902075413
2.30368 3.89948131
2.30445 3.89706187
2.30507 3.89514398
2.30544 3.893986437
2.30562 3.893424545
2.30599 3.892266849
2.3066 3.890348252
2.30737 3.887927115
2.3082 3.885330192

2.30898 3.882908192
2.30959 3.880988321
2.30996 3.879829603
2.31014 3.879267147
2.31051 3.8781083
2.31112 3.876187828
2.31119 3.873764387
2.31273 3.871165068
2.3135 3.868740905
2.31411 3.866819367
2.31448 3.865659664
2.31466 3.865096735
2.31503 3.863936925
2.31565 3.862014894
2.31642 3.859589544
2.31725 3.856988255
2.31802 3.854562324
2.31864 3.852639433
2.31901 3.851478934
2.31919 3.850915625
2.31956 3.849755042
2.32017 3.847831764
2.32094 3.845404902
2.32177 3.842802066
2.32255 3.840374764
2.32316 3.838450834
2.32353 3.837289728
2.32371 3.836726131
2.32408 3.835564964
2.32469 3.833640754
2.32546 3.831212776
2.32629 3.828608819
2.32707 3.826180541
2.32768 3.824255886

2.32805 3.823094363
2.32823 3.822530569
2.3286 3.821369008
2.32921 3.819444179
2.32999 3.817015481
2.33082 3.814410828
2.33159 3.81198197
2.3322 3.810056904
2.33257 3.808895154
2.33275 3.808331254
2.33312 3.80716949
2.33374 3.805244356
2.33451 3.802815334
2.33534 3.800210408
2.33611 3.797781367
2.33673 3.795856204
2.3371 3.794694415
2.33728 3.794130503
2.33765 3.792968723
2.33826 3.791043598
2.33903 3.788614649
2.33986 3.786009876
2.34064 3.783581047
2.34125 3.7816561
2.34162 3.780494463
2.3418 3.77993063
2.34217 3.778769024
2.34278 3.776844222
2.34356 3.774415741
2.34438 3.771811545
2.34516 3.769383325
2.34577 3.767458909
2.34614 3.766297613
2.34632 3.765733951

2.34669 3.764572709
2.3473 3.762648544
2.34808 3.760220927
2.34891 3.757617733
2.34968 3.755190518
2.35029 3.753266946
2.35066 3.752106179
2.35084 3.751542778
2.35121 3.750382084
2.35183 3.748458851
2.3526 3.746032446
2.35343 3.743430582
2.3542 3.741004622
2.35482 3.739082049
2.35519 3.737921884
2.35537 3.737358775
2.35574 3.736198683
2.35635 3.734276446
2.35712 3.731851295
2.35795 3.729250776
2.35873 3.726826068
2.35934 3.724904485
2.35971 3.723744918
2.35989 3.723182099
2.36026 3.722022604
2.36087 3.720101356
2.36165 3.717677451
2.36248 3.715078266
2.36325 3.7126548
2.36386 3.710734201
2.36423 3.709575227
2.36441 3.709012696
2.36478 3.707853793
2.36539 3.705933526

2.36617 3.703510858
2.367 3.700912996
2.36777 3.698490764
2.36838 3.696571141
2.36875 3.695412755
2.36893 3.69485051
2.3693 3.693692195
2.36992 3.691772901
2.37069 3.68935146
2.37152 3.686754913
2.37229 3.684333904
2.37291 3.68241525
2.37328 3.681257448
2.37346 3.680695486
2.37383 3.679537755
2.37444 3.677619427
2.37521 3.675199204
2.37604 3.67260396
2.37682 3.670184166
2.37743 3.668266473
2.3778 3.667109251
2.37798 3.66654757
2.37835 3.665390418
2.37896 3.663473049
2.37974 3.661054033
2.38057 3.658460084
2.38134 3.656041494
2.38195 3.654124755
2.38232 3.652968107
2.3825 3.652406706
2.38287 3.651250128
2.38348 3.64933371
2.38426 3.646915893
2.38509 3.644323228

2.38586 3.641905833
2.38647 3.63999004
2.38684 3.638833964
2.38702 3.638272839
2.38739 3.637116831
2.38801 3.635201357
2.38878 3.63278473
2.38961 3.630193337
2.39038 3.627777129
2.391 3.625862275
2.39137 3.624706764
2.39155 3.624145914
2.39192 3.622990472
2.39253 3.621075934
2.3933 3.618660487
2.39413 3.616070358
2.39491 3.613655326
2.39552 3.611741404
2.39589 3.610586455
2.39607 3.610025877
2.39644 3.608870995
2.39705 3.606957387
2.39783 3.604543109
2.39866 3.601954234
2.39943 3.59954037
2.40004 3.597627371
2.40041 3.596472978
2.40059 3.595912669
2.40096 3.594758338
2.40158 3.592845621
2.40235 3.590432415
2.40318 3.587844595
2.40395 3.585431596
2.40457 3.583519185

2.40494 3.582365098
2.40511 3.581804924
2.40548 3.580650845
2.4061 3.578738463
2.40687 3.576325535
2.4077 3.573737833
2.40847 3.571324778
2.40909 3.569412206
2.40946 3.568257974
2.40964 3.567697716
2.41001 3.566543436
2.41062 3.56463064
2.41139 3.562217046
2.41222 3.559628449
2.413 3.557214392
2.41361 3.555300911
2.41398 3.554146082
2.41416 3.553585521
2.41453 3.552430588
2.41514 3.550516629
2.41592 3.548101423
2.41675 3.545510919
2.41752 3.543094914
2.41813 3.541179776
2.4185 3.540023897
2.41868 3.539462813
2.41905 3.538306776
2.41967 3.536390906
2.42044 3.533973143
2.42127 3.531379717
2.42204 3.528960821
2.42266 3.527043276
2.42303 3.525885896
2.42321 3.52532407

2.42358 3.524166476
2.42419 3.522247945
2.42496 3.519826681
2.42579 3.51722932
2.42657 3.514806588
2.42718 3.512885887
2.42755 3.511726553
2.42773 3.511163766
2.4281 3.510004164
2.42871 3.508082224
2.42948 3.505656513
2.43031 3.503054204
2.43109 3.50062669
2.4317 3.498702085
2.43207 3.497540346
2.43225 3.496976377
2.43262 3.495814315
2.43323 3.493888217
2.43401 3.491457114
2.43484 3.488848844
2.43561 3.486415603
2.43622 3.484486345
2.43659 3.483321748
2.43677 3.48275638
2.43714 3.481591405
2.43776 3.4796604
2.43853 3.477222961
2.43936 3.474607716
2.44013 3.472167804
2.44075 3.470233144
2.44112 3.469065238
2.4413 3.468498249
2.44167 3.46732991
2.44228 3.465393249

2.44305 3.462948529
2.44388 3.460325296
2.44466 3.457877768
2.44527 3.455936956
2.44564 3.454765289
2.44582 3.454196462
2.44619 3.453024307
2.4468 3.45108124
2.44758 3.448628294
2.4484 3.445996059
2.44918 3.44353997
2.44979 3.441592258
2.45016 3.440416378
2.45034 3.439845493
2.45071 3.438669078
2.45132 3.436718903
2.4521 3.434256946
2.45293 3.431615064
2.4537 3.429150064
2.45431 3.427195391
2.45468 3.426015367
2.45486 3.425442489
2.45523 3.424262003
2.45585 3.422305193
2.45662 3.419835057
2.45745 3.417184643
2.45822 3.414711909
2.45884 3.41275126
2.45921 3.411567696
2.45939 3.410993117
2.45976 3.409809164
2.46037 3.407846716
2.46114 3.40536966
2.46197 3.402712065

2.46275 3.400232859
2.46336 3.398267233
2.46373 3.397080731
2.46391 3.396504743
2.46428 3.395317925
2.46489 3.393350839
2.46567 3.390868123
2.4665 3.388204698
2.46727 3.385720279
2.46788 3.383750674
2.46825 3.382561836
2.46843 3.381984733
2.4688 3.380795653
2.46941 3.378824926
2.47019 3.376337811
2.47102 3.373669907
2.47179 3.371181534
2.4724 3.36920895
2.47277 3.368018379
2.47295 3.367440453
2.47332 3.366249713
2.47394 3.364276345
2.47471 3.36178609
2.47554 3.359115058
2.47631 3.356623992
2.47693 3.354649426
2.4773 3.353457725
2.47748 3.352879268
2.47785 3.351687471
2.47846 3.34971246
2.47923 3.347220325
2.48006 3.344547517
2.48084 3.342055018
2.48145 3.340079469

2.48182 3.338887241
2.482 3.338308545
2.48237 3.337116294
2.48298 3.335140638
2.48376 3.332647883
2.48459 3.329974649
2.48536 3.327481977
2.48597 3.325506444
2.48634 3.32431429
2.48652 3.323735649
2.48689 3.322543546
2.48751 3.320568244
2.48828 3.318076129
2.48911 3.315403822
2.48988 3.312912236
2.49049 3.310937717
2.49086 3.309746241
2.49104 3.309167946
2.49141 3.307976594
2.49203 3.306002645
2.4928 3.30351243
2.49363 3.300842399
2.4944 3.29835316
2.49502 3.296380654
2.49539 3.295190459
2.49557 3.294612803
2.49594 3.293422804
2.49655 3.291451207
2.49732 3.288964151
2.49815 3.286297749
2.49893 3.283812116
2.49954 3.281842621
2.49991 3.280654308

```
6 1 -1 +1 2 % NLEV2 AUTO2 J2DL J2DU J2DD
0 1 2 3 4 5 % {IV2(i)}
```

Listing A.4. RKR input file for the $A^2\Pi$ state

```
57 139 8 16 +0 0 0 % IAN1 IMN1 IAN2 IMN2 CHARGE NDEGv NDEBv
'LaO - Potential energy function and constants for A state [VEXT = 0]
2 % LMAXGv
762.104 -2.209D0 %Y10 Y20 : calculated from PGOPHER fit
1 % LMAXBv
0.347149 -1.615D-3 %Y01 Y11 Y21 Y31: calculated from PGOPHER fit
0 1 0.d0 % Kaiser NSV VEXT
-0.4d0 0.1d0 6.0d0 %(1) V1 DV V2
```

Listing A.5. LEVEL input file for the $A^2\Pi-X^2\Sigma^+$ transition.

```
57 139 8 16 0 2 % IAN1 IMN1 IAN2 IMN2 CHARGE NUMPOT
'LaO A-X from RKR potentials with transition dipole moments (interpolated)'
0.0015 0.8 15.0 1.d-4 % RH RMIN RMAX EPS
99 0 0 65370.09535d0 % NTP LPPOT IOMEG VLIM
10 1 1 1 0.0D+0 % NUSE IR2 ILR NCN CNN
1.D0 1.D0 0.0d0 % RFACT EFACT VSHIFT & X-state turn. pnts.
1.6396000000000000 6505.78695212213
1.6464000000000000 5967.85526120584
1.6532000000000000 5461.49389397055
1.6600000000000000 4984.85004019116
1.6668000000000000 4536.17962801873
1.67364766904215 4110.96952152000
1.67497601776893 4031.442000000000
1.67632098853836 3951.87094848000
1.67768309829561 3872.25638784000
1.67906289115588 3792.59833896000
1.68046094044261 3712.89682272000
1.68187785092637 3633.151860000000
1.68331426128916 3553.36347168000
1.68477084684259 3473.53167864000
1.68624832253247 3393.65650176000
```

1.68774744626775	3313.73796192000
1.68926902261744	3233.77608000000
1.69081390692670	3153.77087688000
1.69238300991147	3073.72237344000
1.69397730280155	2993.63059056000
1.69559782311424	2913.49554912000
1.69724568115572	2833.31727000000
1.69892206736540	2753.09577408000
1.70062826064085	2672.83108224000
1.70236563780815	2592.52321536000
1.70413568443630	2512.17219432000
1.70594000723647	2431.77804000000
1.70778034833935	2351.34077328000
1.70965860181047	2270.86041504000
1.71157683284766	2190.33698616000
1.71353730021283	2109.77050752000
1.71554248259005	2029.16100000000
1.71759510974379	1948.50848448000
1.71969819959074	1867.81298184000
1.72185510261756	1787.07451296000
1.72406955550547	1706.29309872000
1.72634574640710	1625.46876000000
1.72868839512760	1544.60151768000
1.73110285259206	1463.69139264000
1.73359522559074	1382.73840576000
1.73617253512549	1301.74257792000
1.73884292012748	1220.70393000000
1.74161590352296	1139.62248288000
1.74450274568323	1058.49825744000
1.74751692312083	977.33127456000
1.75067479135691	896.12155512000
1.75399652674741	814.86912000000
1.75750750574127	733.57399008000
1.76124039887786	652.23618624000

1.76523849212923	570.85572936000
1.76956124916133	489.43264032000
1.77429429643224	407.96694000000
1.77956908076329	326.45864928000
1.78560692422095	244.90778904000
1.79283946692507	163.31438016000
1.80238133483583	81.67844352000
1.82597098502407	0.00000000000
1.85036767705890	81.67844352000
1.86071712846108	163.31438016000
1.86875779704300	244.90778904000
1.87560430950783	326.45864928000
1.88168830671986	407.96694000000
1.88723111149147	489.43264032000
1.89236417139135	570.85572936000
1.89717311362641	652.23618624000
1.90171740261289	733.57399008000
1.90604032507459	814.86912000000
1.91017455230412	896.12155512000
1.91414546150515	977.33127456000
1.91797322978980	1058.49825744000
1.92167421343691	1139.62248288000
1.92526188971822	1220.70393000000
1.92874751976568	1301.74257792000
1.93214062726771	1382.73840576000
1.93544935191918	1463.69139264000
1.93868071548710	1544.60151768000
1.94184082552844	1625.46876000000
1.94493503373650	1706.29309872000
1.94796806068616	1787.07451296000
1.95094409530132	1867.81298184000
1.95386687503598	1948.50848448000
1.95673975115112	2029.16100000000
1.95956574233929	2109.77050752000

1.96234757914236	2190.33698616000
1.96508774102334	2270.86041504000
1.96778848752464	2351.34077328000
1.97045188462615	2431.77804000000
1.97307982717699	2512.17219432000
1.97567405809305	2592.52321536000
1.97823618487222	2672.83108224000
1.98076769387183	2753.09577408000
1.98326996270784	2833.31727000000
1.98574427106930	2913.49554912000
1.98819181018866	2993.63059056000
1.99061369116676	3073.72237344000
1.99301095231715	3153.77087688000
1.99538456566744	3233.77608000000
1.99773544273305	3313.73796192000
2.00006443966016	3393.65650176000

99 0 0 47532.70155	% NTP2 LPPOT2 IOMEG2 VLIM2
10 1 1 1 0.D0	% NUSE2 IR22 ILR2 NCN2 CNN2
1.D0 1.D0 13066.6492D0	% RFACT EFAC2 VSHIFT2 & A state
1.64930000000000	6057.55226430662
1.65620000000000	5555.94409209537
1.66310000000000	5084.08018365961
1.67000000000000	4640.19676943464
1.67690000000000	4222.63466752017
1.68381012211800	3829.27431000000
1.68515833249157	3755.29500000000
1.68652366071298	3681.27151000000
1.68790664124284	3607.20384000000
1.68930783665097	3533.09199000000
1.69072783972552	3458.93596000000
1.69216727578985	3384.73575000000
1.69362680525279	3310.49136000000
1.69510712642148	3236.20279000000

1.69660897861078	3161.87004000000
1.69813314558830	3087.49311000000
1.69968045940036	3013.07200000000
1.70125180463177	2938.60671000000
1.70284812316085	2864.09724000000
1.70447041948222	2789.54359000000
1.70611976668218	2714.94576000000
1.70779731316733	2640.30375000000
1.70950429026576	2565.61756000000
1.71124202084317	2490.88719000000
1.71301192910464	2416.11264000000
1.71481555178753	2341.29391000000
1.71665455099494	2266.43100000000
1.71853072897316	2191.52391000000
1.72044604520568	2116.57264000000
1.72240263628351	2041.57719000000
1.72440283912354	1966.53756000000
1.72644921825110	1891.45375000000
1.72854459805147	1816.32576000000
1.73069210114285	1741.15359000000
1.73289519435361	1665.93724000000
1.73515774423033	1590.67671000000
1.73748408460805	1515.37200000000
1.73987909960934	1440.02311000000
1.74234832660877	1364.63004000000
1.74489808536518	1289.19279000000
1.74753564193883	1213.71136000000
1.75026941957831	1138.18575000000
1.75310927415270	1062.61596000000
1.75606686004829	987.00199000000
1.75915612572756	911.34384000000
1.76239399995466	835.64151000000
1.76580136682054	759.89500000000
1.76940449363522	684.10431000000

1.77323719878589	608.26944000000
1.77734429026967	532.39039000000
1.78178732427839	456.46716000000
1.78665494284321	380.49975000000
1.79208322569052	304.48816000000
1.79830130161944	228.43239000000
1.80575604812855	152.33244000000
1.81560147095280	76.18831000000
1.83999124681976	0.00000000000
1.86528718274001	76.18831000000
1.87603924308328	152.33244000000
1.88440110510654	228.43239000000
1.89152677507506	304.48816000000
1.89786313101858	380.49975000000
1.90363930226832	456.46716000000
1.90899136908362	532.39039000000
1.91400797402949	608.26944000000
1.91875067383250	684.10431000000
1.92326427702539	759.89500000000
1.92758260253188	835.64151000000
1.93173191819943	911.34384000000
1.93573310865731	987.00199000000
1.93960310320887	1062.61596000000
1.94335585085676	1138.18575000000
1.94700300652828	1213.71136000000
1.95055442663445	1289.19279000000
1.95401853496672	1364.63004000000
1.95740259812910	1440.02311000000
1.96071293642514	1515.37200000000
1.96395508777496	1590.67671000000
1.96713393684767	1665.93724000000
1.97025381802574	1741.15359000000
1.97331859840408	1816.32576000000
1.97633174536035	1891.45375000000

1.6056 7.430350007
1.60637 7.428212977
1.6072 7.425922385
1.60797 7.423787475
1.60859 7.422096067
1.60896 7.421075597
1.60914 7.420580343
1.60951 7.419560141
1.61012 7.417869972
1.61089 7.41573804
1.61172 7.413452395
1.61249 7.411321613
1.61311 7.409633144
1.61348 7.408614305
1.61366 7.408119804
1.61403 7.407101074
1.61464 7.405413109
1.61541 7.403283538
1.61624 7.400999904
1.61702 7.398870512
1.61763 7.397182813
1.618 7.396164296
1.61818 7.395669913
1.61855 7.394651346
1.61916 7.392963415
1.61994 7.390833467
1.62077 7.388548909
1.62154 7.386418171
1.62215 7.384729071
1.62252 7.383709567
1.6227 7.383214666
1.62307 7.382194953
1.62369 7.380504886
1.62446 7.378371824

1.62529 7.376083407
1.62606 7.373948584
1.62668 7.372255915
1.62705 7.371234114
1.62723 7.37073806
1.6276 7.369715891
1.62821 7.36802152
1.62898 7.365882606
1.62981 7.363587394
1.63059 7.361445749
1.6312 7.35974734
1.63157 7.358721934
1.63175 7.358224091
1.63212 7.357198157
1.63273 7.355497312
1.6335 7.353349809
1.63433 7.351044866
1.63511 7.348893662
1.63572 7.347187345
1.63609 7.346157024
1.63627 7.345656756
1.63664 7.344625748
1.63725 7.342916259
1.63803 7.340757431
1.63886 7.338439821
1.63963 7.33627632
1.64024 7.334559925
1.64061 7.333523379
1.64079 7.333020052
1.64116 7.331982661
1.64178 7.330262358
1.64255 7.328089466
1.64338 7.325756254
1.64415 7.32357772

1.64477 7.321849077
1.64514 7.320804998
1.64532 7.320297975
1.64569 7.319252891
1.6463 7.317519605
1.64707 7.315329913
1.6479 7.312978163
1.64868 7.310781858
1.64929 7.309038798
1.64966 7.307985876
1.64984 7.307474522
1.65021 7.306420437
1.65082 7.304672024
1.6516 7.302462962
1.65242 7.300090228
1.6532 7.297874299
1.65381 7.296115737
1.65418 7.295053513
1.65436 7.294537665
1.65473 7.293474367
1.65534 7.291710846
1.65612 7.289482998
1.65695 7.287090462
1.65772 7.28485639
1.65833 7.283083669
1.6587 7.282012994
1.65888 7.281493069
1.65925 7.280421426
1.65987 7.278644232
1.66064 7.27639941
1.66147 7.273989016
1.66224 7.271738612
1.66286 7.269953166
1.66323 7.268874907

1.66341 7.268351326
1.66378 7.267272204
1.66439 7.265482772
1.66516 7.263222788
1.66599 7.260796478
1.66677 7.258531554
1.66738 7.25673482
1.66775 7.255649843
1.66793 7.255123027
1.6683 7.254037292
1.66891 7.252237059
1.66969 7.249963724
1.67052 7.247523441
1.67129 7.245245808
1.6719 7.243439222
1.67227 7.242348393
1.67245 7.241818762
1.67282 7.240727282
1.67343 7.238917683
1.67421 7.236632808
1.67504 7.234180494
1.67581 7.231891964
1.67642 7.230076962
1.67679 7.228981148
1.67697 7.228449123
1.67734 7.227352763
1.67796 7.225535234
1.67873 7.223240632
1.67956 7.22077823
1.68033 7.218480614
1.68095 7.216658631
1.68132 7.215558699
1.6815 7.215024701
1.68187 7.213924327

1.68248 7.212100304
1.68325 7.209797785
1.68408 7.207327239
1.68486 7.205022349
1.68547 7.203194821
1.68584 7.202091636
1.68602 7.201556085
1.68639 7.200452564
1.687 7.198623483
1.68778 7.19631486
1.68861 7.193838111
1.68938 7.191527759
1.68999 7.189696121
1.69036 7.188590551
1.69054 7.188053868
1.69091 7.186948067
1.69153 7.185115362
1.6923 7.182802446
1.69313 7.180321438
1.6939 7.178007435
1.69452 7.176173124
1.69489 7.175066034
1.69506 7.174528639
1.69543 7.173421424
1.69605 7.171586533
1.69682 7.169271135
1.69765 7.16678781
1.69842 7.164471967
1.69904 7.162636419
1.69941 7.161528677
1.69959 7.16099099
1.69996 7.159883228
1.70057 7.15804758
1.70134 7.155731451

1.70217 7.153247536
1.70295 7.150931244
1.70356 7.149095357
1.70393 7.1479874
1.70411 7.147449603
1.70448 7.146341597
1.70509 7.144505479
1.70587 7.142188635
1.7067 7.1397038
1.70747 7.13738651
1.70808 7.135549734
1.70845 7.1344412
1.70863 7.133903111
1.709 7.132794481
1.70962 7.13095726
1.71039 7.128638902
1.71122 7.126152292
1.71199 7.123833205
1.71261 7.121994908
1.71298 7.120885414
1.71316 7.120346849
1.71353 7.119237212
1.71414 7.117398256
1.71491 7.115077585
1.71574 7.112588344
1.71652 7.110266662
1.71713 7.108426212
1.7175 7.107315377
1.71768 7.106776149
1.71805 7.105665125
1.71866 7.103823801
1.71943 7.10150002
1.72026 7.099007291
1.72104 7.096682216

1.72165 7.094838979
1.72202 7.093726421
1.7222 7.093186345
1.72257 7.092073552
1.72318 7.090229227
1.72396 7.087901537
1.72479 7.085404466
1.72556 7.083075199
1.72617 7.081228543
1.72654 7.08011388
1.72672 7.079572771
1.72709 7.078457827
1.72771 7.076609868
1.72848 7.074277472
1.72931 7.071775201
1.73008 7.069440944
1.7307 7.067590236
1.73107 7.066473087
1.73125 7.06593076
1.73162 7.064813283
1.73223 7.062961058
1.733 7.060623157
1.73383 7.05811483
1.73461 7.055774785
1.73522 7.053919393
1.73559 7.052799375
1.73577 7.052255645
1.73614 7.051135253
1.73675 7.04927813
1.73752 7.046933925
1.73835 7.044418687
1.73913 7.042072056
1.73974 7.040211347
1.74011 7.039088079

1.74029 7.03854276
1.74066 7.037419071
1.74127 7.035556416
1.74205 7.03320511
1.74288 7.030682105
1.74365 7.028328089
1.74426 7.02646143
1.74463 7.02533453
1.74481 7.024787437
1.74518 7.02366007
1.7458 7.021791251
1.74657 7.019432045
1.7474 7.016900416
1.74817 7.014538218
1.74879 7.012664977
1.74916 7.011534063
1.74934 7.010985011
1.74971 7.009853583
1.75032 7.007977968
1.75109 7.005610079
1.75192 7.003069038
1.7527 7.000698005
1.75331 6.998817743
1.75368 6.997682592
1.75386 6.997131484
1.75423 6.995995826
1.75484 6.994113223
1.75562 6.991736565
1.75644 6.989186178
1.75722 6.986806485
1.75783 6.984919397
1.7582 6.983780142
1.75838 6.983227047
1.75875 6.982087304

1.75936 6.980197958
1.76014 6.977812839
1.76097 6.975253438
1.76174 6.972865394
1.76235 6.970971725
1.76272 6.969828515
1.7629 6.969273504
1.76327 6.968129824
1.76389 6.96623398
1.76466 6.96384071
1.76549 6.961272626
1.76626 6.95887654
1.76688 6.956976536
1.76725 6.955829518
1.76743 6.955272664
1.7678 6.954125194
1.76841 6.952223097
1.76918 6.949821985
1.77001 6.94724555
1.77079 6.944841732
1.7714 6.942935636
1.77177 6.941784959
1.77195 6.941226333
1.77232 6.940075221
1.77293 6.938167117
1.77371 6.935758472
1.77454 6.933174018
1.77531 6.930762776
1.77592 6.928850835
1.77629 6.927696646
1.77647 6.927136319
1.77684 6.925981714
1.77745 6.924067847
1.77823 6.921651978

1.77906 6.919059836
1.77983 6.916641481
1.78044 6.914723938
1.78081 6.913566386
1.78099 6.913004431
1.78136 6.911846479
1.78198 6.909927095
1.78275 6.907504311
1.78358 6.904904813
1.78435 6.902479653
1.78497 6.900556755
1.78534 6.899395987
1.78552 6.898832475
1.78589 6.897671326
1.7865 6.895746668
1.78727 6.89331728
1.7881 6.890710757
1.78888 6.888279101
1.78949 6.886351093
1.78986 6.885187256
1.79004 6.884622259
1.79041 6.88345806
1.79102 6.881528375
1.7918 6.879092691
1.79263 6.876479475
1.7934 6.874041632
1.79401 6.872108759
1.79438 6.870942002
1.79456 6.870375592
1.79493 6.869208491
1.79555 6.867274023
1.79632 6.864832352
1.79715 6.862212774
1.79792 6.859769055

1.79854 6.857831561
1.79891 6.856662032
1.79908 6.856094281
1.79945 6.854924425
1.80007 6.85298542
1.80084 6.850538069
1.80167 6.847912448
1.80244 6.845463126
1.80306 6.843521208
1.80343 6.842349015
1.80361 6.841779971
1.80398 6.840607454
1.80459 6.838664041
1.80536 6.836211125
1.80619 6.833579533
1.80697 6.831124641
1.80758 6.829178307
1.80795 6.828003447
1.80813 6.827433109
1.8085 6.826257924
1.80911 6.824310089
1.80989 6.821851592
1.81072 6.819214011
1.81149 6.816753532
1.8121 6.814802766
1.81247 6.813625232
1.81265 6.813053595
1.81302 6.811875735
1.81364 6.809923465
1.81441 6.80745937
1.81524 6.804815781
1.81601 6.802349697
1.81663 6.800394487
1.817 6.79921427

1.81718 6.798641331
1.81755 6.797460787
1.81816 6.795504068
1.81893 6.793034357
1.81976 6.790384743
1.82054 6.787913037
1.82115 6.78595337
1.82152 6.784770461
1.8217 6.784196216
1.82207 6.78301298
1.82268 6.781051799
1.82345 6.778576454
1.82428 6.775920796
1.82506 6.773443451
1.82567 6.771479313
1.82604 6.770293705
1.82622 6.769718149
1.82659 6.768532213
1.8272 6.766566556
1.82798 6.764085562
1.82881 6.761423842
1.82958 6.75894084
1.83019 6.756972217
1.83056 6.755783902
1.83074 6.755207032
1.83111 6.754018387
1.83173 6.75204824
1.8325 6.749561579
1.83333 6.746893778
1.8341 6.744405104
1.83472 6.742431982
1.83509 6.741240951
1.83527 6.740662763
1.83564 6.739471401

1.83625 6.737496752
1.83702 6.735004406
1.83785 6.732330506
1.83863 6.729836141
1.83924 6.727858507
1.83961 6.726664752
1.83979 6.726085242
1.84016 6.724891156
1.84077 6.722911989
1.84154 6.720413942
1.84237 6.717733925
1.84315 6.715233852
1.84376 6.713251693
1.84413 6.712055206
1.84431 6.711474369
1.84468 6.71027755
1.84529 6.708293854
1.84607 6.705790088
1.8469 6.703103934
1.84767 6.700598138
1.84828 6.698611439
1.84865 6.697412212
1.84883 6.696830045
1.8492 6.695630484
1.84982 6.693642244
1.85059 6.691132743
1.85142 6.68844044
1.85219 6.685928914
1.85281 6.683937682
1.85318 6.682735724
1.85336 6.682152232
1.85373 6.680949946
1.85434 6.678957199
1.85511 6.676442033

1.85594 6.673743681
1.85672 6.67122654
1.85733 6.669230876
1.8577 6.66802625
1.85788 6.667441465
1.85825 6.66623652
1.85886 6.664239379
1.85964 6.66171869
1.86047 6.659014443
1.86124 6.656491832
1.86185 6.654491848
1.86222 6.653284623
1.8624 6.652698579
1.86277 6.651491043
1.86338 6.649489621
1.86416 6.646963553
1.86499 6.644253565
1.86576 6.641725625
1.86637 6.639721435
1.86674 6.63851168
1.86692 6.637924409
1.86729 6.636714351
1.86791 6.634708762
1.86868 6.632177458
1.86951 6.629461882
1.87028 6.626928757
1.8709 6.624920475
1.87127 6.623708258
1.87145 6.623119794
1.87182 6.621907282
1.87243 6.619897639
1.8732 6.617361243
1.87403 6.614640232
1.87481 6.612102065

1.87542 6.610089805
1.87579 6.608875193
1.87597 6.60828557
1.87634 6.607070673
1.87695 6.60505709
1.87773 6.602515744
1.87856 6.599789452
1.87933 6.597246386
1.87994 6.595230261
1.88031 6.594013324
1.88049 6.593422574
1.88086 6.59220536
1.88147 6.59018795
1.88225 6.587641798
1.88308 6.584910379
1.88385 6.582362557
1.88446 6.58034268
1.88483 6.579123487
1.88501 6.578531644
1.88538 6.577312181
1.886 6.575291058
1.88677 6.572740242
1.8876 6.57000385
1.88837 6.567451415
1.88899 6.5654279
1.88936 6.564206518
1.88954 6.563613615
1.88991 6.562391972
1.89052 6.560367249
1.89129 6.557811914
1.89212 6.555070701
1.8929 6.552513797
1.89351 6.550486757
1.89388 6.549263256

1.89406 6.548669325
1.89443 6.547445571
1.89504 6.545417362
1.89582 6.542857649
1.89665 6.54011177
1.89742 6.53755054
1.89803 6.535520088
1.8984 6.534294536
1.89858 6.533699612
1.89895 6.532473815
1.89957 6.530442233
1.90034 6.527878286
1.90117 6.525127887
1.90194 6.522562449
1.90256 6.52052866
1.90293 6.519301089
1.9031 6.518705184
1.90347 6.517477361
1.90409 6.515442406
1.90486 6.51287417
1.90569 6.510119121
1.90646 6.507549301
1.90708 6.505512006
1.90745 6.504282306
1.90763 6.503685364
1.908 6.502455397
1.90861 6.500416866
1.90938 6.497844078
1.91021 6.495084097
1.91099 6.492509632
1.9116 6.490468623
1.91197 6.489236669
1.91215 6.488638628
1.91252 6.487406391

1.91313 6.485364077
1.91391 6.482786473
1.91474 6.48002128
1.91551 6.477441906
1.91612 6.475396976
1.91649 6.474162641
1.91667 6.473563441
1.91704 6.472328809
1.91766 6.470282502
1.91843 6.467699821
1.91926 6.464929132
1.92003 6.462344588
1.92065 6.460295527
1.92102 6.459058686
1.9212 6.458458266
1.92157 6.457221112
1.92218 6.455170604
1.92295 6.452582583
1.92378 6.449806117
1.92456 6.447216139
1.92517 6.44516274
1.92554 6.443923268
1.92572 6.443321567
1.92609 6.442081766
1.9267 6.440026849
1.92747 6.437433225
1.9283 6.4346507
1.92908 6.432055026
1.92969 6.42999708
1.93006 6.42875485
1.93024 6.428151807
1.93061 6.426909233
1.93122 6.424849699
1.932 6.422250209

1.93283 6.419461343
1.9336 6.41685971
1.93421 6.41479701
1.93458 6.413551896
1.93476 6.41294745
1.93513 6.411701978
1.93575 6.409637619
1.93652 6.407031999
1.93735 6.404236511
1.93812 6.401628657
1.93874 6.399560993
1.93911 6.398312871
1.93929 6.39770696
1.93966 6.396458464
1.94027 6.394389071
1.94104 6.39177706
1.94187 6.388974668
1.94265 6.386360329
1.94326 6.384287493
1.94363 6.383036237
1.94381 6.382428801
1.94418 6.381177155
1.94479 6.37910252
1.94557 6.376483855
1.94639 6.373674277
1.94717 6.37105319
1.94778 6.368974975
1.94815 6.367720458
1.94833 6.367111437
1.9487 6.365856515
1.94931 6.36377643
1.95009 6.361150848
1.95092 6.35833381
1.95169 6.355705757

1.9523 6.353622034
1.95267 6.352364205
1.95285 6.351753581
1.95322 6.350495369
1.95384 6.348409873
1.95461 6.345777559
1.95544 6.342953443
1.95621 6.340318925
1.95683 6.33823017
1.9572 6.336969345
1.95738 6.336357277
1.95775 6.335096113
1.95836 6.33300579
1.95913 6.330367503
1.95996 6.327537125
1.96074 6.324896904
1.96135 6.322803721
1.96172 6.321540264
1.9619 6.320926929
1.96227 6.319663176
1.96288 6.317568631
1.96366 6.314925132
1.96449 6.312089311
1.96526 6.309444147
1.96587 6.307347141
1.96624 6.306081416
1.96642 6.305466991
1.96679 6.304201014
1.9674 6.302102849
1.96818 6.299454901
1.96901 6.296614453
1.96978 6.29396511
1.97039 6.291864884
1.97076 6.290597254

1.97094 6.289981916
1.97131 6.288714081
1.97193 6.2866129
1.9727 6.283961264
1.97353 6.281117006
1.9743 6.278464245
1.97492 6.276361403
1.97529 6.275092234
1.97547 6.27447616
1.97584 6.273206829
1.97645 6.271103237
1.97722 6.268448675
1.97805 6.265601424
1.97883 6.262946007
1.97944 6.260841153
1.97981 6.25957081
1.97999 6.258954175
1.98036 6.257683714
1.98097 6.255578315
1.98175 6.252921589
1.98258 6.250072161
1.98335 6.247414851
1.98396 6.245308588
1.98433 6.244037434
1.98451 6.243420417
1.98488 6.24214919
1.9855 6.240042587
1.98627 6.237384458
1.9871 6.234533672
1.98787 6.23187523
1.98848 6.229768162
1.98885 6.228496562
1.98903 6.22787934
1.9894 6.226607711

1.99002 6.224500507
1.99079 6.221841738
1.99162 6.21899041
1.99239 6.216331598
1.99301 6.214224329
1.99338 6.212952648
1.99356 6.212335396
1.99393 6.21106373
1.99454 6.20895653
1.99531 6.206297883
1.99614 6.20344683
1.99692 6.200788409
1.99753 6.198681543
1.9979 6.197410145
1.99808 6.196793042
1.99845 6.195521702
1.99906 6.19341511
1.99984 6.190757346
2.00067 6.18790738
2.00144 6.185250061
2.00205 6.183144093
2.00242 6.181873235
2.0026 6.181256391
2.00297 6.179985577
2.00359 6.177879816
2.00436 6.175222992
2.00519 6.172373848
2.00596 6.169717108
2.00658 6.16761147
2.00695 6.166340756
2.00712 6.165723967
2.00749 6.164453235
2.00811 6.162347519
2.00888 6.159690589

2.00971 6.156841129
2.01048 6.154183907
2.0111 6.152077758
2.01147 6.15080668
2.01165 6.150189699
2.01202 6.148918542
2.01263 6.146812029
2.0134 6.144153931
2.01423 6.141303018
2.01501 6.138644251
2.01562 6.136536749
2.01599 6.1352648
2.01617 6.134647381
2.01654 6.133375291
2.01715 6.13126714
2.01793 6.128606813
2.01876 6.125753307
2.01953 6.123091935
2.02014 6.120982239
2.02051 6.11970891
2.02069 6.119090807
2.02106 6.117817276
2.02168 6.115706646
2.02245 6.113043028
2.02328 6.110185791
2.02405 6.107520751
2.02467 6.10540802
2.02504 6.104132804
2.02522 6.10351377
2.02559 6.10223829
2.0262 6.100124339
2.02697 6.097456369
2.0278 6.094594263
2.02858 6.091924495

2.02919 6.089807886
2.02956 6.088530276
2.02974 6.087910065
2.03011 6.086632128
2.03072 6.084514015
2.03149 6.081840631
2.03232 6.078972517
2.0331 6.076296958
2.03371 6.074175632
2.03408 6.072895119
2.03426 6.072273484
2.03463 6.070992583
2.03524 6.068869467
2.03602 6.066189607
2.03685 6.063314346
2.03762 6.060631936
2.03823 6.05850505
2.0386 6.057221126
2.03878 6.056597821
2.03915 6.055313448
2.03977 6.053184487
2.04054 6.05049709
2.04137 6.047613545
2.04214 6.044923221
2.04276 6.042789934
2.04313 6.041502092
2.04331 6.04087687
2.04368 6.039588518
2.04429 6.037452871
2.04506 6.034756875
2.04589 6.031863907
2.04667 6.029164607
2.04728 6.027024078
2.04765 6.025731811

2.04783 6.025104426
2.0482 6.023811586
2.04881 6.021668411
2.04959 6.018962755
2.05041 6.016059228
2.05119 6.01334996
2.0518 6.011201523
2.05217 6.009904508
2.05235 6.009274829
2.05272 6.007977296
2.05333 6.005826467
2.05411 6.003111451
2.05494 6.000198377
2.05571 5.997480726
2.05632 5.995326003
2.05669 5.994025348
2.05687 5.993393945
2.05724 5.992092943
2.05786 5.98993662
2.05863 5.987215124
2.05946 5.984295661
2.06023 5.981572576
2.06085 5.979413904
2.06122 5.978111019
2.0614 5.977478574
2.06177 5.976175514
2.06238 5.974016034
2.06315 5.971291006
2.06398 5.968368316
2.06476 5.965642744
2.06537 5.963482459
2.06574 5.962178754
2.06592 5.961545953
2.06629 5.960242245

2.0669 5.958081944
2.06768 5.955356332
2.06851 5.952433577
2.06928 5.949708466
2.06989 5.947548905
2.07026 5.94624579
2.07044 5.945613317
2.07081 5.94431037
2.07142 5.942151584
2.0722 5.939428337
2.07303 5.936508678
2.0738 5.933786976
2.07441 5.931630476
2.07478 5.930329361
2.07496 5.9296979
2.07533 5.928397125
2.07595 5.926242191
2.07672 5.923524257
2.07755 5.920610854
2.07832 5.91789551
2.07894 5.915744407
2.07931 5.914446702
2.07949 5.913816938
2.07986 5.912519744
2.08047 5.910371
2.08124 5.907661325
2.08207 5.904757342
2.08285 5.902051303
2.08346 5.899907933
2.08383 5.898615048
2.08401 5.897987666
2.08438 5.896695463
2.08499 5.894555244
2.08577 5.891856778

2.0866 5.888965375
2.08737 5.88627159
2.08798 5.88413829
2.08835 5.882851635
2.08853 5.882227319
2.0889 5.880941517
2.08952 5.87881216
2.09029 5.87612785
2.09112 5.873252189
2.09189 5.870573606
2.09251 5.868452712
2.09288 5.867173698
2.09305 5.866553131
2.09342 5.865275141
2.09404 5.863158982
2.09481 5.860491777
2.09564 5.85763502
2.09641 5.854974586
2.09703 5.852868435
2.0974 5.851598471
2.09758 5.850982339
2.09795 5.84971357
2.09856 5.847612946
2.09933 5.844965794
2.10016 5.842131101
2.10094 5.839491705
2.10155 5.83740242
2.10192 5.83614267
2.1021 5.835531497
2.10247 5.834272935
2.10308 5.832189138
2.10386 5.82956293
2.10469 5.826750124
2.10546 5.824130447

2.10607 5.822056303
2.10644 5.820805482
2.10662 5.820198586
2.10699 5.818948719
2.10761 5.816878985
2.10838 5.814269906
2.10921 5.811474707
2.10998 5.808870736
2.1106 5.806808553
2.11097 5.805564742
2.11115 5.804961192
2.11152 5.803718101
2.11213 5.801659251
2.1129 5.799063288
2.11373 5.796281393
2.1145 5.793689116
2.11512 5.791635715
2.11549 5.790396994
2.11567 5.789795858
2.11604 5.788557625
2.11665 5.786506479
2.11742 5.78391962
2.11825 5.781146727
2.11903 5.778562133
2.11964 5.776514333
2.12001 5.775278784
2.12019 5.774679131
2.12056 5.773443836
2.12117 5.771397213
2.12195 5.768815448
2.12278 5.766047253
2.12355 5.763466329
2.12416 5.761420951
2.12453 5.760186655

2.12471 5.759587553
2.12508 5.758353278
2.1257 5.756307999
2.12647 5.753727314
2.1273 5.750959516
2.12807 5.748378251
2.12869 5.746332114
2.12906 5.745097152
2.12924 5.74449767
2.12961 5.743262496
2.13022 5.741215381
2.13099 5.738631764
2.13182 5.73586006
2.1326 5.733274441
2.13321 5.731224366
2.13358 5.729986819
2.13376 5.729386026
2.13413 5.728148033
2.13474 5.726095903
2.13551 5.723505343
2.13634 5.720725429
2.13712 5.718131444
2.13773 5.716074252
2.1381 5.7148322
2.13828 5.714229165
2.13865 5.712986435
2.13926 5.710926109
2.14004 5.708324593
2.14087 5.705532168
2.14164 5.702925806
2.14225 5.700858315
2.14262 5.699609841
2.1428 5.699003631
2.14317 5.697754245

2.14379 5.695682544
2.14456 5.69306606
2.14539 5.690256821
2.14616 5.687634069
2.14678 5.685553101
2.14715 5.684296285
2.14733 5.683685969
2.1477 5.682428008
2.14831 5.680341752
2.14908 5.677706289
2.14991 5.674875933
2.15069 5.672232801
2.1513 5.670135305
2.15167 5.668868397
2.15185 5.668253159
2.15222 5.666985022
2.15283 5.664881842
2.15361 5.662225052
2.15443 5.659372058
2.15521 5.656708215
2.15582 5.654594611
2.15619 5.653318114
2.15637 5.652698258
2.15674 5.651420678
2.15735 5.649302071
2.15813 5.646626202
2.15896 5.643753229
2.15973 5.641071205
2.16034 5.638943498
2.16071 5.637658622
2.16089 5.637034734
2.16126 5.635748922
2.16188 5.633616891
2.16265 5.630924473

2.16348 5.628034234
2.16425 5.625336557
2.16487 5.623196752
2.16524 5.621904706
2.16542 5.621277374
2.16579 5.619984539
2.1664 5.617841089
2.16717 5.615134651
2.168 5.612229856
2.16878 5.609519056
2.16939 5.607369157
2.16976 5.606071151
2.16994 5.605440961
2.17031 5.604142314
2.17092 5.601989449
2.1717 5.59927152
2.17253 5.596354883
2.1733 5.593633488
2.17391 5.591475499
2.17428 5.590172743
2.17446 5.589540283
2.17483 5.588237032
2.17544 5.586076757
2.17622 5.583349866
2.17705 5.580424099
2.17782 5.577694638
2.17843 5.575530565
2.1788 5.574224268
2.17898 5.573590126
2.17935 5.572283481
2.17997 5.5701178
2.18074 5.567384476
2.18157 5.564452291
2.18234 5.561717294

2.18296 5.559549139
2.18333 5.558240511
2.18351 5.557605273
2.18388 5.556296444
2.18449 5.554127362
2.18526 5.551390134
2.18609 5.548454243
2.18687 5.545716239
2.18748 5.543546009
2.18785 5.542236259
2.18803 5.541600512
2.1884 5.540290709
2.18901 5.538120229
2.18979 5.535381627
2.19062 5.532444743
2.19139 5.52970626
2.192 5.527535958
2.19237 5.526226296
2.19255 5.525590628
2.19292 5.52428106
2.19354 5.522111188
2.19431 5.51937374
2.19514 5.516438574
2.19591 5.513702143
2.19653 5.511533773
2.1969 5.51022541
2.19707 5.509590407
2.19744 5.508282283
2.19806 5.506115024
2.19883 5.503381259
2.19966 5.500450524
2.20043 5.497718669
2.20105 5.495554202
2.20142 5.494248291

2.2016 5.493614501
2.20197 5.492308916
2.20258 5.49014596
2.20335 5.487417736
2.20418 5.484492984
2.20496 5.481766653
2.20557 5.479606495
2.20594 5.478303154
2.20612 5.477670604
2.20649 5.476367556
2.2071 5.474208755
2.20788 5.471485686
2.20871 5.468566353
2.20948 5.465844973
2.21009 5.463688669
2.21046 5.462387624
2.21064 5.46175618
2.21101 5.460455395
2.21163 5.458300295
2.2124 5.455581806
2.21323 5.452667276
2.214 5.449950273
2.21462 5.447797369
2.21499 5.446498346
2.21517 5.445867875
2.21554 5.444569079
2.21615 5.442417224
2.21692 5.439702742
2.21775 5.436792401
2.21853 5.434079202
2.21914 5.431929243
2.21951 5.430631967
2.21969 5.430002336
2.22006 5.428705254

2.22067 5.42655619
2.22144 5.423845141
2.22227 5.420938373
2.22305 5.418228404
2.22366 5.416080935
2.22403 5.414785132
2.22421 5.414156208
2.22458 5.412860566
2.22519 5.410713838
2.22597 5.408005649
2.2268 5.405101838
2.22757 5.402394525
2.22818 5.400249092
2.22855 5.398954488
2.22873 5.398326138
2.2291 5.39703166
2.22972 5.394886814
2.23049 5.392180911
2.23132 5.389279442
2.23209 5.386574212
2.23271 5.38443036
2.23308 5.38313668
2.23326 5.38250877
2.23363 5.381215184
2.23424 5.379071764
2.23501 5.376367574
2.23584 5.373467832
2.23662 5.370764111
2.23723 5.368621385
2.2376 5.367328354
2.23778 5.366700752
2.23815 5.365407782
2.23876 5.363265334
2.23953 5.360562283

2.24036 5.357663653
2.24114 5.354960867
2.24175 5.352818812
2.24212 5.351526157
2.2423 5.350898729
2.24267 5.349606101
2.24328 5.347464171
2.24406 5.344761684
2.24489 5.341863551
2.24566 5.339161127
2.24627 5.337019289
2.24664 5.335726735
2.24682 5.335099348
2.24719 5.333806788
2.24781 5.33166492
2.24858 5.328962424
2.24941 5.326064173
2.25018 5.323361536
2.2508 5.321219464
2.25117 5.319926745
2.25135 5.319299273
2.25172 5.318006527
2.25233 5.315864327
2.2531 5.313161385
2.25393 5.310262645
2.25471 5.307559566
2.25532 5.305417164
2.25569 5.304124255
2.25587 5.303496693
2.25624 5.302203767
2.25685 5.300061285
2.25763 5.297358015
2.25846 5.294458956
2.25923 5.291755611

2.25984 5.28961302
2.26021 5.288320007
2.26039 5.287692396
2.26076 5.286399376
2.26137 5.284256753
2.26215 5.281553332
2.26298 5.278654145
2.26375 5.275950713
2.26436 5.273808074
2.26473 5.272515041
2.26491 5.271887423
2.26528 5.270594394
2.2659 5.268451771
2.26667 5.265748377
2.2675 5.262849254
2.26827 5.260145912
2.26889 5.258003367
2.26926 5.256710399
2.26944 5.256082816
2.26981 5.254789863
2.27042 5.252647381
2.27119 5.249944192
2.27202 5.247045323
2.2728 5.24434225
2.27341 5.24219994
2.27378 5.240907123
2.27396 5.240279616
2.27433 5.238986823
2.27494 5.236844624
2.27572 5.234141819
2.27655 5.231243395
2.27732 5.228540769
2.27793 5.226398834
2.2783 5.225106254

2.27848 5.224478863
2.27885 5.223186317
2.27946 5.221044542
2.28024 5.218342298
2.28107 5.215444511
2.28184 5.21274251
2.28245 5.210601091
2.28282 5.209308832
2.283 5.2086816
2.28337 5.207389386
2.28399 5.205248175
2.28476 5.202546672
2.28559 5.199649711
2.28636 5.196948513
2.28698 5.194807753
2.28735 5.1935159
2.28753 5.192888868
2.2879 5.19159707
2.28851 5.189456565
2.28928 5.18675598
2.29011 5.183860038
2.29089 5.181159821
2.2915 5.17901986
2.29187 5.177728499
2.29205 5.177101708
2.29242 5.175810412
2.29303 5.173670754
2.29381 5.170971265
2.29464 5.168076533
2.29541 5.165377475
2.29602 5.163238454
2.29639 5.16194767
2.29657 5.161321161
2.29694 5.160030453

2.29756 5.157891783
2.29833 5.155193568
2.29916 5.152300236
2.29993 5.149602515
2.30055 5.147464576
2.30092 5.146174452
2.30109 5.145548266
2.30146 5.144258226
2.30208 5.142120673
2.30285 5.13942388
2.30368 5.136532081
2.30445 5.133835792
2.30507 5.131698985
2.30544 5.130409543
2.30562 5.129783688
2.30599 5.128494328
2.3066 5.1263579
2.30737 5.123662521
2.3082 5.120772233
2.30898 5.118077349
2.30959 5.115941652
2.30996 5.114652879
2.31014 5.114027347
2.31051 5.112738654
2.31112 5.110603327
2.3119 5.107909335
2.31273 5.105020529
2.3135 5.102327021
2.31411 5.100192411
2.31448 5.098904292
2.31466 5.098279078
2.31503 5.096991038
2.31565 5.094856791
2.31642 5.092164156

2.31725 5.089276801
2.31802 5.086584641
2.31864 5.084451096
2.31901 5.083163618
2.31919 5.082538715
2.31956 5.081251314
2.32017 5.079118124
2.32094 5.076426819
2.32177 5.073540884
2.32255 5.070850043
2.32316 5.068717541
2.32353 5.06743069
2.32371 5.066806091
2.32408 5.065519316
2.32469 5.063387161
2.32546 5.060697157
2.32629 5.057812612
2.32707 5.055123062
2.32768 5.052991579
2.32805 5.051705343
2.32823 5.051081041
2.3286 5.049794878
2.32921 5.047663736
2.32999 5.044975004
2.33082 5.042091819
2.33159 5.039403532
2.3322 5.037273046
2.33257 5.03598741
2.33275 5.035363399
2.33312 5.034077835
2.33374 5.031947682
2.33451 5.029260195
2.33534 5.026378338
2.33611 5.023691285

2.33673 5.021561774
2.3371 5.020276725
2.33728 5.019652998
2.33765 5.018368019
2.33826 5.016238833
2.33903 5.013552562
2.33986 5.010672004
2.34064 5.007986157
2.34125 5.005857598
2.34162 5.004573122
2.3418 5.003949673
2.34217 5.002665266
2.34278 5.000537025
2.34356 4.997851941
2.34438 4.994972651
2.34516 4.992287981
2.34577 4.990160352
2.34614 4.988876435
2.34632 4.988253258
2.34669 4.986969408
2.3473 4.984842089
2.34808 4.982158164
2.34891 4.979280112
2.34968 4.976596591
2.35029 4.974469869
2.35066 4.973186499
2.35084 4.972563586
2.35121 4.97128028
2.35183 4.969153859
2.3526 4.966471062
2.35343 4.96359421
2.3542 4.960911799
2.35482 4.95878595
2.35519 4.957503103

2.35537 4.956880444
2.35574 4.955597659
2.35635 4.953472096
2.35712 4.950790372
2.35795 4.94791466
2.35873 4.945233302
2.35934 4.943108281
2.35971 4.94182593
2.35989 4.941203511
2.36026 4.939921219
2.36087 4.937796468
2.36165 4.93511576
2.36248 4.932241126
2.36325 4.929560764
2.36386 4.927436524
2.36423 4.926154643
2.36441 4.92553245
2.36478 4.924250624
2.36539 4.922126639
2.36617 4.919446888
2.367 4.916573271
2.36777 4.913893846
2.36838 4.911770343
2.36875 4.910488903
2.36893 4.909866924
2.3693 4.908585535
2.36992 4.906462271
2.37069 4.903783421
2.37152 4.900910759
2.37229 4.898232214
2.37291 4.896109401
2.37328 4.894828374
2.37346 4.894206595
2.37383 4.892925617

2.37444 4.890803028
2.37521 4.888125021
2.37604 4.885253251
2.37682 4.882575529
2.37743 4.880453361
2.3778 4.87917272
2.37798 4.878551128
2.37835 4.877270533
2.37896 4.875148573
2.37974 4.872471351
2.38057 4.869600412
2.38134 4.866923455
2.38195 4.864801886
2.38232 4.863521604
2.3825 4.862900185
2.38287 4.861619944
2.38348 4.859498568
2.38426 4.856822074
2.38509 4.853951904
2.38586 4.851275654
2.38647 4.849154639
2.38684 4.847874688
2.38702 4.847253428
2.38739 4.845973516
2.38801 4.843852677
2.38878 4.841176853
2.38961 4.838307391
2.39038 4.83563179
2.391 4.833511282
2.39137 4.832231635
2.39155 4.831610522
2.39192 4.830330909
2.39253 4.828210564
2.3933 4.825535351

2.39413 4.822666535
2.39491 4.819991526
2.39552 4.81787148
2.39589 4.816592109
2.39607 4.815971129
2.39644 4.814691789
2.39705 4.81257189
2.39783 4.809897232
2.39866 4.807029
2.39943 4.804354525
2.40004 4.802234896
2.40041 4.800955772
2.40059 4.800334913
2.40096 4.79905582
2.40158 4.79693633
2.40235 4.794262194
2.40318 4.791394538
2.40395 4.788720623
2.40457 4.786601458
2.40494 4.785322625
2.40511 4.78470191
2.40548 4.783423119
2.4061 4.781304149
2.40687 4.778630702
2.4077 4.775763822
2.40847 4.773090669
2.40909 4.770972133
2.40946 4.769693691
2.40964 4.769073168
2.41001 4.76779478
2.41062 4.765676494
2.41139 4.763003943
2.41222 4.760138064
2.413 4.757465881

2.41361 4.755348139
2.41398 4.754070187
2.41416 4.753449905
2.41453 4.752172019
2.41514 4.750054584
2.41592 4.747383137
2.41675 4.744518482
2.41752 4.741847477
2.41813 4.739730695
2.4185 4.738453332
2.41868 4.737833339
2.41905 4.736556055
2.41967 4.734439635
2.42044 4.731769501
2.42127 4.728906294
2.42204 4.726236676
2.42266 4.724121017
2.42303 4.722844345
2.42321 4.722224689
2.42358 4.720948107
2.42419 4.718832867
2.42496 4.716164254
2.42579 4.713302718
2.42657 4.710634694
2.42718 4.708520326
2.42755 4.707244442
2.42773 4.706625172
2.4281 4.705349391
2.42871 4.703235497
2.42948 4.700568614
2.43031 4.697708972
2.43109 4.695042752
2.4317 4.692929838
2.43207 4.691654843

2.43225 4.691036007
2.43262 4.689761127
2.43323 4.687648743
2.43401 4.684983798
2.43484 4.682126274
2.43561 4.679462066
2.43622 4.677350772
2.43659 4.676076765
2.43677 4.675458412
2.43714 4.674184532
2.43776 4.672073824
2.43853 4.669411025
2.43936 4.666555842
2.44013 4.663893854
2.44075 4.661784345
2.44112 4.660511426
2.4413 4.659893604
2.44167 4.658620824
2.44228 4.656511958
2.44305 4.653851513
2.44388 4.650998895
2.44466 4.648339336
2.44527 4.646231776
2.44564 4.644960045
2.44582 4.644342803
2.44619 4.643071223
2.4468 4.640964362
2.44758 4.63830648
2.4484 4.635456651
2.44918 4.632799728
2.44979 4.630694284
2.45016 4.62942384
2.45034 4.628807225
2.45071 4.627536942

2.45132 4.62543224
2.4521 4.622777088
2.45293 4.619930171
2.4537 4.617275935
2.45431 4.615172588
2.45468 4.613903392
2.45486 4.613287378
2.45523 4.612018321
2.45585 4.609915617
2.45662 4.607262928
2.45745 4.604418581
2.45822 4.601766674
2.45884 4.599665127
2.45921 4.598396997
2.45939 4.597781495
2.45976 4.596513482
2.46037 4.594412477
2.46114 4.591761871
2.46197 4.588919687
2.46275 4.58626973
2.46336 4.584169681
2.46373 4.582902436
2.46391 4.582287358
2.46428 4.581020209
2.46489 4.5789206
2.46567 4.576271699
2.4665 4.573431271
2.46727 4.570782883
2.46788 4.568684033
2.46825 4.567417492
2.46843 4.56680275
2.4688 4.565536281
2.46941 4.563437769
2.47019 4.560790193

2.47102 4.557951114
2.47179 4.555303917
2.4724 4.553205964
2.47277 4.551939945
2.47295 4.551325451
2.47332 4.550059482
2.47394 4.547961765
2.47471 4.545315135
2.47554 4.542476998
2.47631 4.539830612
2.47693 4.537733256
2.4773 4.536467577
2.47748 4.535853243
2.47785 4.534587592
2.47846 4.53249037
2.47923 4.529844306
2.48006 4.527006704
2.48084 4.52436075
2.48145 4.52226369
2.48182 4.52099817
2.482 4.520383907
2.48237 4.519118394
2.48298 4.517021366
2.48376 4.514375489
2.48459 4.511538015
2.48536 4.508892112
2.48597 4.506795048
2.48634 4.505529505
2.48652 4.504915226
2.48689 4.503649668
2.48751 4.501552534
2.48828 4.498906464
2.48911 4.496068711
2.48988 4.493422481

2.49049 4.491325111
2.49086 4.490059364
2.49104 4.489444981
2.49141 4.488179197
2.49203 4.486081655
2.4928 4.483435013
2.49363 4.480596574
2.4944 4.477949638
2.49502 4.475851662
2.49539 4.474585529
2.49557 4.473970954
2.49594 4.472704762
2.49655 4.470606512
2.49732 4.467958918
2.49815 4.465119387
2.49893 4.462471364
2.49954 4.460372481
2.49991 4.459105781

4 1 -1 +1 2
0 1 2 3

% NLEV2 AUTO2 J2DL J2DU J2DD
% {IV2(i)}

APPENDIX B

RKR AND LEVEL INPUT FILES FOR YO TRANSITIONS

Listing B.1. RKR input file for the $X^2\Sigma^+$ state

```

39 89 8 16 +0 0 0 % IAN1 IMN1 IAN2 IMN2 CHARGE NDEGv NDEBv
'YO - Potential energy function and constants for X state [VEXT = 0]'
2 % LMAXGv
861.4165 -2.8321 %Y10 Y20 : calculated from PGOPHER fit
1 % LMAXBv
0.388910D0 -1.755D-3 %Y01 Y11
0 1 0.d0 % Kaiser NSV VEXT
-0.4d0 0.1d0 4.6d0 %(1) V1 DV V2

```

Listing B.2. RKR input file for the $B^2\Sigma^+$ state

```

39 89 8 16 +0 0 0 % IAN1 IMN1 IAN2 IMN2 CHARGE NDEGv NDEBv
'YO - Potential energy function and constants for B state [VEXT = 0]'
2 % LMAXGv
770.7 -9.87D0 %Y10 Y20 calculated from PGOPHER fit
2 % LMAXBv
0.372860 -1.71D-3 -3.89D-4 %Y01 Y11 Y21 Y31: calculated from PGOPHER fit
0 1 0.d0 % Kaiser NSV VEXT
-0.4d0 0.1d0 4.6d0 %(1) V1 DV V2

```

Listing B.3. LEVEL input file for the $B^2\Sigma^+-X^2\Sigma^+$ transition.

```

39 89 8 16 0 2 % IAN1 IMN1 IAN2 IMN2 CHARGE NUMPOT
'YO B-X from RKR potentials with transition dipole moments (interpolated)'
0.0015 0.8 15.0 1.d-4 % RH RMIN RMAX EPS
108 0 0 59220d0 % NTP LPPOT IOMEG VLIM
10 1 1 1 0.0D+0 % NUSE IR2 ILR NCN CNN
1.D0 1.D0 0.0d0 % RFACT EFACT VSHIFT & X-state turn. pnts.

1.6023000000000000 6842.57196474949
1.6091000000000000 6276.83391024122

```

1.61590000000000	5744.05269934272
1.62270000000000	5242.30844433910
1.62950000000000	4769.79309980471
1.63638259861116	4319.56122900000
1.63770282873852	4236.28000000000
1.63903953901937	4152.94212900000
1.64039324586517	4069.54761600000
1.64176449285878	3986.09646100000
1.64315385279369	3902.58866400000
1.64456192991428	3819.02422500000
1.64598936238159	3735.40314400000
1.64743682499321	3651.72542100000
1.64890503218983	3567.99105600000
1.65039474138642	3484.20004900000
1.65190675667180	3400.35240000000
1.65344193292770	3316.44810900000
1.65500118042685	3232.48717600000
1.65658546998007	3148.46960100000
1.65819583871455	3064.39538400000
1.65983339658060	2980.26452500000
1.66149933370231	2896.07702400000
1.66319492870973	2811.83288100000
1.66492155821781	2727.53209600000
1.66668070765086	2643.17466900000
1.66847398365356	2558.76060000000
1.67030312838229	2474.28988900000
1.67217003603706	2389.76253600000
1.67407677207859	2305.17854100000
1.67602559568378	2220.53790400000
1.67801898613215	2135.84062500000
1.68005967399838	2051.08670400000
1.68215067826598	1966.27614100000
1.68429535079611	1881.40893600000
1.68649743001530	1796.48508900000

1.68876110627073	1711.504600000000
1.69109110210961	1626.467469000000
1.69349277187108	1541.373696000000
1.69597222659061	1456.223281000000
1.69853649255233	1371.016224000000
1.70119371527690	1285.752525000000
1.70395342594652	1200.432184000000
1.70682689534108	1115.055201000000
1.70982761320473	1029.621576000000
1.71297195205794	944.131309000000
1.71628011038966	858.584400000000
1.71977749395024	772.980849000000
1.72349681289073	687.320656000000
1.72748140817179	601.603821000000
1.73179082245097	515.830344000000
1.73651080091984	430.000225000000
1.74177298036567	344.113464000000
1.74779901577956	258.170061000000
1.75502122251165	172.170016000000
1.76455604013944	86.113329000000
1.78816212376122	0.000000000000
1.81262933243960	86.113329000000
1.82302576966165	172.170016000000
1.83111009113658	258.170061000000
1.83799873705398	344.113464000000
1.84412402337723	430.000225000000
1.84970760571184	515.830344000000
1.85488112146070	601.603821000000
1.85973031643216	687.320656000000
1.86431473390170	772.980849000000
1.86867771544917	858.584400000000
1.87285197184592	944.131309000000
1.87686290946385	1029.621576000000
1.88073072741464	1115.055201000000

1.88447179884266	1200.43218400000
1.88809961411720	1285.75252500000
1.89162544464448	1371.01622400000
1.89505882223423	1456.22328100000
1.89840789303586	1541.37369600000
1.90167968396348	1626.46746900000
1.90488030668372	1711.50460000000
1.90801511616812	1796.48508900000
1.91108883559754	1881.40893600000
1.91410565595399	1966.27614100000
1.91706931630009	2051.08670400000
1.91998316913432	2135.84062500000
1.92285023407875	2220.53790400000
1.92567324234785	2305.17854100000
1.92845467386219	2389.76253600000
1.93119678844093	2474.28988900000
1.93390165218835	2558.76060000000
1.93657115994924	2643.17466900000
1.93920705452604	2727.53209600000
1.94181094321074	2811.83288100000
1.94438431207620	2896.07702400000
1.94692853838723	2980.26452500000
1.94944490142498	3064.39538400000
1.95193459196593	3148.46960100000
1.95439872061404	3232.48717600000
1.95683832515146	3316.44810900000
1.95925437704523	3400.35240000000
1.96164778722560	3484.20004900000
1.96401941123310	3567.99105600000
1.96637005381664	3651.72542100000
1.96870047305260	3735.40314400000
1.97101138404438	3819.02422500000
1.97330346225357	3902.58866400000
1.97557734650652	3986.09646100000

1.97783364171423	4069.54761600000
1.98007292133815	4152.94212900000
1.98229572963039	4236.28000000000
1.98450258367300	4319.56122900000

108 0 0 75000	% NTP2 LPPOT2 IOMEG2 VLIM2
10 1 1 1 0.D0	% NUSE2 IR22 ILR2 NCN2 CNN2
1.D0 1.D0 20741.6778D0	% RFACT EFACT VSHIFT2 & B state

1.64320000000000	6151.33916773031
1.64900000000000	5536.66015877372
1.65480000000000	4988.45155220234
1.66060000000000	4499.52534528806
1.66640000000000	4063.47083439186
1.67221136611504	3673.85130000000
1.67328310830687	3606.75000000000
1.67438126172953	3539.45130000000
1.67550631806320	3471.95520000000
1.67665879785300	3404.26170000000
1.67783925262434	3336.37080000000
1.67904826720839	3268.28250000000
1.68028646230332	3199.99680000000
1.68155449730132	3131.51370000000
1.68285307341543	3062.83320000000
1.68418293714596	2993.95530000000
1.68554488413237	2924.88000000000
1.68693976344407	2855.60730000000
1.68836848237272	2786.13720000000
1.68983201179915	2716.46970000000
1.69133139222131	2646.60480000000
1.69286774054504	2576.54250000000
1.69444225775898	2506.28280000000
1.69605623763783	2435.82570000000
1.69771107664743	2365.17120000000

1.69940828526029	2294.319300000000
1.70114950093458	2223.270000000000
1.70293650306509	2152.023300000000
1.70477123028443	2080.579200000000
1.70665580058175	2008.937700000000
1.70859253481985	1937.098800000000
1.71058398437886	1865.062500000000
1.71263296384633	1792.828800000000
1.71474258992571	1720.397700000000
1.71691632807167	1647.769200000000
1.71915804881210	1574.943300000000
1.72147209633307	1501.920000000000
1.72386337275323	1428.699300000000
1.72633744270627	1355.281200000000
1.72890066454745	1281.665700000000
1.73156035696050	1207.852800000000
1.73432501337843	1133.842500000000
1.73720458212689	1059.634800000000
1.74021083870675	985.229700000000
1.74335789017484	910.627200000000
1.74666287382517	835.827300000000
1.75014695025420	760.830000000000
1.75383675817548	685.635300000000
1.75776662392012	610.243200000000
1.76198206724636	534.653700000000
1.76654567466435	458.866800000000
1.77154764681294	382.882500000000
1.77712657071433	306.700800000000
1.78351599048324	230.321700000000
1.79117177836958	153.745200000000
1.80127220488753	76.971300000000
1.82624293600549	0.000000000000
1.85213646855252	76.971300000000
1.86318177731134	153.745200000000

1.87180456916787	230.321700000000
1.87918315673948	306.700800000000
1.88577345557169	382.882500000000
1.89180905427424	458.866800000000
1.89742858557087	534.653700000000
1.90272229701593	610.243200000000
1.90775282325654	685.635300000000
1.91256573341718	760.830000000000
1.91719540443245	835.827300000000
1.92166852686487	910.627200000000
1.92600631441369	985.229700000000
1.93022595873824	1059.634800000000
1.93434162253198	1133.842500000000
1.93836513821282	1207.852800000000
1.94230651231318	1281.665700000000
1.94617429777204	1355.281200000000
1.94997587408811	1428.699300000000
1.95371766175059	1501.920000000000
1.95740528885634	1574.943300000000
1.96104372232687	1647.769200000000
1.96463737250147	1720.397700000000
1.96819017742268	1792.828800000000
1.97170567143235	1865.062500000000
1.97518704150523	1937.098800000000
1.97863717389592	2008.937700000000
1.98205869305948	2080.579200000000
1.98545399435367	2152.023300000000
1.98882527169521	2223.270000000000
1.99217454108977	2294.319300000000
1.99550366076374	2365.171200000000
1.99881434847881	2435.825700000000
2.00210819649662	2506.282800000000
2.00538668457177	2576.542500000000
2.00865119128160	2646.604800000000

2.01190300394579	2716.469700000000
2.01514332734465	2786.137200000000
2.01837329140910	2855.607300000000
2.02159395802709	2924.880000000000
2.02480632708731	2993.955300000000
2.02801134186240	3062.833200000000
2.03120989381769	3131.513700000000
2.03440282691897	3199.996800000000
2.03759094150152	3268.282500000000
2.04077499775417	3336.370800000000
2.04395571886407	3404.261700000000
2.04713379386200	3471.955200000000
2.05030988020237	3539.451300000000
2.05348460610773	3606.750000000000
2.05665857270361	3673.851300000000

-4	1	0	4	0	1	-1	0	% NLEV1	AUTO1	LCDC	LXPCT	NJM	JDJR	IWR	LPRWF
0	0							% IV(1)	IJ(1)						
1	10		1.D0					% MORDR	IRFN	DREF					
79	0.2							% NRFN	RFLIM						
10	1	1	0.D0					% NUSEF	ILRF	NCNF	CNNF				
1.d0	1.d0							% RFACTF	MFACTF						

1.58	-4.834644789
1.59	-4.796038185
1.60	-4.756974096
1.61	-4.718952056
1.62	-4.681717905
1.63	-4.644661665
1.64	-4.636452361
1.65	-4.620135415
1.66	-4.58353666
1.67	-4.545997519
1.68	-4.507441747

1.69	-4.467818511
1.70	-4.427026148
1.71	-4.384962995
1.72	-4.34157822
1.73	-4.296668497
1.74	-4.250081331
1.75	-4.201613395
1.76	-4.151035948
1.77	-4.097993168
1.78	-4.042129234
1.79	-3.982986662
1.80	-3.919879224
1.81	-3.852095279
1.82	-3.778669025
1.83	-3.698355089
1.84	-3.609653938
1.85	-3.510608556
1.86	-3.398753609
1.87	-3.271115449
1.88	-3.124085031
1.89	-2.953367086
1.90	-2.754030946
1.91	-2.519366842
1.92	-2.237226018
1.93	-1.883666789
1.94	-1.424774308
1.95	-0.899081473
1.96	-0.494281444
1.97	-0.269072018
1.98	-0.140015656
1.99	-0.051339921
2.00	0.093479322
2.01	0.137601155
2.02	0.179511813

2.03	0.219338376
2.04	0.257207922
2.05	0.29324753
2.06	0.327609695
2.07	0.360548575
2.08	0.39206417
2.09	0.422003985
2.10	0.450418852
2.11	0.477308772
2.12	0.50274999
2.13	0.526717092
2.14	0.549286324
2.15	0.570457688
2.16	0.590231182
2.17	0.608632223
2.18	0.625660811
2.19	0.641342361
2.20	0.655702289
2.21	0.668689765
2.22	0.680355618
2.23	0.69069985
2.24	0.699697044
2.25	0.707398032
2.26	0.713751982
2.27	0.718809727
2.28	0.722520434
2.29	0.741150218
2.30	0.742700582
2.31	0.743310561
2.32	0.743463056
2.33	0.743158066
2.34	0.74186186
2.35	0.738989874
2.36	0.734287951

```
5  1  -1 +1 2
0  1  2  3  4
```

```
% NLEV2 AUTO2 J2DL J2DU J2DD
% {IV2(i)}
```

VITA

Randika Dodangodage
Department of Physics
Old Dominion University
Norfolk, VA 23529

EDUCATION

MS Physics, Old Dominion University, 2020.

BS Physics, University of Sri Jayewardenepura, Sri Lanka, 2015.